Lehrstuhl für Solartechnik

RWTH AACHEN UNIVERSITY

The present work was submitted to the Institute of Solar Research
German Aerospace Center (DLR)

Commissioning and optimization of a test bench for life cycle analysis of rotation and expansion performing assemblies (REPAs) in parabolic trough collector power plants

MASTER-THESIS

presented by

Falko Schneider

Energy Engineering (M.Sc.)

Supervision and Assessment:

1st Examiner:	Univ.-Prof. Dr.-Ing. Bernhard Hoffschmidt
2nd Examiner:	Dipl.-Ing. Christoph Hilgert
Tutor:	Dipl.-Ing. Wolfgang Reinalter

Almería, 09.05.2019

Declaration of Academic Honesty

Eidesstattliche Erklärung

I hereby declare to have written the present master's thesis on my own, having used no other resources and tools than the listed. All contents cited from published or nonpublished documents are indicated as such.

Hiermit erkläre ich, dass ich die vorliegende Masterarbeit selbständig verfasst und keine anderen als die angegebenen Hilfsmittel verwendet habe. Alle Inhalte, die wörtlich oder sinngemäß aus veröffentlichten oder nicht veröffentlichten Schriften entnommen sind, sind als solche kenntlich gemacht.

_____	_____
Place, Date	Signature

Abstract

Rotation and Expansion Performing Assemblies (REPAs) are used in Parabolic Trough Collector (PTC) power plants to connect the moving absorber tubes to the fixed piping of the rest of the power plant. They are one of the most stressed and critical components of a PTC power plant. During their service life they have to withstand approx. 10.000 daily load cycles. A failure can lead to HTF leakages which are often flammable and environmentally hazardous. That's why a leak free and reliable operation is crucial for safe power plant operation.

The main focus of this thesis is the optimization of the kinematics unit (KU) of a life cycle assessment test rig in regards to reproducibility and overall test time. The test facility can subject the REPA to typical pressures, temperatures and mass flows of Heat Transfer Fluids while simulating the daily motions of a PTC. The rotation can be mimicked with a continuous rotation or a step-by-step motion for a more realistic sun-tracking simulation. At the same time the KU simulates thermal expansions of the absorber tube with a lateral translation. A full REPA life cycle test with reproducible loads can be achieved within 17 days for a continuous or 63 days for a step-by-step motion.

In order to ensure operational safety, issues regarding the mechanical stability of the KU have been investigated and solution approaches are proposed and partially tested. At the conclusion of this work the step-by-step motion causes critical oscillations which need to be dealt with in future work. While these oscillations prohibit a 10.000 cycle test with step-by-step motion at this point, a life cycle test with continuous rotation is feasible.

Table of contents

Symbol directory

Symbol	Description	Unit
η	viscosity	mPa·s
$\Delta\varphi_{step}$	size of a motion increment	°
$\Delta\varphi_{step,set}$	set step size of a cycle	°
φ	rotational position of the traverse	°
φ_{stow}	rotational position if the PTC is not in use	°
φ_{start}	rotational position at which the PTC starts tracking the sun	°
φ_{stop}	rotational position at which the PTC stops tracking the sun	°
ρ	density	kg/m^3
c_p	heat capacity	J/(kg·K)
F_{cyl}	hydraulic cylinder force exerted onto the traverse interface	N
$F_{cyl,t}$	tangential component of F_{cyl}	N
$F_{cyl,r}$	radial component of F_{cyl}	N
l_{eff}	effective lever of the cylinder force onto the rotational axis	m
k	Transmission factor between servo and the cylinders	(rad·m)/s
M_{cyl}	drive torque generated by the hydraulic cylinder	Nm
M_{drive}	moment at rotational axis which drives the traverse	
$M_{friction,stat}$	moment generated by static friction in the rotational bearings	Nm
$M_{friction,dyn}$	moment generated by dynamic friction in the bearings	Nm
M_g	gravitational moment of the traverse	Nm
$M_{g,max}$	maximum gravitational moment at 0°	Nm
M_{servo}	servo motor torque	Nm
Δn_{max}	maximum speed deviation from ramp	rev/min
$n_{servo,act}$	actual servo motor revolutions	rev/min
$n_{servo,set}$	set servo motor revolutions for the P-controller	rev/min
P_{servo}	power of servo motor	%
p_{max}	maximum pressure	bar
r_{acc}	servo motor acceleration ramp	(rev/min)/s
r_{dec}	servo motor deceleration ramp	(rev/min)/s
s_{cyl}	distance of piston extension/retraction	m
$s_{cyl,t}$	tangential component of s_{cyl}	m

$s_{cyl,r}$	radial component of s_{cyl}	m
T_f	freezing point	°C
T_{max}	maximum operating temperature	°C
t_{go}	duration of the servo motor running for one step	ms
$t_{standstill}$	duration the traverse does not move between steps	ms
t_{stop}	duration between servo motor starts	ms
v_{act}	actual rotational velocity of the traverse	°/s
v_{set}	set rotational velocity of the PI-controller	°/s

List of abbreviations

BJA	Ball Joint Assembly
BJ	Ball Joint
CIEMAT	Centro de Investigaciones Energéticas, Medioambientales y Tecnológicas (Centre for Energy, Environment and Technology Research)
CSP	Concentrating Solar Power
CW	Counterweight
DLR	Deutsches Zentrum für Luft- und Raumfahrt e.V. (German Aerospace Center)
DNI	Direct Normal Irradiation
GUI	Graphical User Interface
HCE	Heat Collector Element
HTF	Heat Transfer Fluid
KU	Kinematic Unit
LFC	Linear Fresnel Collector
PLC	Programmable Logic Controller
PSA	Plataforma Solar de Almería
PTC	Parabolic Trough Collector
PV	Photovoltaics
REPA	Rotation and Expansion Performing Assembly
RFHA	Rotary Flex Hose Assembly
SCA	Solar Collector Assembly
SCADA	Supervisory Control and Data Acquisition
SCM	Solar Collector Module
SJ	Swivel Joint
ST	Solar Tower

1 Introduction and Motivation

In order to successfully face climate change, people from all across the globe need to work together. An important step towards this goal was the Paris climate conference and the resulting agreement in 2015. In this agreement 195 signatory countries pledge to keep the rise of the global average temperature compared to pre-industrial times well below the 2 °C mark [1]. The actual self-imposed limit is a rise of 1.5 °C. Since then, countries have put policies into action to curb their carbon emissions. Most of these are focused on the energy sector by replacing outdated technology with more efficient ones and by investing in the development and proliferation of renewable energy technologies. One of those renewable technologies is Concentrating Solar Power (CSP).

This technology uses the direct solar radiation to heat up Heat Transfer Fluids (HTF). This heat can be used in industrial applications (e.g. the paper industry) or to generate electricity, e.g. with a conventional steam power plant cycle. Commercially successful technologies are Solar Tower (ST) and Parabolic Trough Collector (PTC). The latter one uses troughs of parabolic mirrors to focus the sunlight onto absorber tubes in their focal line over lengths of up to 150 m [2]. In a PTC power plant the HTF cycles through the absorber tubes of several of these troughs to reach the desired output temperature for the subsequent energy conversion process. Since economical concerns play a major role in the market penetration of new technologies, they must become comparable or better yet cheaper than the fossil fuel alternatives. There are three main approaches to achieve this: increase efficiency, decrease costs or increase reliability. These factors are interconnected, e.g. a model proven to be reliable can be mass produced which reduces the associated costs per unit.

This thesis focuses on the commissioning of a test rig to prove the reliability of a key PTC power plant component: Rotation and Expansion Performing Assemblies (REPAs) which connect the moving absorber tube with the rest of the power plant HTF cycle. The troughs, along with the absorber tubes, rotate to track the sun. This is a challenge since the collector’s focal line and axis of rotation are commonly not aligned. Additionally, the length of the absorber tube generally varies throughout the day due to thermal expansion/contraction caused by changing temperatures ranging from ambient temperature to 400 °C. A REPA has to withstand these temperatures,

the heat-induced expansions of the pipe and tracking-caused rotation for a service life of 25-30 years. This makes it one of the most stressed and critical components of a PTC power plant. A failure can lead to HTF leakages which are often flammable and environmentally hazardous. That's why a leak free and reliable operation is crucial for safe power plant operation.

A test rig for life cycle assessment for REPAs was devised at the Plataforma Solar de Almería (PSA). A kinematic unit subjects the REPA to a sequence of motions to simulate its daily load cycle while HTF is being circulated through it. The KU uses two hydraulic cylinders to rotate a pipe analogously to the motion of an absorber tube in a commercial PTC module. Two additional hydraulic cylinders enable a lateral movement of the pipe. The primary goal of this test rig is to determine the durability of REPA models prevalent in the industry. During tests the REPA is monitored with a variety of sensors, e.g. force, pressure and temperature sensors. These results yield reliable information about the service life and possible failure mechanisms of a REPA. The conclusions can then be used to assess the reliability of this CSP technology before defects develop or a complete failure occurs.

The main objective of this thesis is to develop a REPA test cycle which minimizes the time necessary to run a full life cycle assessment while maintaining safe operating conditions and reproducible REPA loads. A new PLC control algorithm for the kinematics unit is devised, implemented and tested to minimize the overall life cycle test runtime and ensure its reproducibility. It simulates three types of movements:

- continuous rotation to simulate the PTC module during initial and stow positioning phase
- step-by-step rotation to simulate the PTC during the sun-tracking phase
- translation to simulate the thermal expansion

Another aspect of this work is the improvement of the long-term mechanical stability of the test rig. A counterweight is designed and installed to decrease the loads on the hydraulics system which powers the rotation and the KU drive pylon. A more balanced traverse is prone to critical oscillations though. The kinematic system is analyzed to determine whether possible weak points in the test rig contribute to the severity of the oscillations and if the motion control algorithm can mitigate them.

2 State of the Art

In this chapter a general overview over solar technologies will be given. Then the focus will shift to CSP, especially PTC, and finally onto the core topic of this work: Rotation and Expansion Performing Assemblies (REPAs) and existing test benches for REPA life cycle analysis.

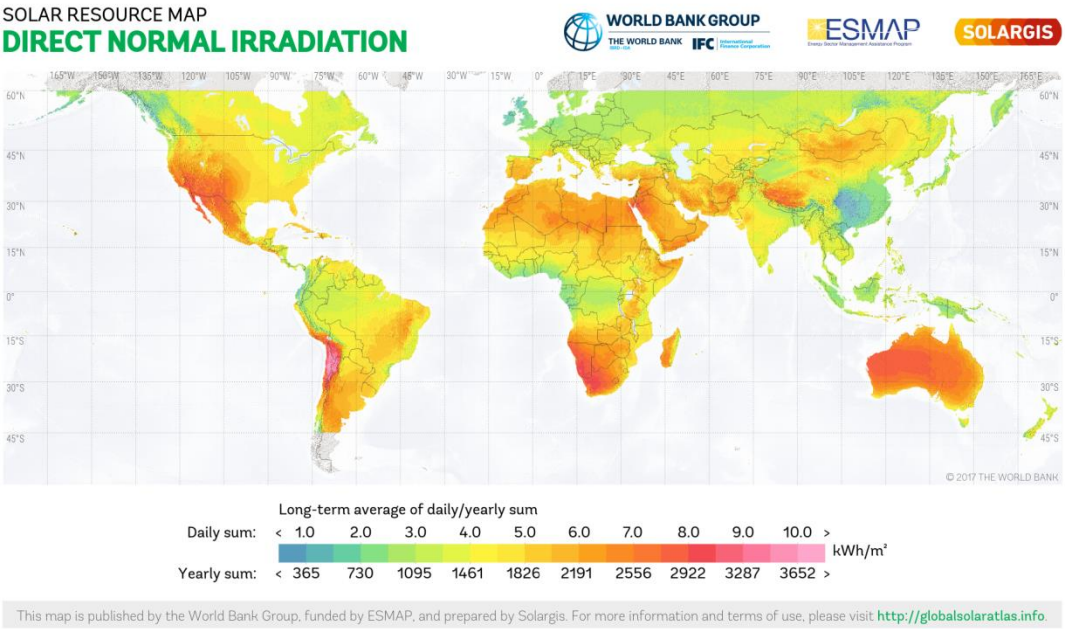

Figure 1 Global map of direct normal irradiation [3]

The sun is the primary energy source for life on earth and is available to be harnessed in abundance. In six hours the deserts of the world would receive enough energy to satisfy the human energy demand for an entire year [4]. The irradiation hits the planet with 1367 W/m², but the direct normal irradiation (DNI) is reduced by earth's atmosphere due to reflection, absorption and scattering. Some of these losses are still available in the form of diffuse solar radiation. This is a general term which describes all non-direct sunlight, e.g. the sunlight scattered by molecules and aerosols in the atmosphere. Since the atmospheric composition and environmental parameters of the terrain change across the globe, so does the DNI and diffuse irradiation. An exemplary overview of the global DNI distribution is given in Figure 1. It shows that location is one of the major deciding factors in the planning stage of a new power plant. It also displays the vast potential in solar power generation.

There are two major ways to transform this abundant solar irradiation into electrical energy: Photovoltaics (PV) and concentrating solar power. The former uses the

photovoltaic effect to directly generate electricity from the sunlight: The incoming irradiation carries enough energy to excite some electrons in the absorbent medium so they are able to leave their atoms and thereby mobile charge carriers are released. By employing P- and N-type semiconductors as cell layers, a p-n junction is created in between them. This is also called the depletion zone because it separates the charge carriers (cf. Figure 2). This difference of the electrical potential can then be tapped by an external circuit to provide electrical current.

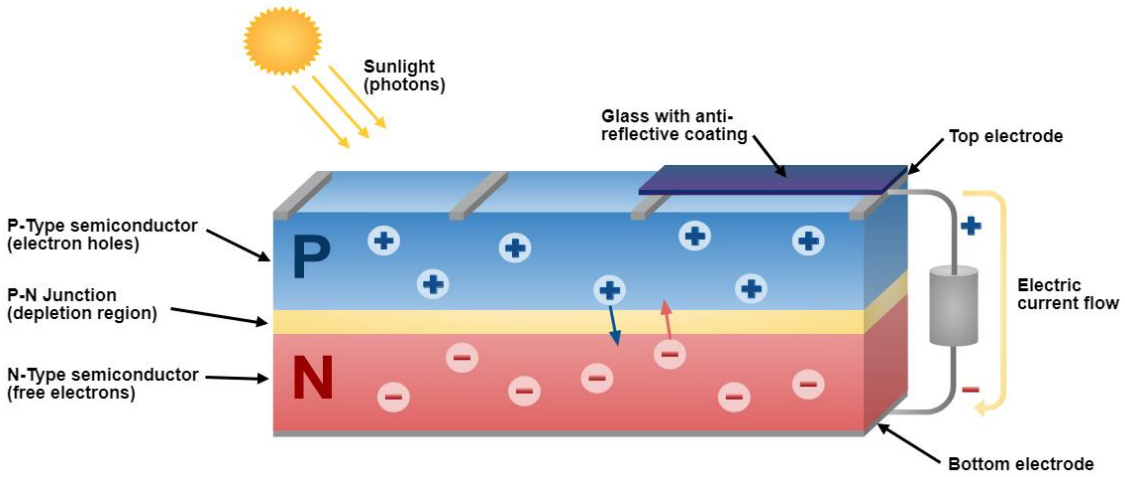

Figure 2 Basic structure and operating principle of a PV Cell [5]

These PV systems have many advantages, e.g. they are modular, scalable and easily maintained. The world record of peak efficiency in converting solar energy into electrical energy using a multilayer PV cell under laboratory conditions is 46% [6]. This technology can also harness diffuse radiation for power generating purposes, unlike CSP. But PV faces similar challenges as other renewable energy technologies do, e.g. volatile and inconsistent electricity production due to changing weather and the limited, expensive storage capacity for electrical energy which could compensate this.

Although a PV cell can be operated with concentrated sunlight as well, it is not widely done because cell efficiency rapidly declines with increasing cell temperature [7]. This thesis focuses on solar thermal applications. So, CSP applications regarding PV will not be discussed in this thesis.

2.1 Concentrating Solar Power

Instead of converting solar irradiation directly into electrical energy like PV, CSP first converts it into thermal energy which can then be used in a conventional power plant process, e.g. in a steam engine cycle, to generate electricity. The unfocused irradiation of the sun is not sufficient to generate enough heat to power a conventional power plant process. In order to create an energetically and economically efficient alternative to other energy sources the solar power needs to be concentrated. Due to the combined process, the solar-to-electric efficiency of CSP is generally lower than that of a PV cell. With new, experimental concentrator designs, the solar-to-thermal efficiency can reach up to 97% [8]. This combination also offers an advantage: for a couple of days, the thermal energy of the intermediate step can be more cost efficiently stored than electrical energy, e.g. in molten salt tanks. A CSP power plant with such a design has a better dispatchability since it can produce electricity beyond the time between sunrise and sundown [9]. The storage can also be used to compensate for detrimental, short-term weather changes, e.g. clouds.

Solar towers can generate temperatures beyond 700 °C on a large scale [10]. So, it can also be used for other applications beside electricity generation: for processes that require heat which would otherwise had to be generated by fossil fuels or electricity. Industrial heat demand makes up two-thirds of industrial energy demand and almost a fifth of global energy consumption [11]. Some possible applications being researched are water desalination, concentrating solar fuels (e.g. hydrogen) or just an overall cogeneration of heat and electricity [9].

2.1.1 CSP technologies

Because only the direct, not the diffuse, sunlight can be concentrated, a location for a CSP power plant should have a high ratio of DNI to diffuse irradiation throughout the year. That way the thermal output of the concentration can be maximized. The concentrator systems can be separated into two groups: point-focusing and line-focusing systems (cf. Figure 3). The former are able to achieve concentration beyond one thousand fold, but also require two axis solar tracking. For line-focusing systems one-axis tracking is sufficient to maintain the necessary solar intensity and focal point in order to efficiently provide the heat for the subsequent power plant process.

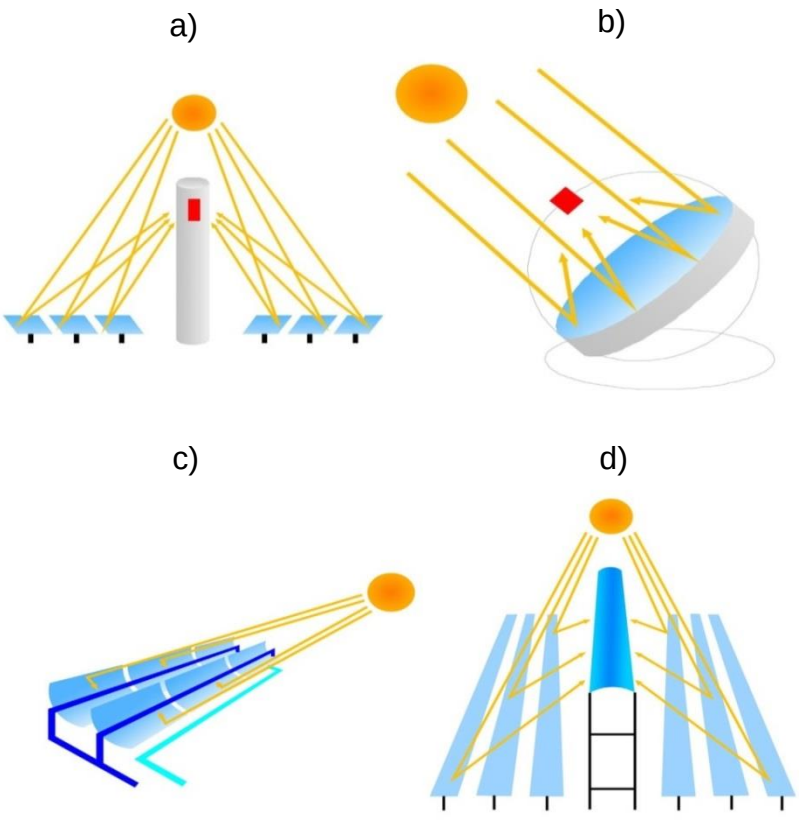

Figure 3 Operating principles of solar tower (a), dish (b), parabolic trough (c) and linear Fresnel (d) concentrators [12]

2.1.1.1 Solar Tower

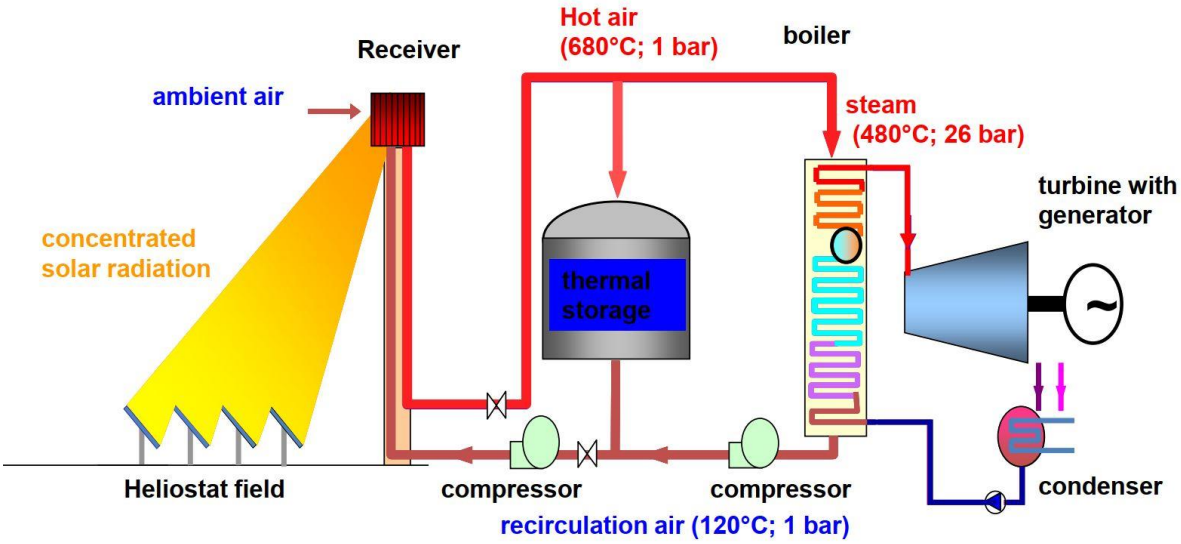

Figure 4 Operating principle of a solar tower power plant [10]

A Solar Tower (ST) design is shown in Figure 4. It uses a field of slightly curved mirrors, called heliostats, to concentrate the sunlight onto a single receiver located at the top of a tower. This field partly or fully encircles the receiver. The degree depends on the receiver design and the latitude of the power plant location. Since the sunlight needs to be kept on a single spot, precise tracking of every single heliostat is crucial. Because of this large scale a concentration of up to one thousand fold can be achieved which results in peak temperatures of up to 1200 °C at the receiver [10]. This heat can then be absorbed by the working fluid, e.g. water/steam, molten salt or air. The choice of fluid usually depends on the absorber temperature and the subsequent plant cycle. Usually a Rankine cycle with water, a Brayton cycle with air or a combination of both is deployed.

Another feature shown in the figure above is a thermal storage. This can be used to even out the volatility of solar radiation during the day. During peak supply, e.g. noon, the surplus thermal energy, which is not needed for electricity generation, can be stored in storage tanks. This enables the power plant to continue to generate electricity for a few hours after sunset or before sunrise, when the demand peaks but no heat can be drawn from the receiver. The design and material of the storage tanks depends on the working temperatures of the plant, the chosen HTF and the intended storage operation. Two examples for this are packed rock bed or molten salt storage tanks.

2.1.1.2 Solar Dish

This point-focusing CSP design uses a large circular, paraboloid shaped mirror to concentrate the sunlight onto a single receiver. In order to successfully keep the focal point on the absorber throughout the day, the assembly has to precisely track the suns movement on two axes. The focused sunbeams can then be used to generate electricity, e.g. with a Stirling engine. Alternative concepts to the Stirling motor include high flux PV cells or an absorber to heat up a HTF which in turn transports the energy to a conventional power plant cycle. The most developed design uses a Stirling engine.

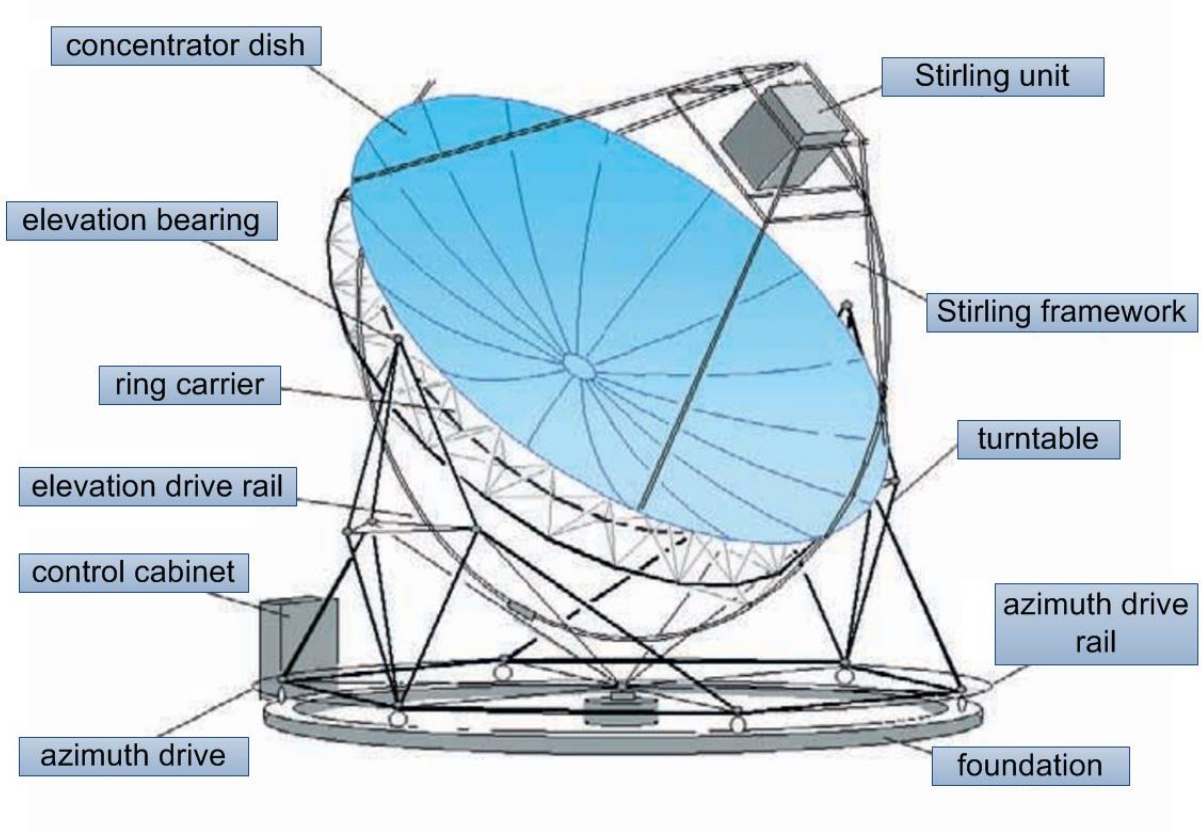

Figure 5 Assembly of a dish Stirling collector [13]

The output of one dish typically ranges from 5 to 50 kW [13]. For an electricity output on a power plant level hundreds of these would have to be installed. It has been demonstrated that this kind of assembly can be reliably operated as grid-connected and standalone power generator [14]. Concerning the grid-connected operation solar dishes are inferior to other CSP technologies, e.g. PTC, in regards to costs and scalability. By directly connecting a generator to the Stirling engine, this technology can function as a standalone solar power generator. It is ideal to be set up in remote

locations to provide a decentralized electricity supply there. Although for that scenario PV technology is the cheaper, simpler, more robust and therefore state-of-the-art choice. Due to these factors this design is not a focus of CSP research anymore.

2.1.1.3 Parabolic Trough Collector

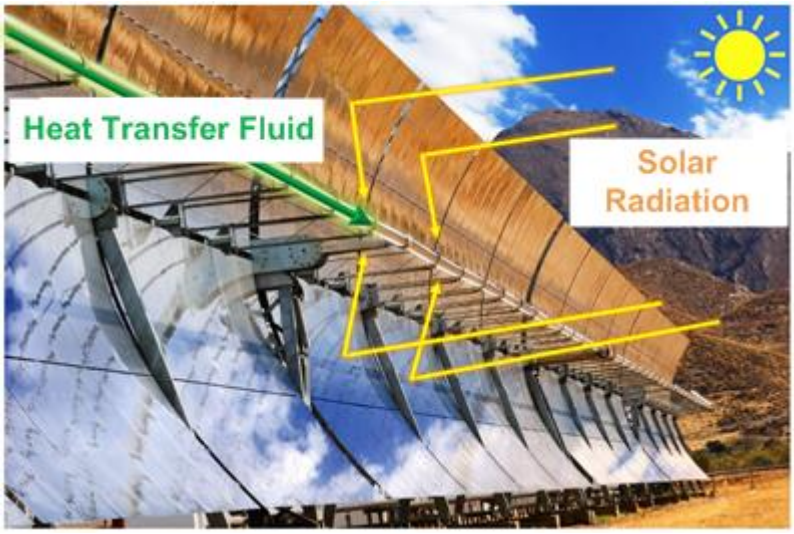

Figure 6 Operating principle of a parabolic trough collector [10]

The PTC design uses a trough of mirrors with a parabolic cross section. The sunlight is concentrated onto a focal line in which a heat collector element (HCE) containing the HTF is located. The size of these mirrors varies between models. The aperture area of a SkyFuel SkyTrough solar collector module (SCM) for instance measures around 6 m in width and 14 m in length [15]. Such collectors are mounted onto a torque tube or a space frame. The height combined with their large surface area results in non-negligible wind loads. During both high and no wind load conditions these mirrors have to maintain their form to properly maintain optical performance. Wind loads can lead to a shutdown of the plant because the troughs need to be driven into stow position[1] to minimize the wind-exposed surface. The maximum wind speed before the collector needs to be stowed depends on the SCM design. The SkyTrough for example has an aperture of 6 m and is able to continuously withstand wind speeds of about 40 km/h with wind gusts (3 seconds duration) of up to 65 km/h

[1] concave side facing downwards

before needing to be driven into stow position. The maximum speed regarding survivability of the frame in stow position is 135 km/h [15].

For practical and economic reasons many SCMs are serially connected to form a solar collector assembly (SCA) which heats up the HTF within one absorber tube. These trough assemblies can be up to 150 m long to provide the necessary heat for the HTF in order to reach the temperature for the subsequent energy conversion process. The volumetric HTF output of one SCA is usually not sufficient to operate an industrial-scale power plant. That's why many of these are being operated in parallel (cf. Figure 7), e.g. approximately 140 SCAs are necessary for a 50 MW PTC power plant. The rest of the layout is similar to the previously shown solar tower with a molten storage design and a Rankine cycle (cf. Chpt. 2.1.1.1).

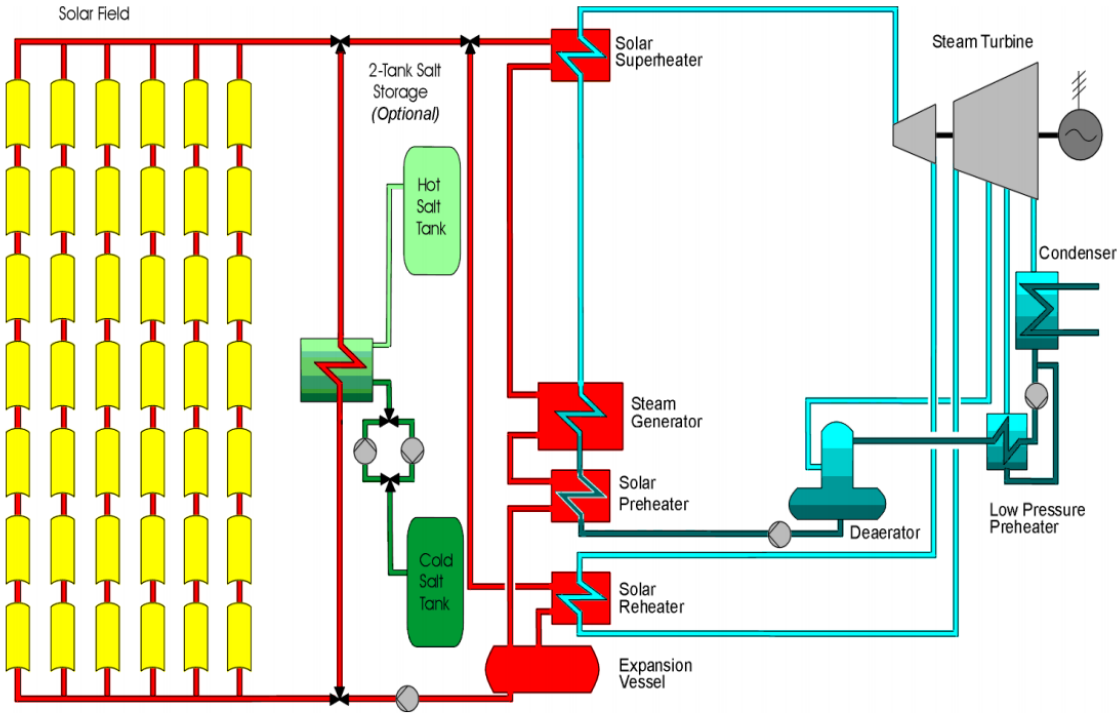

Figure 7 Basic layout of the Andasol PTC power plant in Spain [10]

PTCs reach high overall solar-to-thermal efficiencies of around 70% [2]. Detrimental factors are for example: so-called cosine losses because the trough tracks the sun only along one axis, declining optical efficiency of the mirrors due to dirt, thermal losses to the environment due to the high operating temperatures and additional optical losses due to inaccurate tracking [10].

The core of the HCE is a steel tube with a selective coating[2] which absorbs the concentrated sunlight from the mirrors below and also the global irradiation from the top (cf. Figure 8). The coating is designed to have a high absorbance for radiation in the solar spectrum (350 - 7800 nm) to increase the energy absorption and a low emissivity in the infrared spectrum (> 800 nm) to reduce thermal losses. These can be for example sputtered coatings of several ceramic and metal layers or galvanic black-nickel coatings [2]. To protect the sensitive absorber from degradation and mechanical damages it is encased in an evacuated glass tube which reduces the heat losses due to convection. Common HTFs degrade during operation and release hydrogen, which diffuses through the metal tube into the annular, evacuated gap. To diminish convective heat losses inside the gap and to keep the components from chemical degradation so-called getters are placed in the annular space. These are reactive materials, which can absorb the hydrogen.

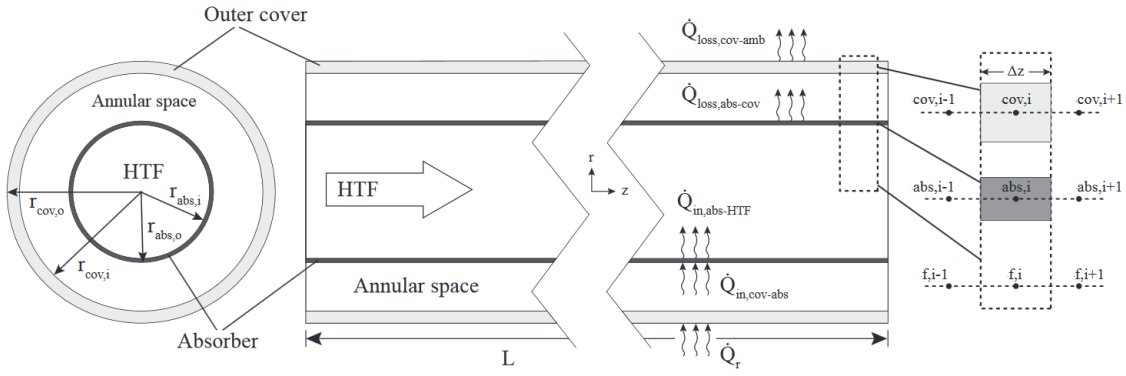

Figure 8 Schematic diagram of a PTC HCE cross section and its heat flows [16]

A PTC requires one-axis sun-tracking and the absorber tube is not stationary. The focal line of a PTC is always in the same relative position to the parabolic mirror[3], which moves to track the sun. The moving receiver tube is only stationary relative to the mirrors. That poses a challenge since the absorber tube needs to be connected to the rigid piping of the rest of the power plant for the HTF to get to the heat exchanger of the energy conversion process. REPAs have been developed for this purpose. They are designed to withstand the temperatures and pressures of the HTF

[2] high absorbance in the solar and low emissivity in the infrared wavelength spectrum

[3] for perpendicular irradiation into the trough

as well as the stresses which stem from the rotation and thermal expansion of the receiver tube. The PTC plant is not operating during the night, so every day the tube cycles between the night temperature of approx. 100°C and the operating temperature, which can be up to 500 °C. Overnight the temperature is commonly kept from dropping to ambient temperatures by circulating the HTF through the SCAs with a flow rate of approx. 1% compared to operating conditions. Especially in desert regions where PTCs are common, the HTF could freeze otherwise. The overall thermal expansion is below 1% of the HCE length. But because of the successive placement of many PTC SCMs, the expansion of one 150 m long absorber tube totals up to 1.3 m which has to be offset by only 2 REPAs (one at each end).

2.1.1.4 Linear Fresnel Collector

The LFC focuses the sunlight on a line. In this focal line HTF flows within an absorber tube and carries the heat to the subsequent energy conversion process. The mirrors which concentrate the irradiation are parallel sets of small, concave mirrors along the absorber tube (cf. Figure 9, left). These reflectors uniaxially track the sun throughout the day. Compared to the parabolic concentrator shape, this segmented mirror design can yield a much higher aperture area and thus higher concentrations, but the downside is a reduced optical efficiency[4], e.g. due to overshadowing amongst the segments. While the mirrors track the sun, the absorber tube remains stationary and only the thermal expansion needs to be compensated. The state-of-the-art solution is a corrugated, steel hose. A secondary concentrator is placed around the top of the absorber tube (cf. Figure 9, right). This mitigates losses due to tracking inaccuracies and mirror slope deviations.

[4] ratio of incident radiation onto the aperture to concentrated radiation onto the absorber tube

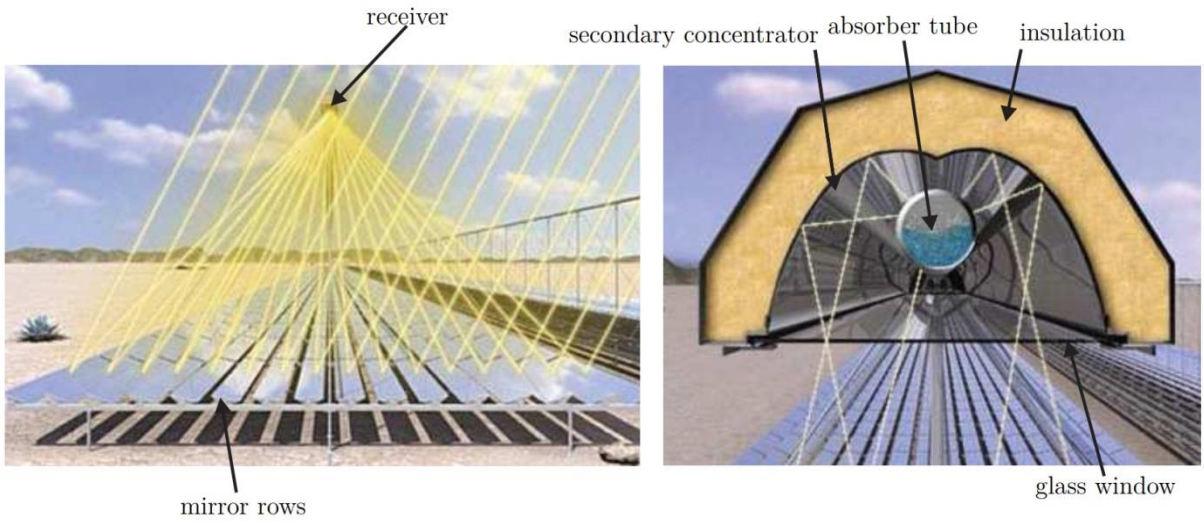

Figure 9 Operating principle of a linear Fresnel collector [17]

Besides the stationary tube, other advantages in regards to PTC are the lower possible wind loads, higher ground usage and more easily cleaned mirrors. On the other hand this design has a lower optical performance and requires more precise sun-tracking since the movement of the reflected beam is twice the angular movement of the mirror [2]. The negative side effects can be mitigated by the larger aperture area.

2.1.2 Heat Transfer Fluid

Generally, the efficiency of a thermodynamic cycle increases with increasing input temperature. Currently the maximum temperature of the transfer fluid is one of the limits regarding CSP efficiency. The state-of-the-art HTFs used in commercial plants are synthetic thermal oils, e.g. HELISOL 5A. There are a few power plants that use water/steam and molten salt. Other HTF in development include liquid metals, pressurized gas-particle suspensions, supercritical water and carbon dioxide [18].

The most common HTFs for solar thermal power plants are listed in Table 1 and compared in regard to their physical properties and costs. A concise review of the HTFs currently in use and their respective fields of application has been done by Andreas Plumpe in his master's thesis [19]. Please refer to his work for further information regarding HTFs. An overview over common HTFs is given in Table 1.

HTF	T_s [°C]	T_{max} [°C]	ρ (300°C) [kg/m^3]	η (300°C) [mPa·s]	c_p (300°C) [J/(kg K)]	costs
Therminol VP-1	12	400	815	0.20	2319	high
Syltherm 800	-40	400	671	0.47	2086	very high
HELISOL 5A	-65	430	656	0.20	2235	high
Solar Salt	220	600	1899	3.26	1495	low
Hitec	142	535	1640	3.16	1560	medium
Hitec XL	120	500	1992	6.37	1447	medium

Table 1 Characteristics of HTFs in PTC applications [19]

The maximum operating temperature is predominantly limited by the respective HTF chemical breakdown behavior at high temperatures and the deterioration of heat transfer properties. Additionally, every component in contact with the HTF, like REPAs, needs to reliably withstand these conditions. The operating temperatures of some of these fluids are shown Figure 10.

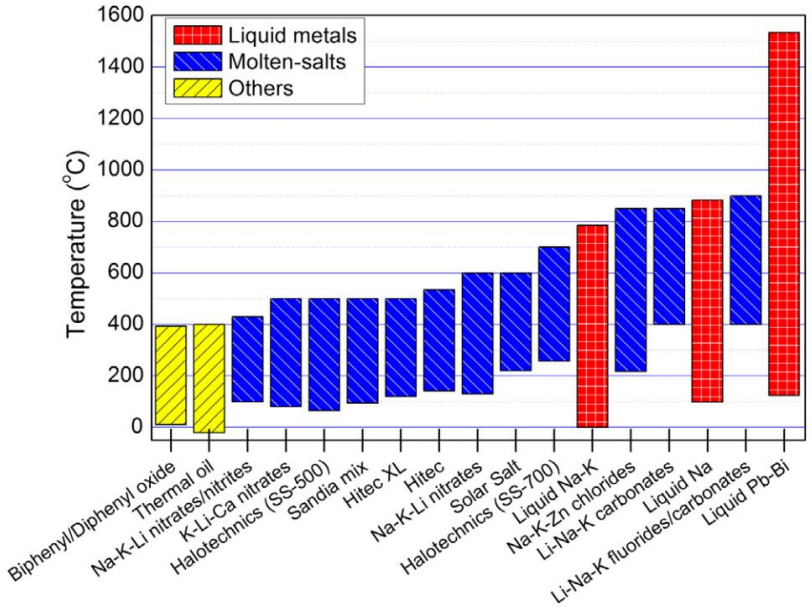

Figure 10 Operating temperatures of various HTF [32]

2.2 Rotation and Expansion Performing Assemblies (REPAs)

The movements of a REPA caused by tracking the sun and the thermal expansion and contraction are shown in Figure 11. Each morning the collector starts in the stow position and is then rotated to start tracking the sun. Throughout the day the SCA readjusts its angle to track the sun and yield maximum efficiency, typically with an accuracy of 0.1° [2]. Every 20-40 seconds the angle is adjusted and in between the trough comes to a standstill. For every single motion the breakaway torque[5] needs to be overcome before the SCA moves. Additional angular adjustments are required to regulate the power plant. If less heat is required than the collectors would provide at the time, the SCA rotation into the optimal focus position is delayed. This so-called “Dumping” is common in commercial PTC plants. These motions are hypothesized to be detrimental to the health of a REPA because the rotating joint frequently switches between static and dynamic friction.

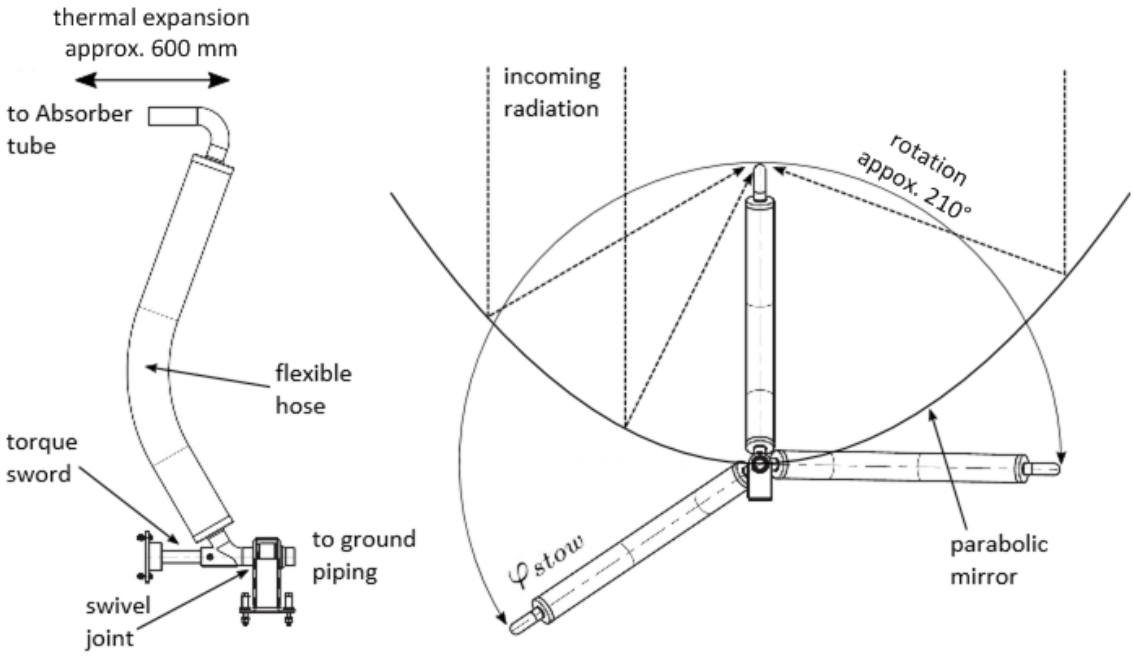

Figure 11 Movement range of a rotary flex hose assembly [20]

A second stress in the component is the translatory movement of the absorber tube due to its thermal expansion. This movement occurs when the tube heats up during

[5] combined static friction of all involved bearings which has to be matched by the drive torque for the assembly to start rotating

the start-up in the morning and cools down after shutdown in the evening. During operation the temperature can fluctuate as well due to changing weather conditions or dumping. But typically these fluctuations are within approximately 13% of the total dilation [19].

While enduring these mechanical loads the REPA itself undergoes the same thermal cycle as the absorber tube and has to operate at a variety of HTF temperatures and pressures during the day, e.g. between the inlet and outlet of a typical SCA the HTF pressure drops from about 30 bar to 20 bar [20]. The most common REPA designs to deal with these stresses are ball joint assemblies (BJA) and rotary flex hose assemblies (RFHA).

The BJA consists of tubes and three ball joints (BJ) which provide the necessary degrees of freedom to compensate both the rotational and translational movement simultaneously. (cf. Figure 12, left). These joints are the critical part of the assembly. While retaining their mobility they also have to be leakproof at HTF operating conditions. For that purpose the inner and outer compression iron seals enclose a soft, injectable sealing. Typically, reinforced graphite is used as sealant to reduce friction and inhibit leakage. A downside of this design is the need for regular refilling of the soft sealing inside the BJ. State-of-the-art BJAs are able to be refilled while at HTF operating pressure in order to avoid a plant shutdown.

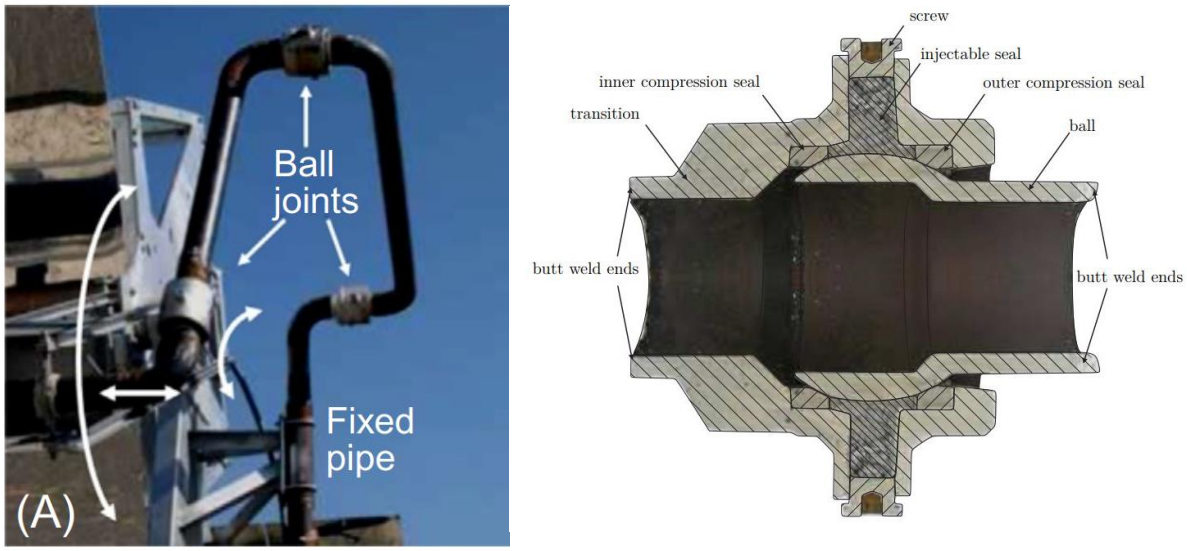

Figure 12 Uninsulated ball joint assembly (left, [21]) and schematic of a ball joint (right, [22])

The RFHA consists of a corrugated, metal hose which is fixed to the absorber tube and connected to the rigid piping with a swivel joint (SJ), which itself is fixed to the SCA's rotational axis with a flat, steel beam interface (cf. Figure 13, left), a so-called torque sword. While the plant-side part of the SJ remains stationary during operation, the hose-side part of the joint is moved by the SCA's drive unit along with the mirrors. The hose consists of an inner corrugated tube with a protective braided metal sleeve around it which acts as a reinforcement and minor thermal insulation (cf. Figure 13, right). Optionally an outer corrugated tube is added to protect the RFHA from detrimental, environmental effects. The joint can compensate the rotational movement, while the hose can accommodate the translational displacement.

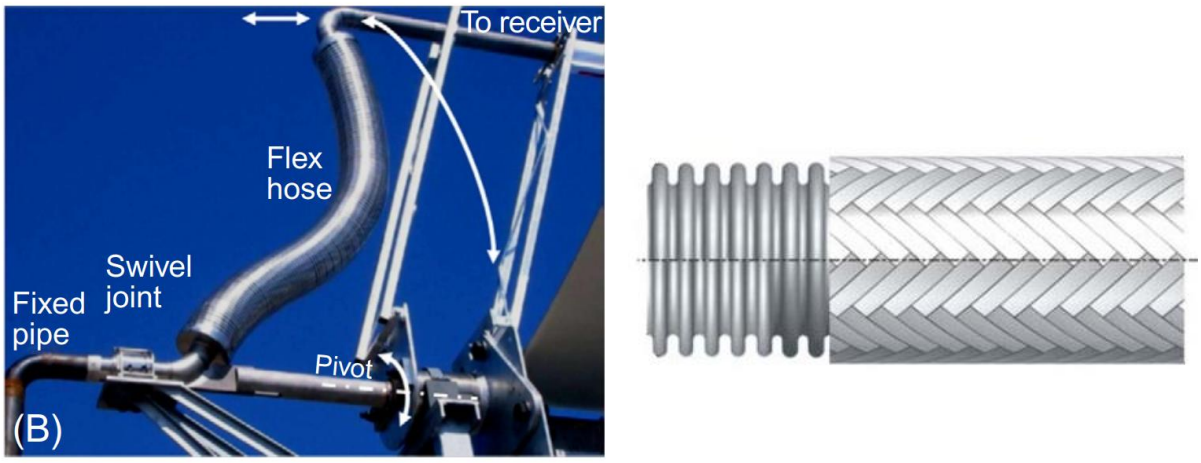

Figure 13 Rotary flex hose assembly (left, [21]) and flex hose design (right, [23])

2.2.1 REPA Testing

A REPA service life is 25 to 30 years. In order to properly qualify these in a reasonable amount of time, accelerated testing needs to be done. There are a few test rigs in the world which are designed to test certain aspects of the REPA or parts of it (cf. Table 2). A concise review has been done by Andreas Plumpe [19]:

"Hyspan Precision Products, Inc. is a US-American manufacturer of flexible tubular metal products. The company operates an endurance test rig for testing ball joints. Using DOWTHERM A (cf. Chpt. 2.1.2), the ball joint is statically wetted (no mass flow) with a pressure of up to 30 bars at the HTF's maximum temperature of 393 °C. These values are close to operating conditions in solar fields. The test objects are cyclically strained with a rotation of 215° and ±7° angular deflection simultaneously.

One cycle has a duration of approx. one minute. It consists of back and forth angular motion from −7° to +7° and of 0° to 215° rotation, back and forth. There are torque sensors installed to measure both the rotational and the angular torque. Also, pressure and temperature are continuously monitored. Designed to perform more than 1000 cycles per day, the endurance testing comprises 11.000 cycles in total which is equivalent to 30 years of power plant operation. The operation / test conditions – representing inlet and outlet of a loop in a solar field – are as follows:

- Condition 1 ("cold header", 6667 cycles): 30 bars and 293 °C
- Condition 2 ("hot header", 4428 cycles): 23 bars and 393 °C

“In spite of the fact that it offers full life cycle testing of ball joints, there are also disadvantageous aspects of this test rig. Ball Joint Assemblies regularly comprise three ball joints performing combined motions. Hence, each of the three ball joint carries out a different (location specific) motion which does not accord with the whole range.

“Using a rubbing wear test rig, IRAtec, a German engineering services provider, investigates the leakage of swivel joints. Therefore, clamping plates are welded on both butt weld ends of the swivel joint. A screwed socket is mounted (to ensure oil supply) as well as two nozzles holding thermocouples. The test object is filled with HTF (Therminol R VP-1) and then installed on the test rig. A temperature of 345 °C is maintained by electrical heaters in the clamping plates, whereas a pressure of 6 bars is applied using a hydraulic hand pump. 15.000 rotation cycles of 20 degrees each (back and forth) are tested. 2000 cycles per day are feasible. There is a load cell measuring the friction force required to perform the rotation. The corresponding torque can be obtained by the length of lever arm between the load cell and the center of rotation. Furthermore, both before and after the test a leakage check by immersing the ball joint in water is performed. Therefore, the ball joint is pressurized with air of 6 bars. Size and quantity of occurring air bubbles are criteria for evaluation. A major drawback of the IRAtec test rig is the pressurization of the swivel joint. The hand pump is only capable to maintain a fluid pressure of 6 bars, which is significantly below PTC loop working pressures (approx. 20 - 30 bars). Furthermore, this is accompanied by an HTF temperature limit, since the vapour pressure of the fluid (around 11 bars at 400 °C) must not exceed the working pressure of 6 bars in

the swivel joint. Hence, the temperature is capped at 345 °C which is too low in order to be able to represent all possible PTC operation conditions. The leakage check is, above that, done with air at 6 bars at ambient temperature; consequently, this test cannot assure seal tightness at real working conditions. Besides thermodynamic properties, the applied motion cycles of 20 ° are not conform with those that appear in power plants. SCAs rather perform rotational motions of up to 120° (distance between vertical position and stow position) in each direction.

“In contrast to the above mentioned testing methods which are targeted on investigating only single components of REPAs, DLR used an existing facility testing an entire Rotary Flex Hose Assembly. The tests were carried out at a HTF test loop at PSA, which consists of six prototype SCEs with a total length of 75m (east-west orientation). The existing REPA at the outlet was substituted with a RotationFlex system made by Senior Flexonics GmbH. The purpose was to gain more detailed information about long term operation properties of the REPA. The RFHA was strained both thermally and mechanically. Heat was provided by focusing the collector to the sun and temperatures were measured both of the HTF at the collector outlet and at the outer surface of the insulated flexible hose. After heating up the HTF to 350 °C which is flowing through both the SCA and the REPA with a pressure of approx. 20 bars, the EuroTrough SCA commences its movement cycles. Based on a rotation cycle defined from 170° (northernmost) to -25° (stow) back and forth, which lasts about 30 minutes, up to nine movement cycles in the course of one day are feasible. By contrast, only one temperature cycle per day can be performed, since the HTF is heated up to operating temperature in the morning and cooled down to ambient temperature in the evening. As there is no auxiliary heating element, the tests are highly dependent on the weather conditions. There are several disadvantages that make this type of test rig unsuitable for durability testing of REPAs. First of all, since the drive is only likely to realize up to nine cycles per day, it would take more than three years to simulate the desired 10.000 cycles of its intended life time. Furthermore, it is highly dependent on weather conditions influencing the progress. It is, above that, impossible to have an influence on the thermal expansion cycles. Also, testing is limited to REPAs for EuroTrough geometry, i.e. the focal length is fixed. Consequently, this kind of testing in not suitable for a

realistic, yet accelerated REPA life time testing in regard to different collector types and time efficiency.

“Senior Flexonics GmbH, manufacturer of, amongst other things, flexible connections for CSP applications, utilizes a kinematics test rig for RFHA. The swivel joints are wetted with stagnant HTF, heated up to max. 550 °C and pressurized up to max. 40 bar. The flexible hose is filled with water at ambient temperature and pressurized up to max. 40 bar. The rotation is applied from −120° (stow position) to 120° (end position) and backwards, which represents one cycle. Simultaneously, the thermal expansion movement is performed from maximum cold position at −14.5° (equivalent to 20 °C) to maximum hot position at +5.5° (equivalent to 400 °C in a PTC application). There are two force/torque sensors; one between the fixture of rotary joint and support (interface 230mm below the rotation axis) and one between the upper end of the flexible hose and the HCE interface. The lack of a mass flow circulating through the test rig diminishes the reliability of the test procedure, since it is to be expected that shear forces due to pipe wall friction have a distinct influence on the lifetime. In addition, Senior Flexonics GmbH utilizes a durability test rig for flexible hoses. Exposed to circulating HTF with a temperature of up to 450 °C and a pressure of up to 40 bars, the test rig simulates the daily thermal expansion of the absorber tubes. However, rotation cycles cannot be applied.

“Associated with the development of molten salt HTF technology in PTC power plants, Abengoa Solar erected a test rig investigating REPAs. Whilst being entirely instrumented with torque, force, temperature, pressure and salt level sensors, the facility exposes the test objects to stagnant molten salt at operating pressure and temperatures similar to desired operation conditions of future commercial plants. Using Solar Salt (cf. Chpt. 2.1.2), the test objects can be pressurized with up to 40 bars, which is equivalent to one and a half times the maximum application pressure. A maximum temperature of up to 500 °C can be reached. The test rig enables a rotational movement of 215° which is induced by a drive unit. The thermal expansion movement can be performed from maximum cold position at 0 mm (ambient temperature) to maximum hot position at 600 mm (500 °C). Yet, after one initial movement from 0 mm – 600 mm, the normal operating range for testing is set to 200 mm - 600 mm. Rotational and expansion movement are performed simultaneously with a duration of two minutes per cycle. The success criterion was specified to

11.000 cycles (30 years of operation) with zero leakage. The first testing phase revealed that exposing the REPAs to the maximum pressure (40 bar) and temperature (500 °C) leads to plentiful failures. Hence, a more sophisticated testing plan was developed implementing step by step increases of the boundary conditions. Additionally, a distinction was made according to SCA inlet and outlet conditions. There have been tests with various BJAs and RFHAs, yet no configuration proved to withstand the boundary conditions. According to Abengoa Solar, the development depends on finding a pliable seal material that is qualified for 500 °C molten salt. It could be manifested that no BJA was successfully tested at elevated temperatures due to exalted leak rates. Yet, there was partial success in testing RFHA: Using a swivel joint with face seal design, a cycle testing was successfully carried out in 10 °C temperature increments up to 480 °C. The leak rate was less than one gram per hour. Furthermore, a life cycle test showed that 2855 cycles could be performed before the leak rate of the swivel joint exceeded the allowable level of 10 grams per hour."

	Hyspan	IRAtec	DLR	Abengoa Solar	Senior Flexonics
Component	BJ	SJ	RFHA	RFHA/BJA	RFHA
HTF	DOWTHERM A	Therminol VP-1	Slytherm 800	Solar Salt	Therminol VP-1[6]
HTF circulation	no	no	yes	no	no[7]
p_{max} [bar]	<30	6	20	25	40
T_{max} [°C]	282	345	300	550	550
Rotation	yes	yes	yes	yes	yes[8]
Translation	yes	no	yes	yes	yes[8]
Cycles	11.000	15.000	321	11.000	ca. 11.000

Table 2 Overview of existing REPA test benches [19]

[6] for rotation tests the flex hose if filled with water at ambient pressure and operating temperature

[7] circulation is only done for the thermal expansion simulation of the flex hose

[8] not simultaneously

A summary of the results of Plumpe's review is listed in Table 2. Based on this review, the main limitations of existing test rigs can be identified as follows:

- inability to properly represent hydraulic conditions of a solar field regarding temperature, pressure and volume flow
- impractical life cycle test durations
- inability to expose the REPA to all mechanical and thermal loads simultaneously

So, for more complete and representative life cycle assessments, a test rig was devised that can circulate HTF with temperatures up to 450 °C and pressures up to 40 bar through two REPAs. The components can be rotated within a range of 205° and a translational motion of up to 1 m can be realized, depending on the variable focal length. It has been commissioned at the PSA and the rotation can be executed in incremental steps to simulate the small movements of the sun-tracking. Additionally, the components are subjected to the environmental conditions of a solar power plant, e.g. dust, wind and humidity. The only factors not regarded in the test bench are rain, wind and spillage, the occasional, inadvertent exposure to concentrated sunlight due to focal misalignment. These effects are considered negligible, compared to the thermal and mechanical operational load [20]. The test rig used in this thesis is based on that design.

3 Experimental Setup

3.1 Test Rig

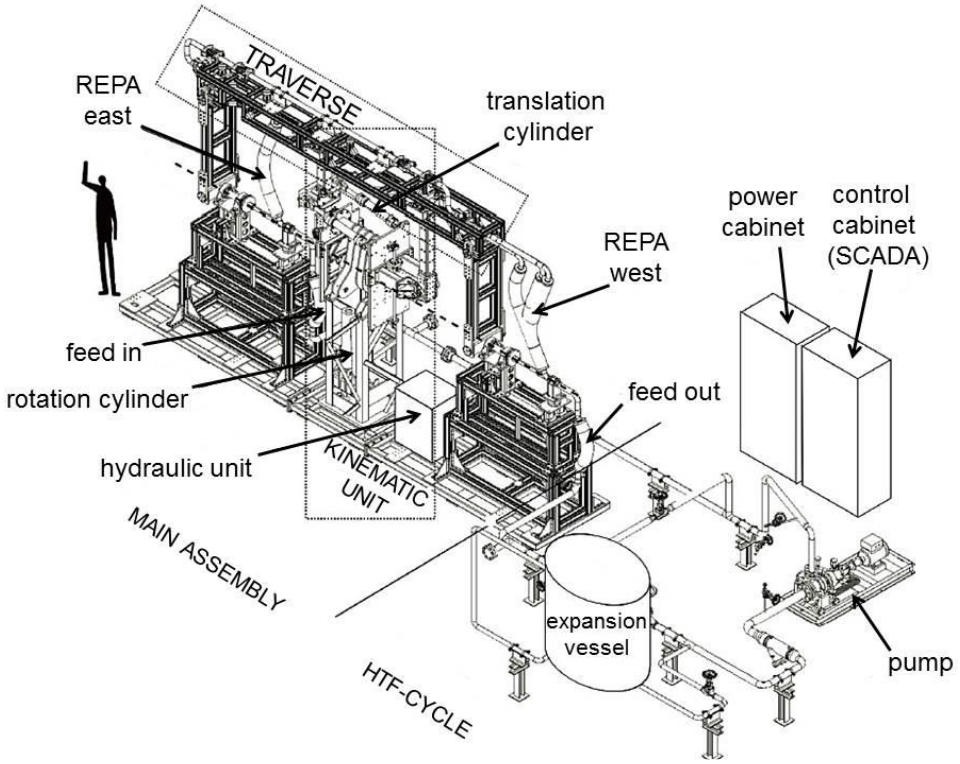

Figure 14 Isometric view of the REPA test rig at PSA [19]

The test bench, shown in Figure 14, can be subdivided into two major sections: the HTF cycle and the main assembly. The former contains a magnetic coupled pump, which can produce flows ranging from 6 to 60 m³/h, and six electric band heaters with 3500 W power each. It is able to heat up synthetic thermal oil up to 450 °C and pressurize it to 40 bar, which exceeds the conditions present in solar power plants. The peak maximum operating conditions of a REPA for temporary loads are 40 bar and 400 °C and 35 bar and 400 °C as static maximum operating conditions [20]. The test bench is designed to withstand HTF temperatures of up to 500 °C. An expansion vessel filled with nitrogen gas is deployed to keep the HTF pressure stable while compensating for the thermal expansion of the HTF. The fluid is kept at the required parameters for the test and circulated through the main assembly.

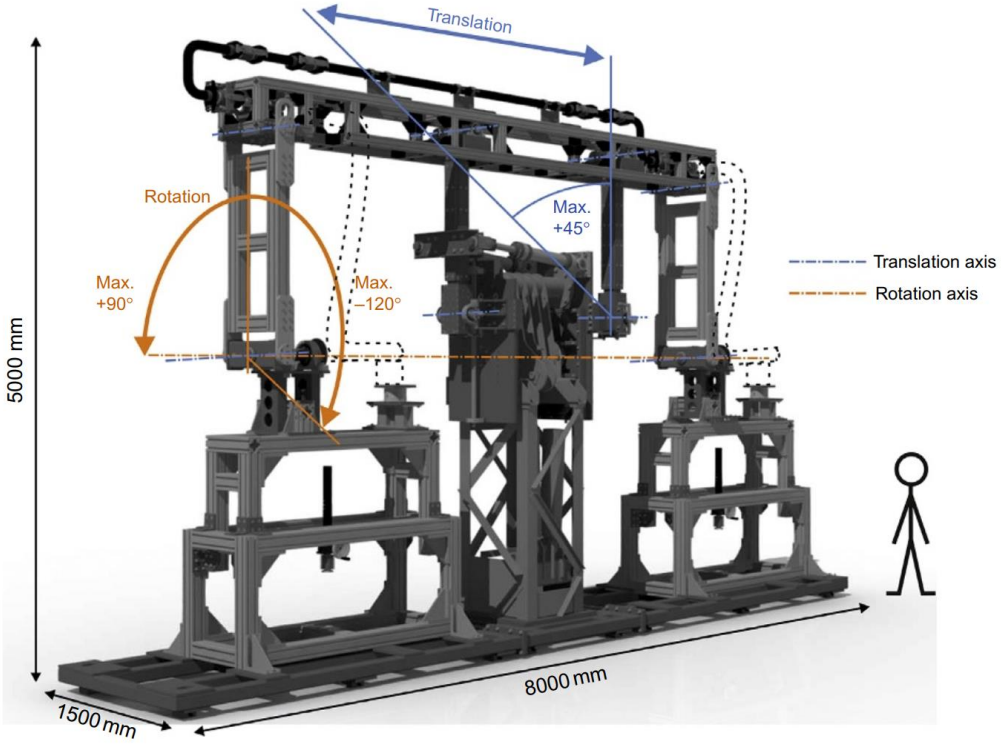

Figure 15 Kinematic unit of the REPA test rig [21]

The main assembly mainly consists of a traverse with HTF piping and a kinematics unit (KU), which encompasses a hydraulics control unit and four hydraulic cylinders (cf. Figure 15). The KU is used to move two REPAs according to the test cycle while HTF flows through them. Two of the hydraulic cylinders are within the drive pylon and rotate the traverse. The traverse containing the HTF piping is connected to the rotational axis of the KU via two steel arms. Two hydraulic cylinders are mounted between one of these arms and a front end plate to power the translation which simulates the thermal expansion. The arm length can be adapted so that different focal lengths, the distance of the HCE to the base of the parabolic mirror, can be tested within a range of 1.5 to 2.3 m. Angular positions are measured with a magnetic band scale sensor from ASM (rotation) and a rotary shaft encoder manufactured by INDUcoder (translation). The range of rotational motion is 205° and the translational cylinder can cause a traverse tilt of up to 45°. Regarding the translatory movement the range is not fully utilized since currently a REPA only needs to be tested for a thermal expansion of about 450 mm [20]. For a detailed insight into the mechanical design of this test bench please refer to the master thesis of Andreas Plumpe [19].

3.1.1 SCADA System

The entire test bench is controlled with a SCADA system (cf. Figure 16). The main component of it is a Siemens S7-300 PLC. The latter sends start/stop and velocity inputs to the servo controller, controls the HTF pump speed, runs the control algorithms for the movement cycles, as well as gathers measurement data. PLC variables can be read and written via an OPC server which is connected to a graphical user interface (GUI). The GUI is programmed in LabVIEW and allows for remote control of the test bench. This system was largely designed by Tobias Hilbel in the course of his bachelor thesis. Please refer to his work for further information [25].

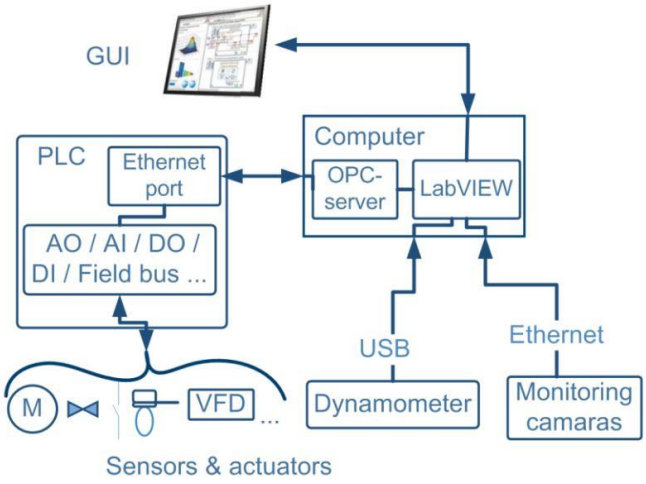

Figure 16 Overview of SCADA system [24]

3.1.2 Hydraulics Unit

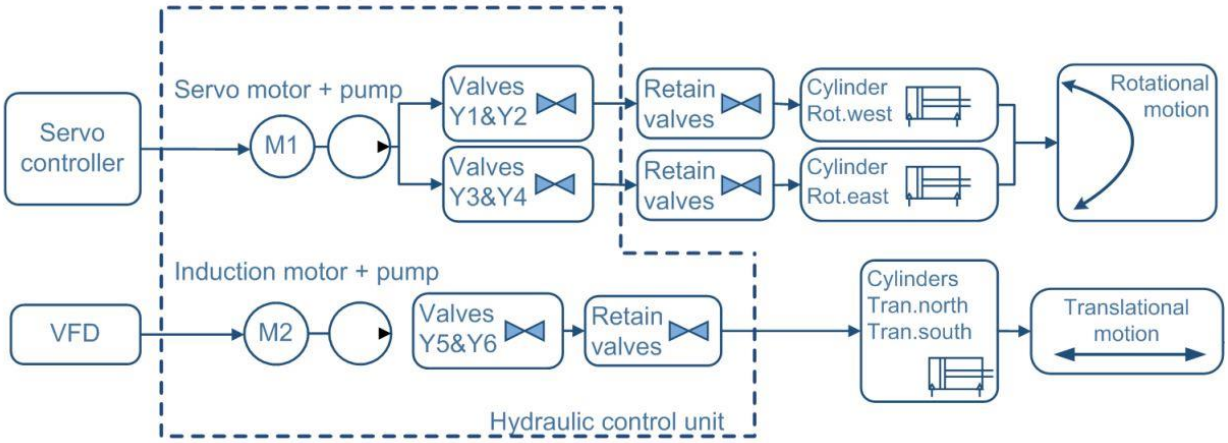

Figure 17 Hydraulics control unit [24]

The rotation is actuated with a servo drive and the translation by an inverter drive system (cf. Figure 17) by LTI motion. The motors powers ELIKA gear pumps which transport the hydraulic oil into the cylinders. Each pump transports 7 ml of oil per revolution. The amount of oil flowing into the individual cylinder is determined by the geometrical configuration. 4/3 directional control valves regulate whether a cylinder piston is being extended or retracted. This cylinder configuration sets the direction of the traverse movement (cf. Table 3). A detailed circuit diagram of the hydraulic control unit is attached as Appendix A.

Rotation section	West cylinder	East cylinder
-20° to 35°	pull/push[9]	pull/push
35° to 133°	pull/push	push/pull
133° to 180°	push/pull	push/pull

Table 3 Cylinder switch points

If the hydraulics system is not pressurized the cylinder retain valves are shut and the traverse is held in position by the cylinders.

[9] Traverse moving away from/towards stow position

The servo controller controls the servo motor speed, i.e. the gear pump speed, by controlling the servo motor torque. This speed is directly proportionate to the combined piston speeds of the rotation. The rated speed of the servo motor is 3000 rev/min. The servo power term used in this work is scaled to this, e.g. 1500 rev/min equals 50% servo power. The motion profile of the motor is determined by the power combined with the acceleration and deceleration ramps (cf. Figure 18). These ramps can be set independently.

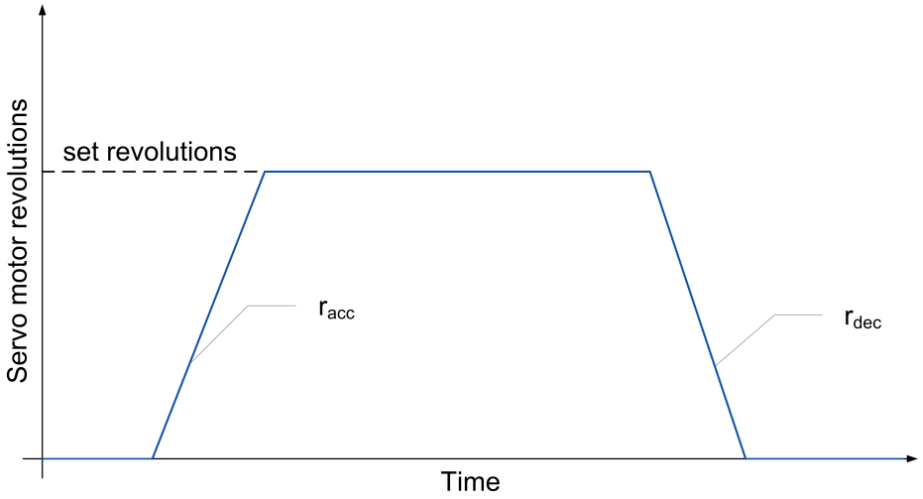

Figure 18 Servo motor motion profile

3.1.3 REPA test cycle

Figure 19 depicts the rotation of a trough during the day. It starts in stow position φ_{stow}, typically 20° below the horizontal level, with its mirrors facing down. This is the preferable stow position since it minimizes the wind-exposed areas and protects the mirrors. At the beginning of the day the PTC is quickly rotated into the φ_{start} position where it can concentrate enough sunlight to operate the power plant. Then it starts tracking the sun, guided by mathematical models and measurement devices, to maximize its efficiency throughout the day. This continues until φ_{stop} is reached at the end of the day, when the sunlight is not sufficient enough to heat up the HTF to the necessary temperatures. After that point the PTC swiftly rotates back into stow position, where it stays for the night and cools down.

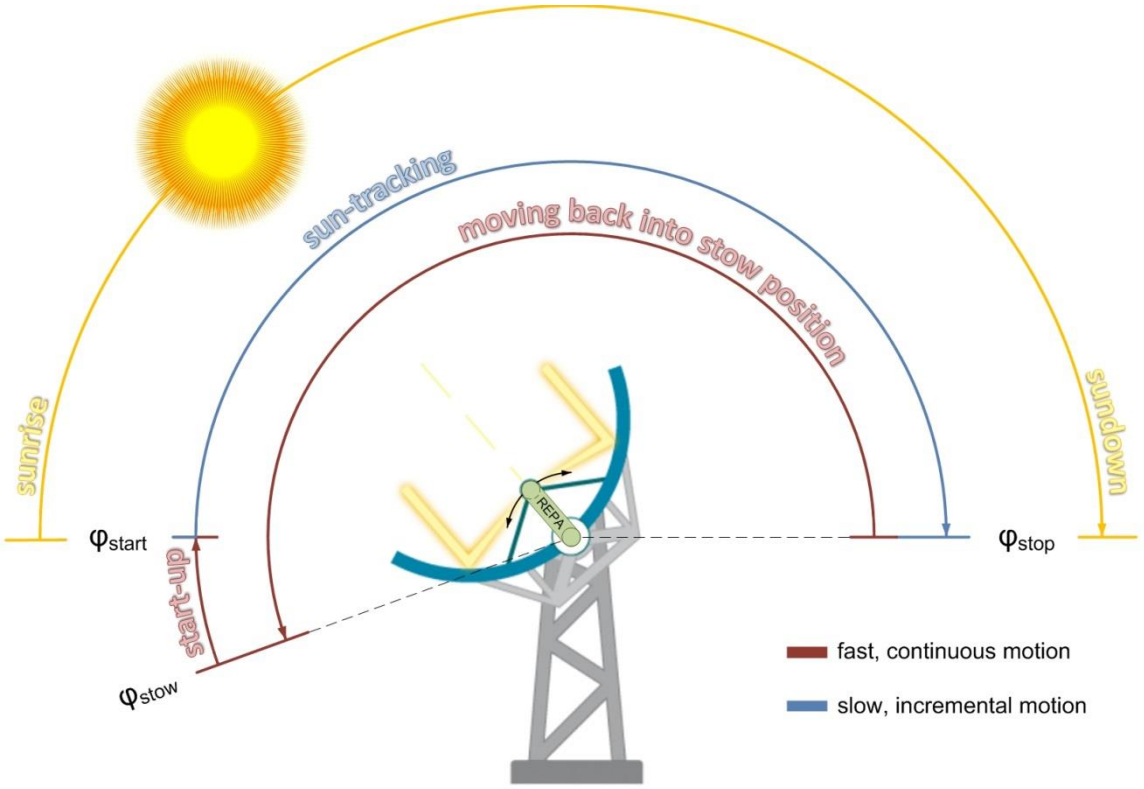

Figure 19 Typical 24h rotation cycle of a PTC (PTC structure from [25])

The starting angle φ_{start} and stopping angle φ_{stop} are different for each solar power plant, since they largely depend on the geographical location, not just latitude and longitude but also the landscape, e.g. mountain ridges can overshadow the solar collectors for low sun levels. They may also change with the season because the azimuth angle changes throughout the year. So, the stresses a REPA has to endure during its lifetime are specific to the location. The REPA test rig is able to run customized test cycles with a minimum φ_{stow} of -20 ° and a maximum φ_{stop} of 180° to simulate the life cycle for specific locations.

The translatory expansion movement is carried out at the beginning of the sun-tracking phase and the contraction starts simultaneously with the motion back into stow position. This simulates the heating up and cooling down of the PTC absorber tube at the beginning and the end of a day, respectively.

3.2 Measurement Technology

There are two types of measurement systems installed in the REPA test rig: Those which measure the influences on the REPA being tested, e.g. temperatures and forces, and those which are necessary for a proper and safe operation of the test bench, like position and vibration sensors.

3.2.1 Dynamometer

The forces and moments acting on the REPA are being measured by K6D175 dynamometers by ME-Messsysteme GmbH. It can measure forces in all three spatial dimensions up to 10 kN and the corresponding moments up to 1 kNm. For the technical specifications please refer to Appendix B.1.

This device uses several strain gauges to measure the three-dimensional forces and moments. A strain gauge changes its ohmic resistance when deformed. This change in resistance can be measured by a Wheatstone Bridge[10]. To determine the stresses in all directions, three gauges are arranged in a rosette layout (cf. Figure 20). Since the elastic modulus, Poisson's ratio and the k-factor of the gauges, the ratio of the relative change of electrical resistance to mechanical strain, are known, the stresses affecting the sensor can then be calculated from the measured electrical current [27].

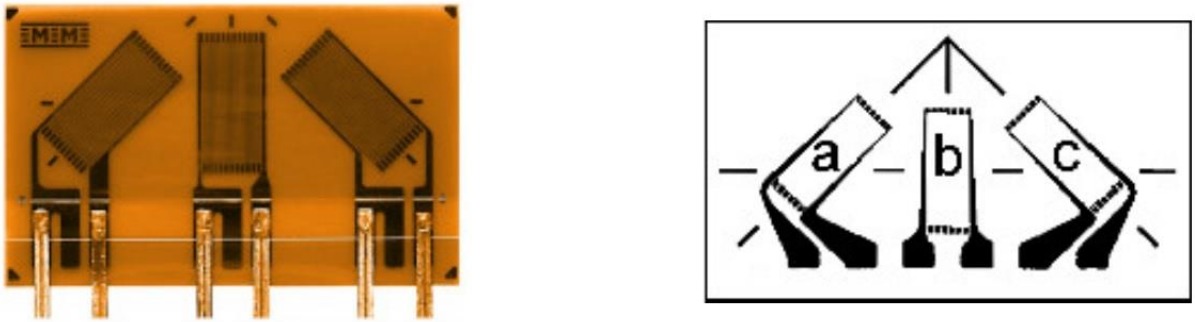

Figure 20 Strain gauge rosette [26]

[10] Electrical circuit which can measure ohmic resistances

There are currently two of these dynamometers at the west side REPA, one at each end. An additional two can be placed at the east side REPA in the future. On the left side of Figure 21 the position of these sensors are depicted. These locations enable the sensors to measure the stresses acting upon the fixed bearing of the pipe support. These are the combination of the forces and moments acting on the HTF piping and the REPA. Previously, simulations with the ROHR2 simulation software have been created and validated for the traverse by Thore Müller [20] and Christian Schütt [28] and thus the stresses of the traverse are known. Thereby the forces exerted upon the upper bearing caused by the traverse piping can be calculated. In order to calculate the forces and moments at the foot of the REPA another simulation of the lower piping has been done. The right side of Figure 21 shows in detail how the dynamometer is fixed to the piping. A key part in this design is the thermal insulation. It is a ceramic plate inserted in between the sensors surface with the strain gauges and the piping which, due to the HTF flow, heats up to temperatures above the operational limit of the K6D175 of 85 °C. The ceramic plate itself is not able to provide the necessary insulation of the sensor by itself but has to be actively cooled with a fan. This setup creates an offset of 137 mm from the location where the forces are acting on the REPA but this can be accounted for within the GSVMulti software of ME-Messsysteme which interprets the signals of the dynamometers.

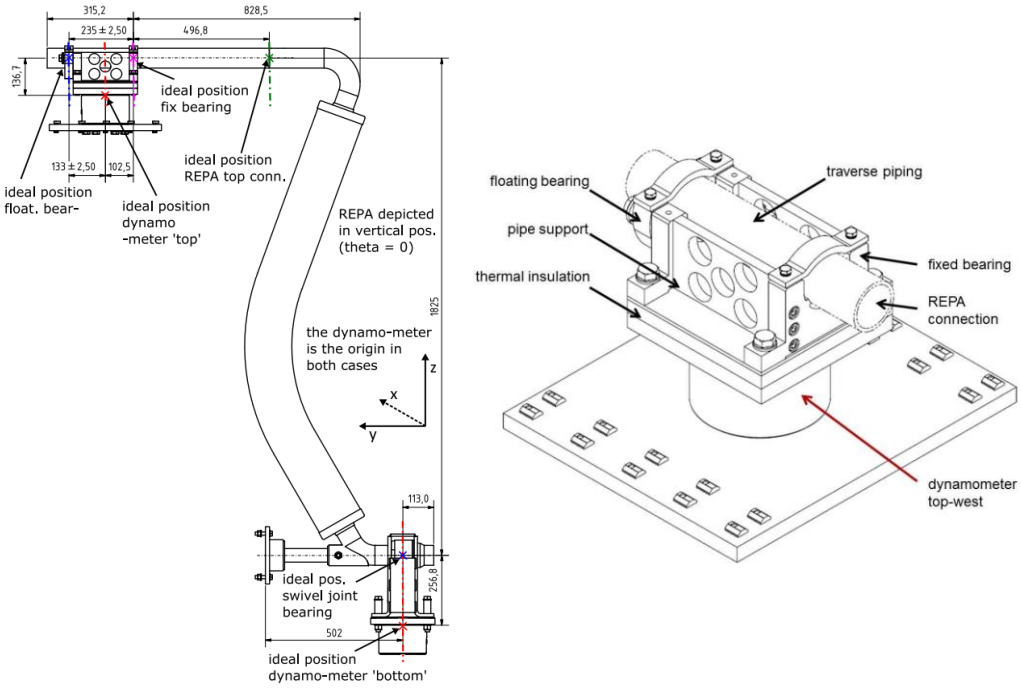

Figure 21 Position of the dynamometers [20] and a detailed view of the dynamometer fixation [27]

The operating temperature affects the accuracy and validity of the measurement results. Extensive analysis and calculations regarding this dynamometer uncertainty have been previously done by Thore Müller [20]. There are measurement uncertainties affecting the zero signal and the characteristic as well as uncertainties induced by the temperature [20]: In the course of his thesis important improvements were made, like cooling the sensor, improving the insulation and the re-calibration and validation of the sensor for high operating temperatures. As a result of these actions the measurement uncertainty was reduced. Figure 22 shows an exemplary dynamometer measurement.[11] The shaded areas around the individual plot lines mark the uncertainty of these results according to the previously mentioned calculations. The interval indicates a 95% certainty.

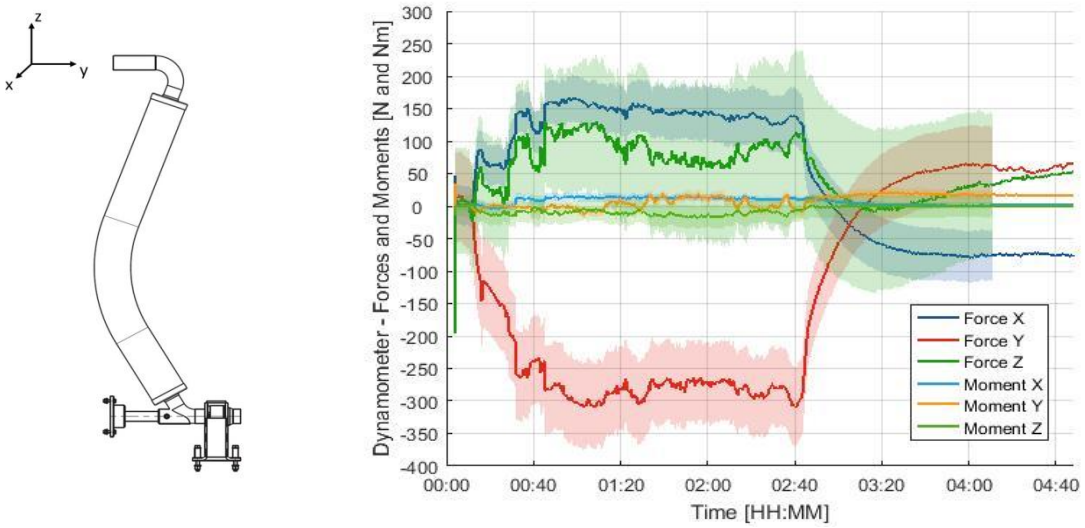

Figure 22 Orientation and sample results for a dynamometer measurement [20]

3.2.2 Vibration Sensors

The weight of the frame of the traverse, the HTF piping and the arms of the KU exert a moment of about 32 kNm onto the axis of the drive pylon. In order to balance this one-sided load a counterweight (CW) has been designed and implemented (cf. Chpt. 4.1). The motion of the test rig, especially the step-by-step tracking motion, causes the drive pylon to oscillate. Without the CW the pylon exhibited a lateral displacement

[11] taken from a temperature response experiment

of about 3 mm during one 180° rotation. It illustrates the stresses applied to the drive pylon during operation and the hydraulics system. Considering the length of an entire REPA life cycle and that the test bench is to be run continuously, these loads can cause a fatigue failure. A good gauge of the assembly's health are the vibrations of the structure. If constantly monitored, dangerous trends, e.g. increasing oscillation amplitudes, can be registered in time and preemptive measures can be taken, e.g. reinforcing the pylon. Another important factor to be considered is resonance. If the motion causes an excitation of the drive pylon with a resonance frequency, the loads will lead to structural damage of the test rig.

In order to accurately measure the vibrations and enable online monitoring an IDS Innomic KS943B.100 accelerometer was installed. It can measure the acceleration in by using piezoelectricity. If a piezoelectric material is stressed it produces an electrical charge. As seen in Figure 23 a seismic mass is connected to the piezoelectric element. Once accelerated by the vibrations, it exerts a force upon the piezoceramic due to its inertia. Since the mass is known and the force is measured via the piezoelectric effect, a simple calculation according to Newton yields the applied acceleration [28]. The higher the seismic mass, the higher the sensitivity of the sensor. But it also decreases the resonance frequency and thereby the operational range of the device. The sensor in question uses this same principle to measure it in all three spatial dimensions, has a limiting resonance frequency of 32 kHz, a measurement range of ± 60 g[12] and an accuracy of ± 5 % [30].

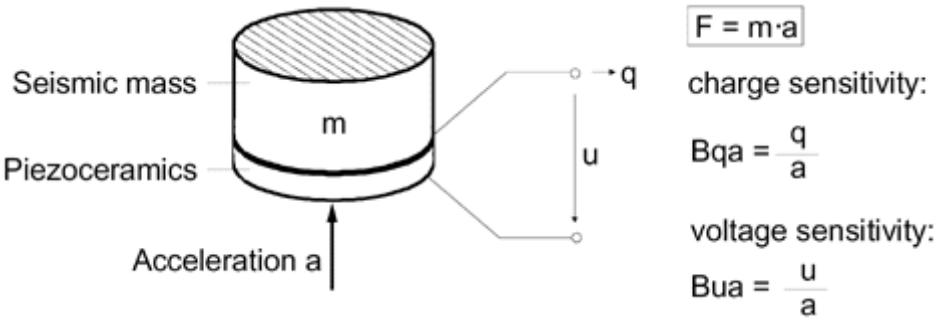

Figure 23 Basic operating principle of a piezoelectric accelerometer [28]

Further details on this sensor can be found in Appendix B.2.

[12] gravitational acceleration of earth (9.81 m/s²)

4 Test Rig Optimization

The optimization of the test rig can be split into two sections: mechanical improvements and PLC control algorithms. As mechanical improvement to enhance the test rigs durability, a counterweight to balance the traverse is designed, mounted and tested. The CW tests reveal clearances in the hydraulic cylinder bearings which cause dangerous traverse oscillations which prohibit a safe long-term operation. Therefore these bearing are re-designed to reduce the play of the KU.

In the second part, the step-by-step movement of the tracking motion is realized by timing the runtime and stop time of the servo motor. The hydraulic drive is analyzed in regards to its motion profile and hardware limits to minimize the timings and therefore minimize the overall REPA test cycle time. PID controllers are implemented to ensure the cycle produces steady, reproducible motion sequences over the entire arc as well as in subsequent test cycles.

4.1 Counterweight

4.1.1 Counterweight Design

As mentioned in Chpt. 3.2.2, measurements have shown a lateral displacement totaling 3 mm at the top of the drive pylon for a full 180° rotation. To reduce this movement and increase the durability of the test rig, counterweights are designed to balance the traverse (cf. Figure 24). A back-of-the-envelope calculation yielded a maximum weight moment at the rotational axis $M_{g,max}$ of 32 kNm. The CW assembly is offset from the traverse by 180° and generates an opposing momentum which ideally negates the torque at the rotational axis caused by the excentrical traverse mass.

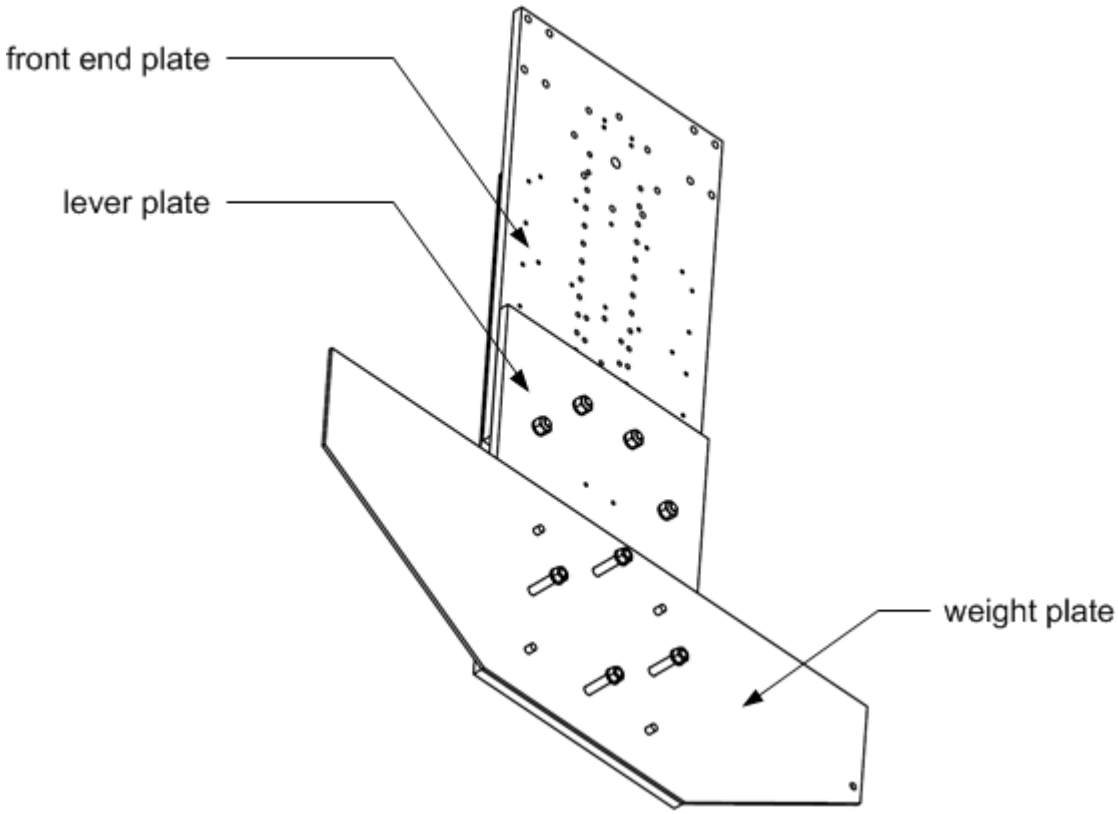

Figure 24 Counterweight assembly with one weight plate

The CW consists of two identical assemblies mounted to both sides of the drive pylon: The lever plates of the counterweight are mounted onto the front-end plates of the drive pylon, the same plates which carry the rotary arms. The CW consists of multiple plates mounted onto these lever plates and fixed by nuts and bolts (cf.

Figure 25). That way it is easily adapted in case of weight changes on the traverse side by removing or adding weight plates.

Figure 25 Mounted 8L-CW at 180° traverse position

Four 20 mm and four 10 mm thick weight plates per side are necessary to generate the calculated 32 kNm momentum. The weight of the lever plate and its influence on the torque are factored in as well. The counterweight is classified according to the number of weight plates mounted, e.g. for an 8L4S-CW, 8 large and 4 small weight plates are mounted onto each lever plate (cf. Table 4). The individual masses of the CW components are listed in Table 4.

Abbreviation	Component	Weight [kg]
-	lever plate	223
S	10 mm weight plate	94
L	20 mm weight plate	188

Table 4 Counterweight masses

The technical specifications of the CW are attached in Appendix C.1.

4.1.2 Forces and Moments at the Rotation Axis

The counterweight reduces the load on the hydraulic cylinders and the drive pylon. A balanced traverse reduces the moment onto the rotational axis caused by the eccentric center of mass of the traverse. This affects the servo torque, i.e. piston forces, necessary to rotate the assembly. For raising the traverse, the hydraulics unit has to counteract gravity while for a downward motion the gravitational moment of the traverse supplements the drive torque in moving the traverse. The magnitude of that moment is determined by the horizontal lever between the traverse center of mass and the rotational axis. It is proportional to the cosine of the rotational angle. Accordingly, the maxima of the gravitational moment occur when the traverse is in a horizontal position and the minimum at 90°. For the entire motion range, this equals:

$$M_g = M_{g,max} * \cos(\varphi) \tag{4.1}$$

Besides gravity, the effective levers of the hydraulic cylinder forces onto the rotational axis are another angle-dependent influence on the servo motor torque. The discontinuity is caused by the geometrical boundary conditions between the cylinder/traverse interface and the cylinder bearings in the drive pylon. The generated moment is proportional to the respective effective lever between each piston and the rotation axis (cf. Figure 26).

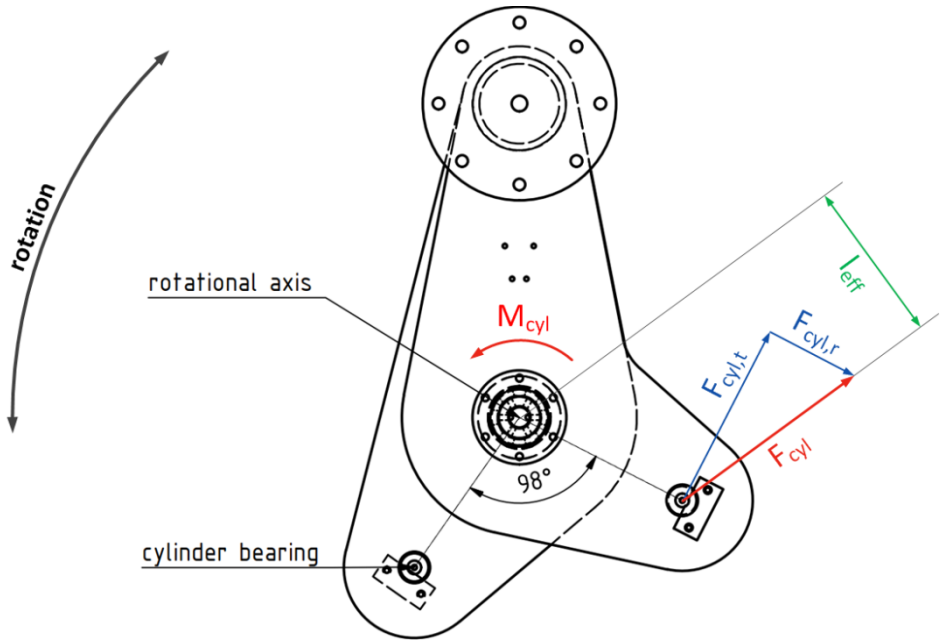

Figure 26 Forces at cylinder/traverse interface (vertical traverse position)

These effective levers for both cylinders and their sum are plotted over the motion range of 200° in Figure 27. As the hydraulic systems of both cylinders are hydraulically connected, their internal pressure is the same, if their retain valves are open. Therefore the piston forces are equal as well since the hydraulic cylinders are of an identical geometry. Only the tangential components of these forces contribute to the rotation. Then the distribution of the necessary torque onto each cylinder only depends on the levers:

$$M_{cyl} = 2 * F_{cyl} * (l_{eff,east} + l_{eff,west}) \tag{4.2}$$

The torque necessary to start moving the traverse can be calculated with a moment balance at the beginning of a traverse motion including the static bearing friction of the axis:

$$M_{cyl} = M_{friction,stat} + M_g \tag{4.3}$$

The servo motor torque is proportional to the hydraulic pressure and thereby the piston forces. By that fact this proportionality can be derived:

$$M_{servo} \sim \frac{M_{cyl}}{(l_{eff,east} + l_{eff,west})} \sim \frac{M_{friction,stat} + M_g}{(l_{eff,east} + l_{eff,west})} \tag{4.4}$$

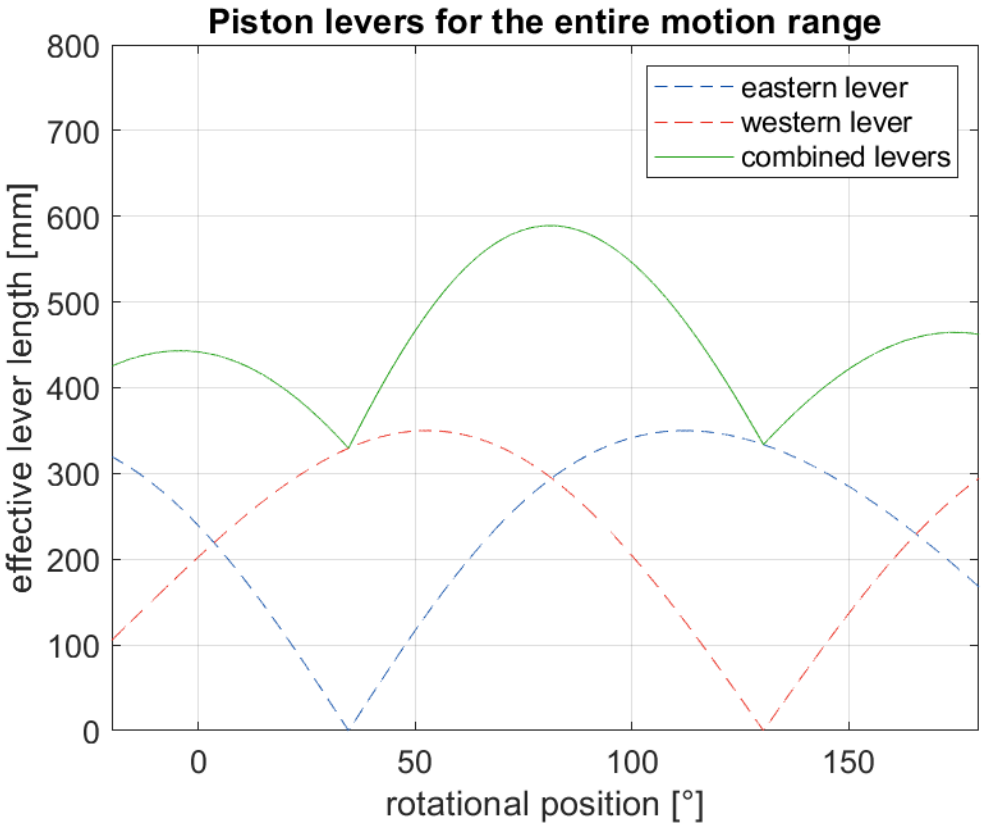

Figure 27 Effective levers of the piston forces

The correlation from Equation 4.4 is depicted in Figure 28. The results of the calculations are shown for three different maximum gravitational moments correlating to different counterweights, including the moment of the unbalanced traverse ($M_{g,max}$ = 32 kNm). The static bearing friction is assumed as an unknown constant independent of the rotational position. For the calculations a static friction value of 5 kNm is assumed since it cannot be measured directly. Beyond 90° the gravitational moment supplements the rotation and counteracts the friction. If $M_{g,max}$ is greater than the static friction moment, it can fully negate it. In that case no cylinder forces are needed to rotate the traverse and the servo motor torque is zero[13]. The lower $M_{g,max}$ show the expected impact of the CW on the servo load. A more balanced traverse, i.e. a traverse exerting a lower gravitational moment at the rotation axis, results in a steadier servo torque with significantly lower maximum values (cf. blue line in Figure 28).

[13] According to the correlation in Eq. 4.4 it is negative because the moment balance is calculated for the time when the traverse just overcomes the breakaway torque, i.e. the traverse is not actually moving. The servo motor would need to counteract the rotation in order to prevent the traverse from rotating.

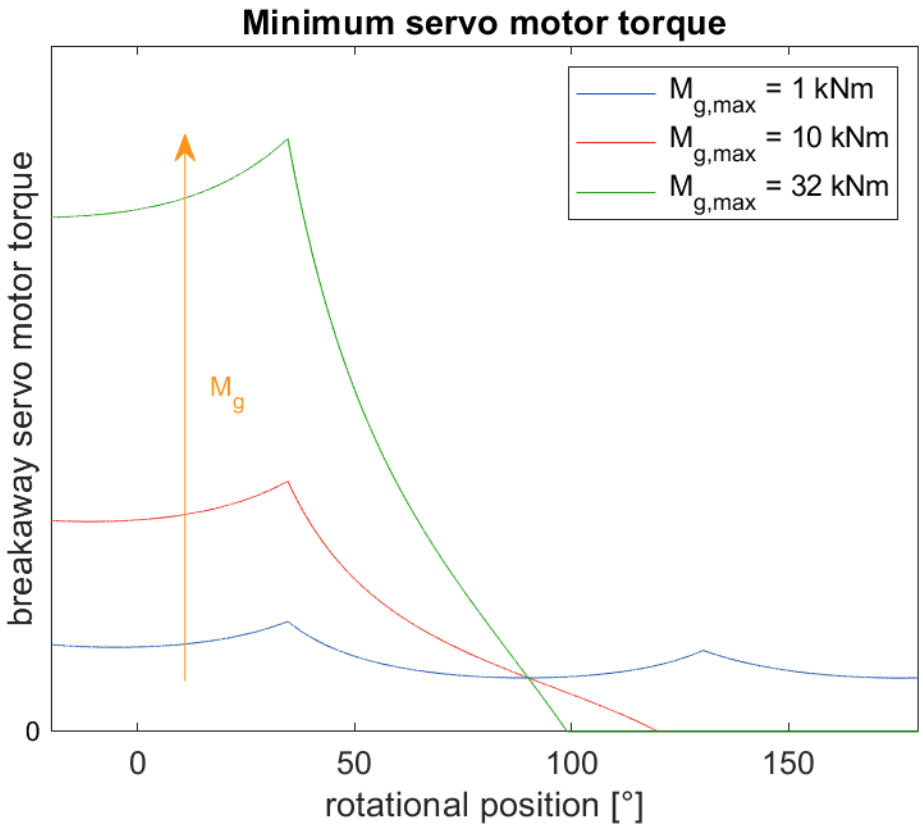

Figure 28 Breakaway servo motor torque for various gravitational moments

4.1.3 Results

Figure 29 shows the torque applied by the servo motor for a continuous rotation from -20° to 175° at 20% motor speed prior to the installation of the CW. The maximum measured torque exceeds the rated servo motor torque of 10.5 Nm, but is still below the maximum torque of 36 Nm [31]. Additionally, these tests were conducted without the additional load of two REPAs and the HTF flowing through them and the traverse piping. The two irregularities at 33 and 115 seconds are caused by the necessary switch of the respective cylinder from pull to push (cf. Chpt. 3.1.2). During these phases the combined effective levers reach a minimum. At the first switch point the servo motor torque needs to increase accordingly to generate a constant moment at the rotation axis (cf. Chpt. 4.1.2). This necessary moment for moving the traverse up exceeds the one for lowering it by up to a factor of three. The disparity between the upward (first 80 seconds in Figure 29) and the downward motion supports the hypothesis from the previous chapter that gravity is primarily determining the angle dependence of the servo torque, not the effective levers of the piston forces.

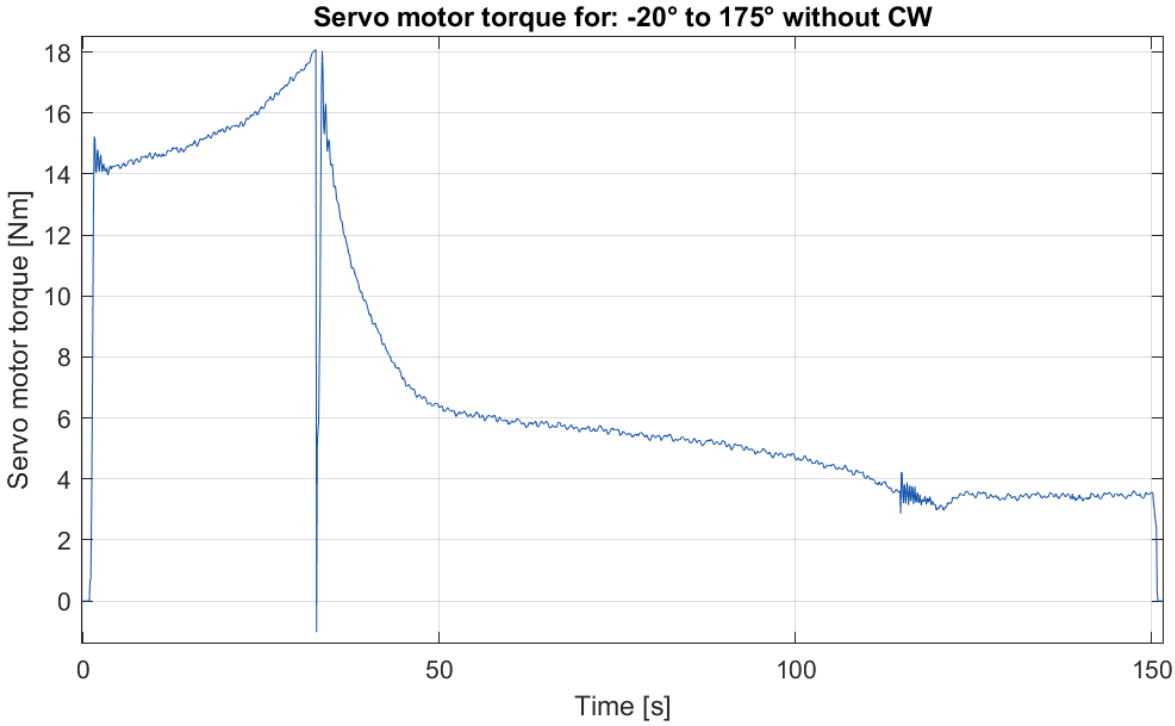

Figure 29 Servo motor torque for one rotation without counterweight

The servo torque drops at the first switching point due to clearances in the east cylinder bearings. When the cylinder is switched from pull to push, it needs to extend the piston for the sum of the clearances before the contact between cylinder and cylinder/traverse interface is reestablished again. During that process the east cylinder is unloaded and the west cylinder, which is still in contact with the cylinder/traverse interface, holds the traverse in position.[14] The sudden load reduction causes a rapid decline in the torque measurement (cf. Figure 30). The first measurement value after the switch is negative which indicates a change of direction of the servo torque. This is due to the PID controller of the servo controller because with the load reduction the previously set torque caused the actual servo power to increase to 43%, exceeding the set velocity by a factor of 2.15. This deviation from the setpoint causes the controller to reduce the torque accordingly (cf. Chpt 3.1.2). Before the contact with the interface is reestablished the servo motor move an unloaded cylinder and afterwards it needs to increase the torque again to start

[14] The west cylinder does not move because both cylinders are hydraulically linked (cf. Appendix A). The hydraulic oil is pushed into the east cylinder because it is the path of least resistance.

moving the traverse. The oscillations after the switching point are attributed to the PID controller.

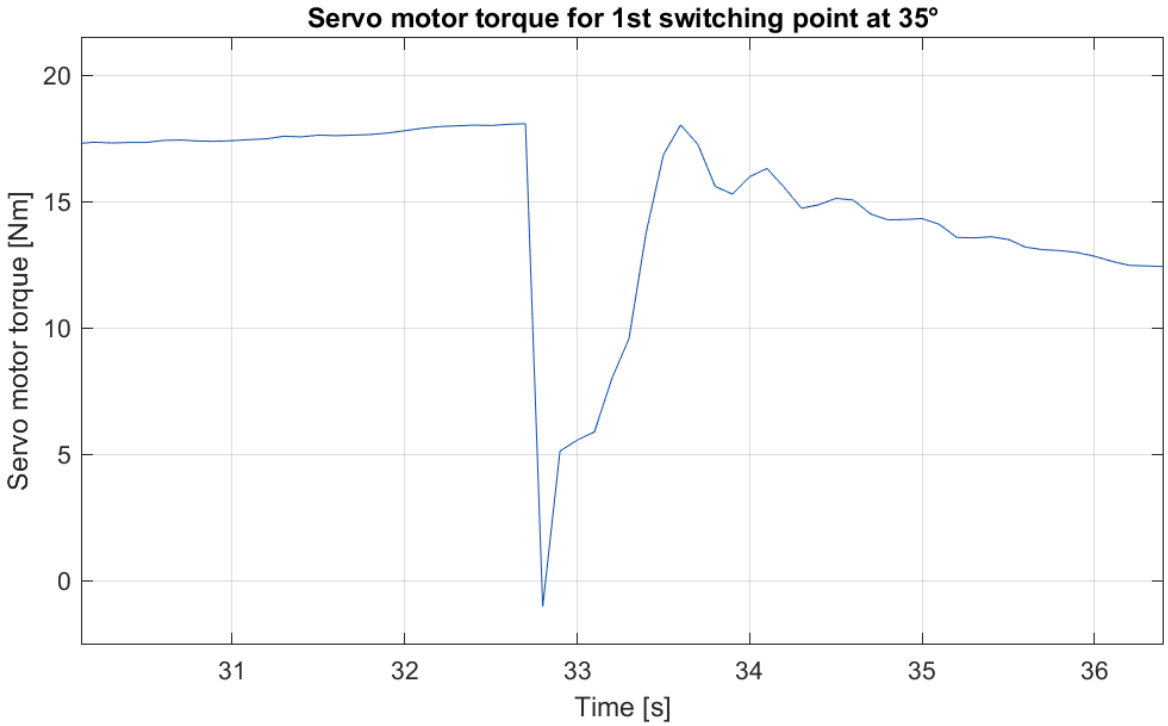

Figure 30 Torque measurement at first switching point

At the second switch point, when the west cylinder switches from pull to push, the torque exhibits a smaller decrease compared to the first switch point (cf. Figure 31). In this case the overall load of the cylinders is lower.[15] The smaller load reduction causes a maximum servo power deviation from the setpoint of 15% which results in a smaller torque adjustment of the servo controller. The subsequent torque oscillations are the result of the PID response.

[15] During this test the traverse is being lowered at the second switch point. For a rotation in the opposite direction the load proportions would be reversed. The loads at the 133° switch point would be higher than at 35°.

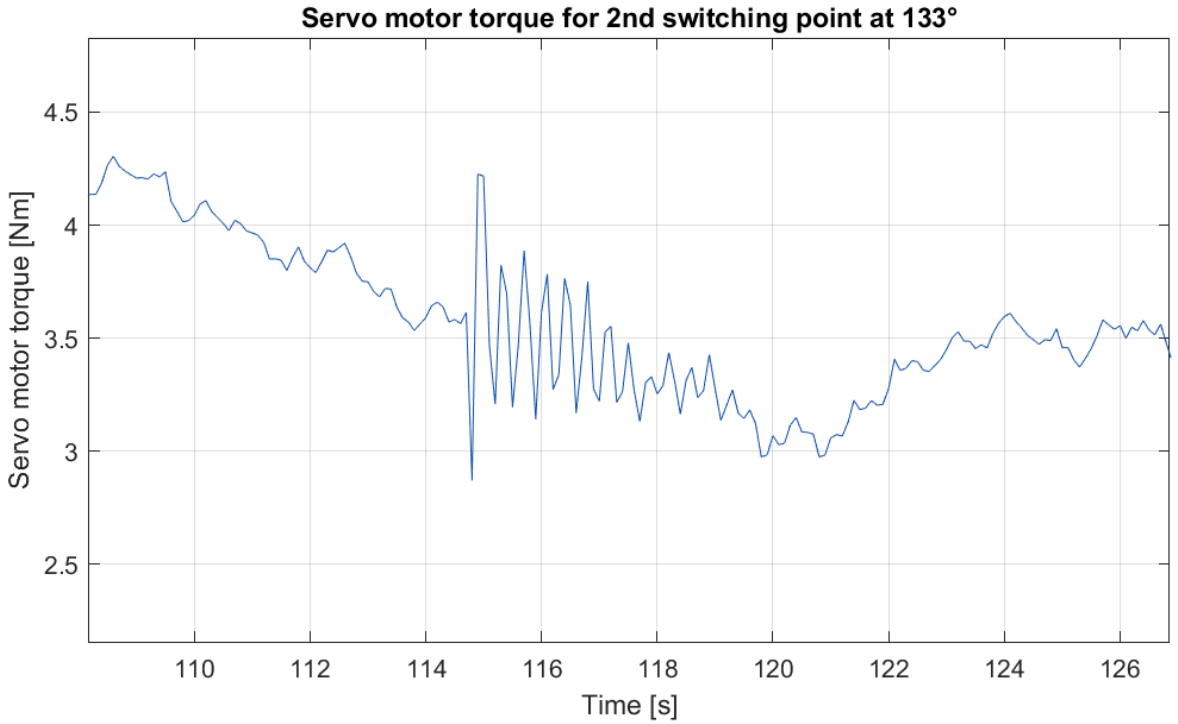

Figure 31 Torque measurement at second switching point

During the downward motion the servo load does not reach zero as derived in Eq. 4.4 since the traverse is moving. For the derivation of the moment balance in Chpt. 4.1.2 the traverse is in hold position instead of moving. For a moving traverse, a dynamic instead of static friction and an additional drive moment which powers the rotation at 20% motor speed is added:

$$M_{cyl} = M_{friction,dyn} + M_g + M_{drive} \quad (4.5)$$

The gravitational moment counteracts the friction and supplements the drive moment during the downward motion. Depending on the magnitude of $M_{g,max}$, the gravitational forces are sufficient to lower the traverse and in that case the servo motor does not need to supply M_{drive}. Additionally, the servo motor also powers the gear pumps. They need to circulate the oil through the hydraulics system to open the cylinder valves. Otherwise the pistons are not able to move and the rotation of the traverse is blocked (cf. Chpt. 3.1.2). The minimum servo motor torque for 20% motor speed is 3.5 Nm.

The maximum gravitational moment occurs at 0° and 180° where the gravitational lever is at a maximum. In order to assess the impact of specific CWs, the servo motor torque is measured for a continuous, upward motion from 0° to 5° with various counterweights and compared to a well-balanced traverse (cf. Figure 32). The servo motor torque during a motion from 85° to 95° is taken as a reference case for a well-balanced traverse since at 90° the lever of the gravitational moment is negligible and therefore this moment is at a minimum. The combined effective piston levers at 0° and 90° are 553 mm and 551 mm, respectively. Their impact on this comparison of the servo torque measurements can therefore be neglected.

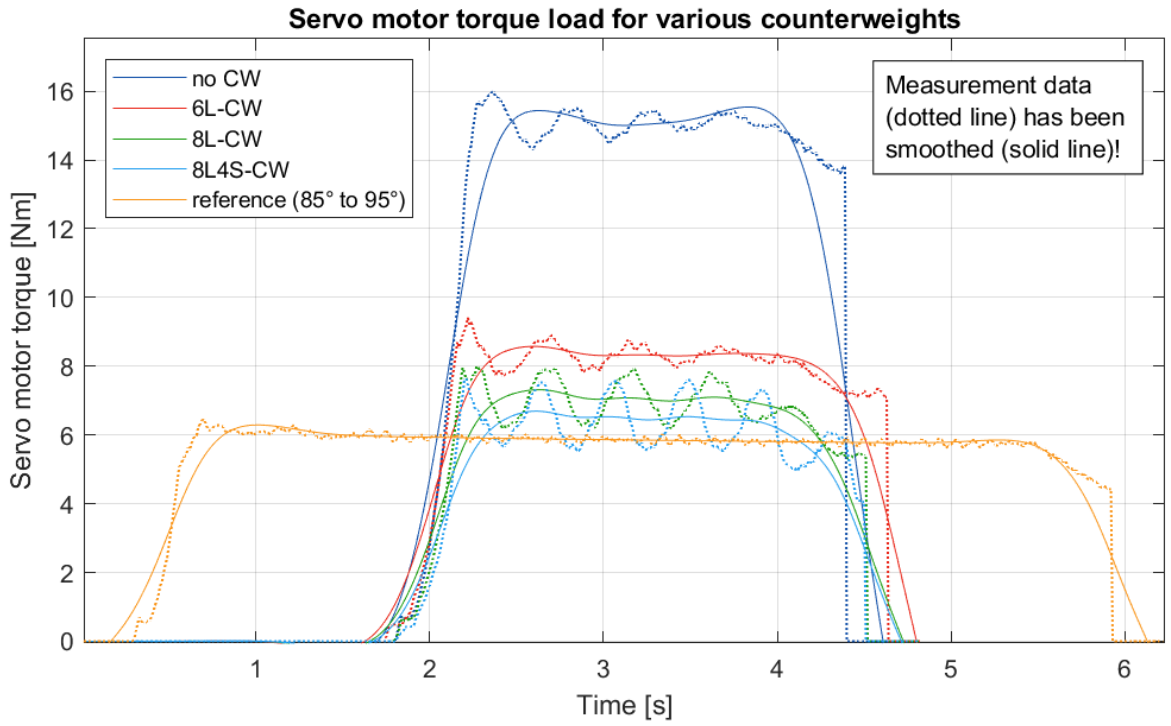

Figure 32 Effect of the counterweight on the servo motor torque

The necessary servo torque decreases with increasing counterweight (cf. Figure 32). For example, the installation of an 8L4S-CW reduces this torque by 56% (compared to a motion without CW) so that it is within 10% of the reference measurement. The reference servo torque is approximately 6 Nm. Because the measurement data displays oscillations, a smoothing spline function[16] was used to determine the average torque. These oscillations are also visible in the traverse motion and are likely to overly strain the test rig structure. Thus, the fully balanced system has not

[16] smoothing parameter 0.95 and unweighted data

been tested since the tendency of oscillations increases with increasing Counterweight (cf. Chpt. 4.2). For the remaining tests in this thesis the 6L-CW was mounted which leads to a 43% load reduction compared to no CW while enabling manageable oscillations.

4.2 Traverse Oscillations

The balancing of the traverse revealed a fault in the KU: Clearances in the four bearings at the interfaces between the hydraulic cylinders, the traverse and the drive pylon. Without the gravitational moment of an unbalanced traverse to tension the bearings, the cylinders can move more easily within the range of the clearances. At the end of a motion, the traverse has an inertial and gravitational momentum which needs to be absorbed by the test rig structure. This causes elastic deformations and results in oscillations. These previously minor, acceptable oscillations are exacerbated by the bearing clearances because they decrease the overall damping capabilities of the test rig. As the bearing tensioning decreases with a more balanced traverse, the oscillation intensity increases. This is apparent in Figure 32 as the oscillating traverse exerts oscillating loads onto the hydraulic cylinders which in turn causes oscillations in the servo motor torque because the hydraulic oil acts as a conduit between the cylinders and the gear pumps.

Increasing the standstill time in between steps to let the traverse settle after each step does not noticeably improve the vibration behavior (cf. Figure 33). The depicted data stems from an experiment with a 6LCW and a step-by-step motion from 40° to 140°. Within that segment of the rotation the most intense traverse oscillations occur as the gravitational moment is minimal. For the range of servo timings considered in this thesis, the kinetic impulses generated by the servo drive and the traverse oscillations do not result in a noticeable constructive interference which would lead to a resonance disaster.

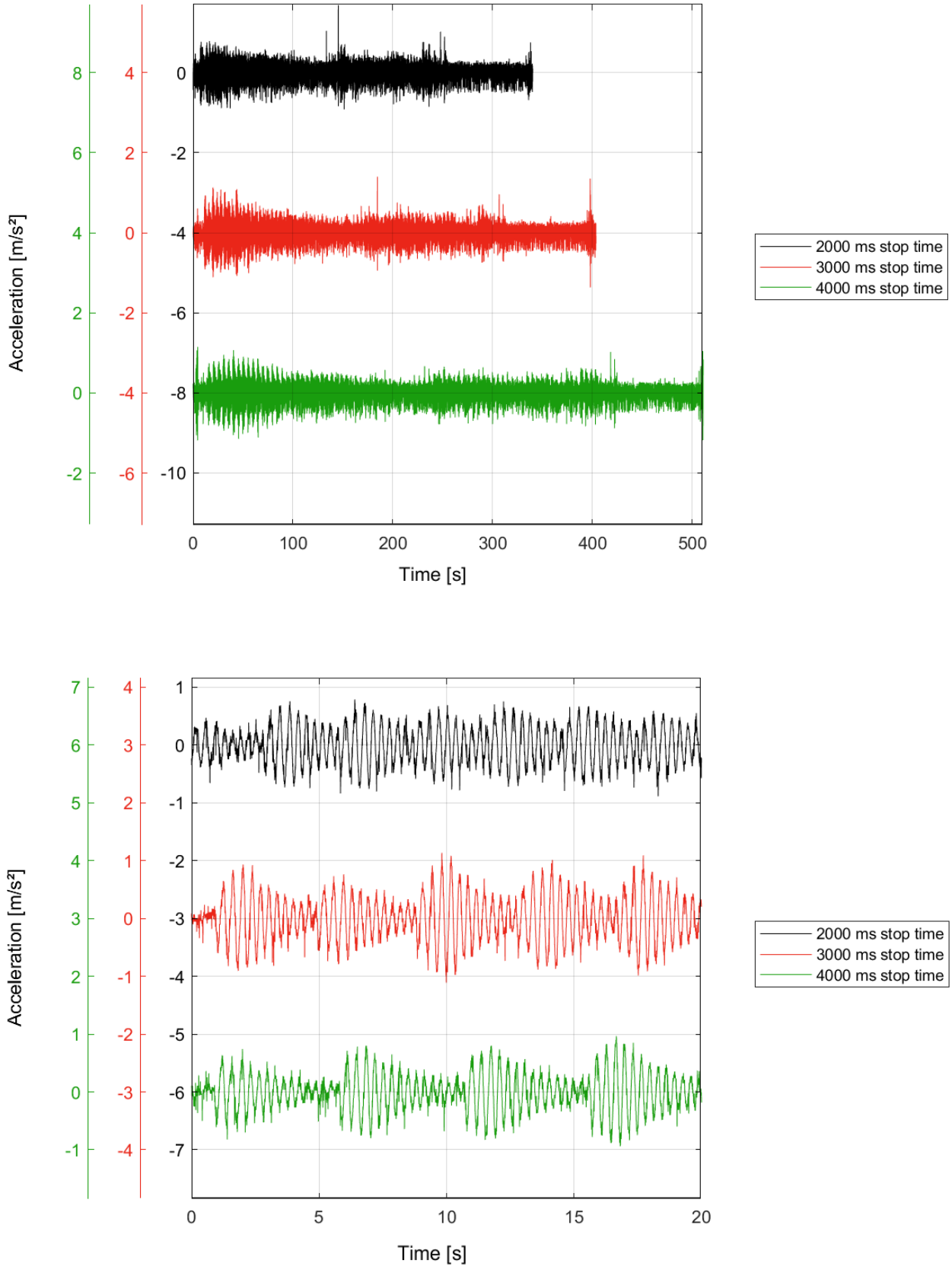

Figure 33 Vibration measurements for critical segment (40°-140°)

The oscillation graphs exhibit minor peaks at around 50° (cf. 40-50 seconds in Figure 33). The intensity of the oscillation is linked to the power of the excitation and the damping capability of the test rig determines the duration of critical oscillations, once excited. The excitation is caused by the inertial and gravitational momentum. During the step-by-step motion the traverse velocity is constant because the step size and servo motor runtime are constant. Thereby, the inertial momentum is constant as well. The gravitational moment can supplement or counteract the inertial moment, depending on whether the traverse moves upwards or downwards. After stopping during the upwards motion, the traverse is accelerated in the opposite direction for the range of the bearing clearances and elastic deformation. It exacerbates the excitation compared to the downward motion during which the inertial and gravitational moment act unidirectionally.

In order to mitigate these oscillations, the PLC control algorithm for the KU has been adapted to gently slow down the traverse around critical points of a rotation cycle. These critical points are at the switching points at 35° and 133°, the setpoint of the rotation and the stow and end positions, because the traverse does not only come to a standstill but changes direction as well.The decreased traverse speed lowers the inertial momentum and thus mitigates the oscillations by reducing the excitation but it is counterproductive towards the objective of minimizing the test cycle time. To improve the test rigs damping capabilties, a new bearing is designed.

4.2.1 New Cylinder Bearings

The hydraulic cylinders of the KU have been found to exhibit extensive clearances. During the switching points the switching cylinder needs its piston to move for the sum of these clearances in order to start rotating the traverse again. This movement has been measured with a feeler gauge which yielded a total bearing clearance of 1 – 1.2 mm for each cylinder. In order to ensure play free bearings, a new bearing system with narrower tolerances has been designed (cf. Figure 34). The bolt is manufactured according to specifications provided by Weber Hydraulik, the hydraulic cylinder manufacturer. Since the inner diameter of the cylinders articulated joint measures 50 mm while the bearing holes of the drive pylon measure 60 mm, radial spacers are necessary. They possess a similar fit with the bolt as the cylinders joint. The exact diameters of the pylon bearing holes are unknown and could not be

accurately measured due to the lack of necessary measurement devices. Therefore the radial spacers are designed with an outer diameter of 60.23 – 60.3 mm. This allows for iterative, miniscule diameter reductions during installation so a tight fit similar to the one at the bolt interface can be achieved.

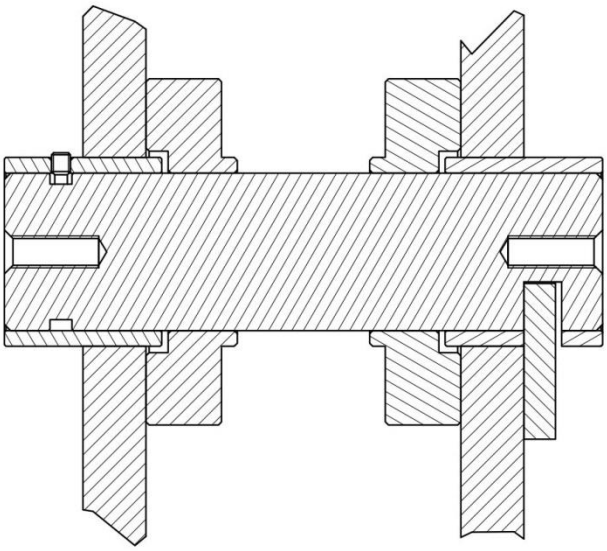

Figure 34 New cylinder bearing design

The articulated joint of the hydraulic cylinder enables it to turn around its centerline. This is necessary to compensate minor alignment mismatches between the two bearings of one cylinder. An axial spacer is designed to keep that joint in place. It is loosely mounted onto the bolt. The cylinders joint also facilitates the rotary movement of the bearing and the bolt therefore needs to be secured against spinning. The spin-lock is realized with a 10 mm thick plate inserted into a groove of the bolt and screwed to the drive pylon plates.

The full specifications of the new design can be found in Appendix D.

4.3 PLC Cycle Optimization

The incremental, rotational movement can be automated within the PLC in two ways: controlled and timed. For the former, the PLC controls the angular position during the traverse motion and stops the servo motor if the step size is within acceptable deviations of the set step size. This method achieves high accuracy in regards to step size only at low speeds. At high speeds, the acceptable deviations need to be increased due to a delay between the traverse reaching a setpoint and stopping. This is caused by the PLC acquisition frequency, communication times (e.g. rotary encoder to PLC or PLC to servo controller) and the deceleration ramp of the servo motor. These are accumulating factors and the latter has the primary negative impact on the accuracy of that mode.

For the timed mode the PLC sets how long the servo motor runs per step and how long the pauses between them are (cf. Figure 35). The minimum servo runtime t_{go} and servo stop time t_{stop}, at which a stable test cycle can be executed, are 800 ms and 1000 ms respectively. Shorter time spans result in unreliable servo motor performance because the acceleration and deceleration ramps can coincide with each other, preventing the traverse from stopping. A PID controller is used to control the step size by manipulating the servo motor speed (cf. Chpt. 4.3.1). This control loop for the current step is executed after the previous step is completed and the entire motion, including deceleration ramp, is considered. Therefore the previously mentioned delays, which adversely affect the control method, are of no concern.

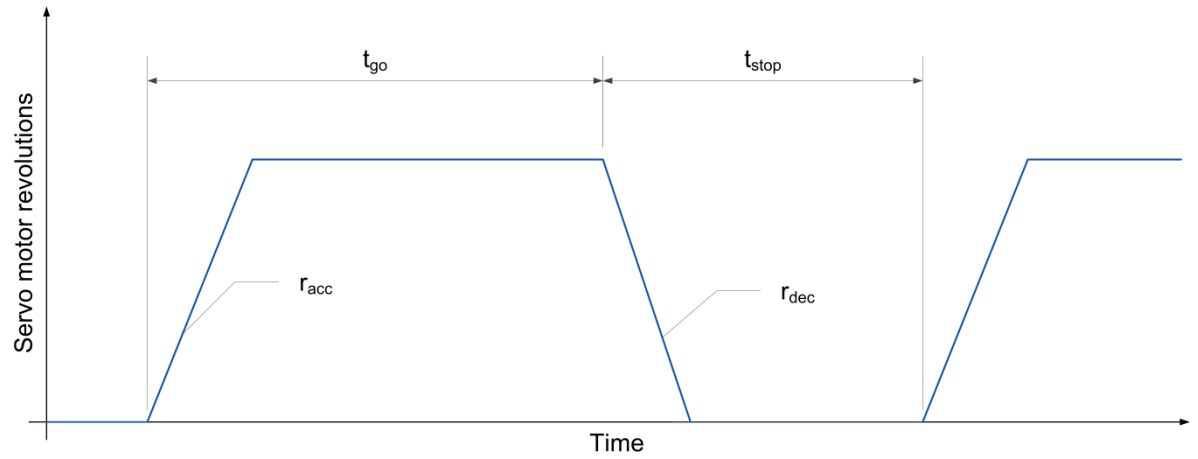

Figure 35 Servo motor motion profile for one step

Since the purpose of the test rig is accelerated life cycle assessment, a fast test cycle is the primary goal. The secondary objective is a reproducible step size because the repeated changing of static and dynamic friction at the swivel joint is suspected to play a major role in REPA wear. The timed method is superior to the control method for both concerns since its timing is at the hardware limit and with the PID controller it results in more precise step sizes at higher speeds and lower step sizes.

4.3.1 Step controller

Without a step controller the timed cycle does not yield reproducible step sizes. The constant servo power and runtime result in a constant combined piston extension/retraction per step[17]. This movement is non-linearly linked to the rotational angle due to the geometrical boundary conditions between the cylinder/traverse interface and the cylinder bearings in the drive pylon. While the bearings of the hydraulic cylinder in the drive pylon are fixed, the locations of the bearings in the cylinder/traverse interface rotate synchronously with the traverse. Only the piston movement tangential to the rotation axis contributes to the rotation (cf. Figure 38). That movement is the sum of the piston extension and the interface rotation. The step size correlates with the tangential motion during the respective step. Since application-oriented step sizes are ≤1° the step size can be calculated as the ratio of the tangential motion[18] and the distance between the bearing and rotation axis:

$$\Delta\varphi_{\mathrm{step}} = \frac{\mathrm{s_{cyl,t}}}{0.35\mathrm{m}} \tag{4.6}$$

For the miniscule step-by-step motion the movements are approximated as lines. This can be correlated to the piston levers and servo runtime (cf. Appendix E):

$$\Delta\varphi_{\mathrm{step}} = \frac{\mathrm{k} * \mathrm{P_{servo}} * \mathrm{t_{go}}}{0.35\mathrm{m}} \left[\sqrt{2 - \left(\frac{\mathrm{l_{eff,east}}}{0.35\mathrm{m}}\right)^2} + \sqrt{2 - \left(\frac{\mathrm{l_{eff,west}}}{0.35\mathrm{m}}\right)^2} \right] \tag{4.7}$$

[17] the extension/retraction of each individual cylinder depends on the geometric boundaries, see Appendix E

[18] For angles ≤1° the tangential motion curve is approximated as a straight line

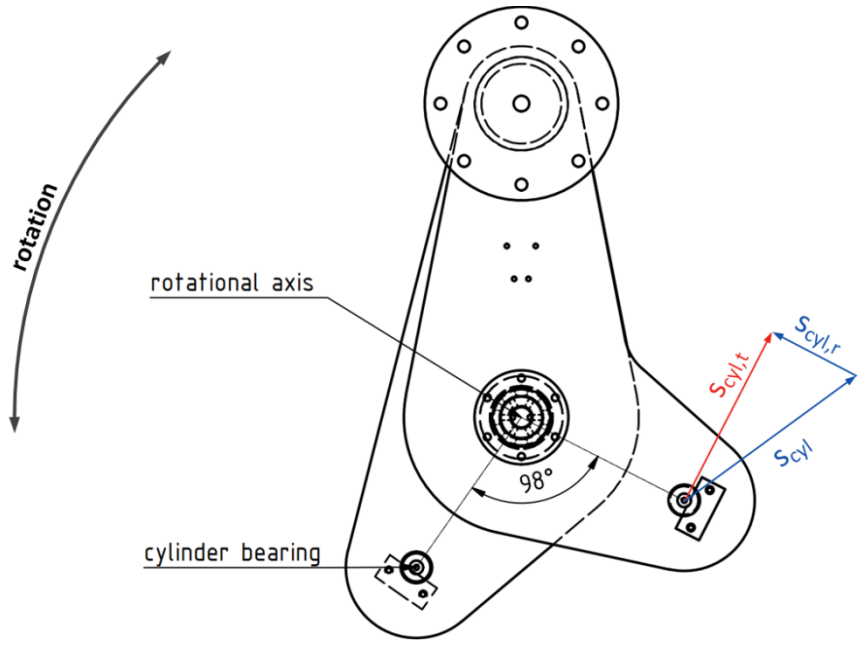

Figure 36 Cylinder motion at cylinder/traverse interface (vertical traverse position)

The factor k accounts for the transmission between the servo motor via the gear pumps to the cylinders and the cylinder geometry. It is an unknown proportional factor to P_{servo}. See Appendix E for the derivation. According to this correlation, the step size is plotted in Figure 37 for a constant servo motor power and runtime over a rotation from -20° to 180°.

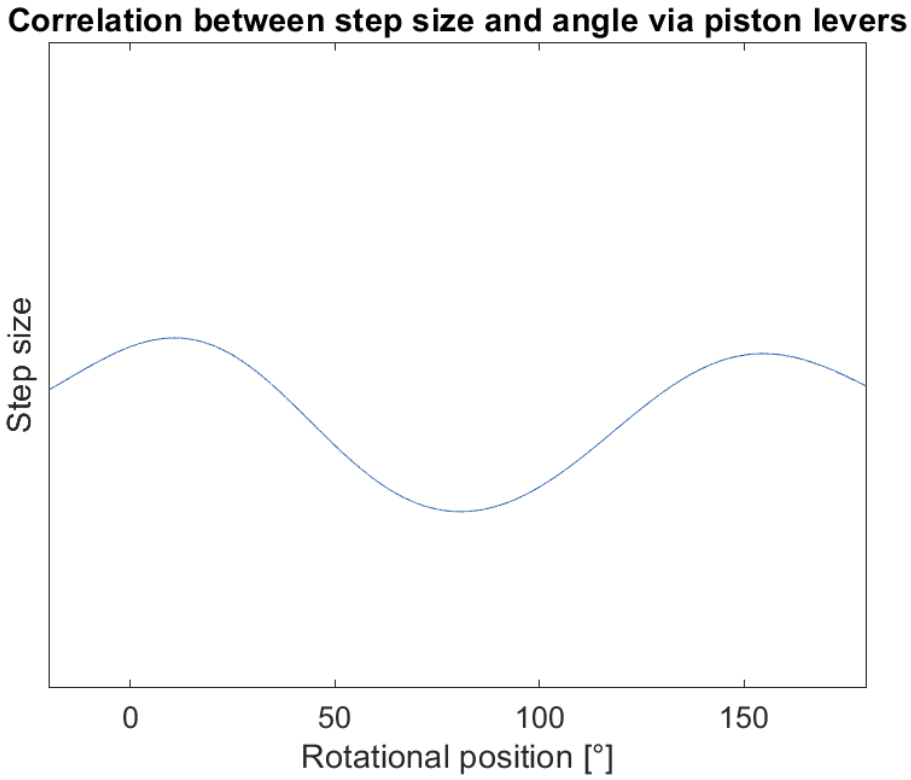

Figure 37 Correlation between step size and piston levers

The step controller mitigates this impact on the step size by varying the servo power, i.e. the total piston extension/contraction, per step. A controller without integral and derivative action is sufficient for this application. Empirical tuning experiments yield a proportional gain factor of K = 5 as suitable. The controller runs one loop at the end of each step. During that loop the size of the just completed step is compared to the set step size. The difference is then multiplied with the proportional gain and set as the servo power (cf. Figure 38).

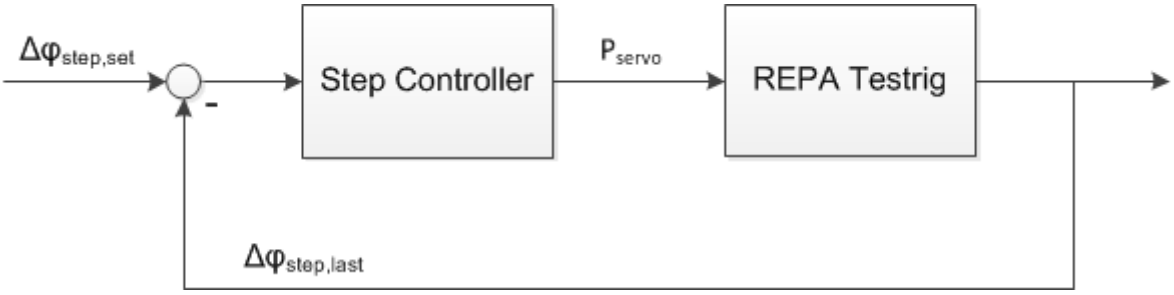

Figure 38 Step controller block diagram

In Figure 39 the effect of the controller is shown. The step sizes without PID control exhibit the angle correlation calculated in Equation 4.7. The controller manages to generate step which are mostly within 10% of the set step size. There are three irregularities in the graph of the controlled cycle (cf.): at the start, at 35° and 133°. The latter two occur because of the cylinder switching points (cf. Chpt. 3.1.2). It is necessary to reduce the servo power in these segments to ensure a safe operation. During these safety sections the controller is deactivated and continues afterwards with the data of the last step before the segment as input. The first irregularity is caused by the start value of the controller. An arbitrary servo power is set for the first step and after it is completed, the first loop of the controller is executed. A few steps are necessary to reach an approximate control output for the necessary servo timing and step size. A greater proportional gain factor can accelerate this but negatively influences the control of the subsequent steps. It is more effective to set an approximate servo motor power for the first step which is based on empirical evidence.

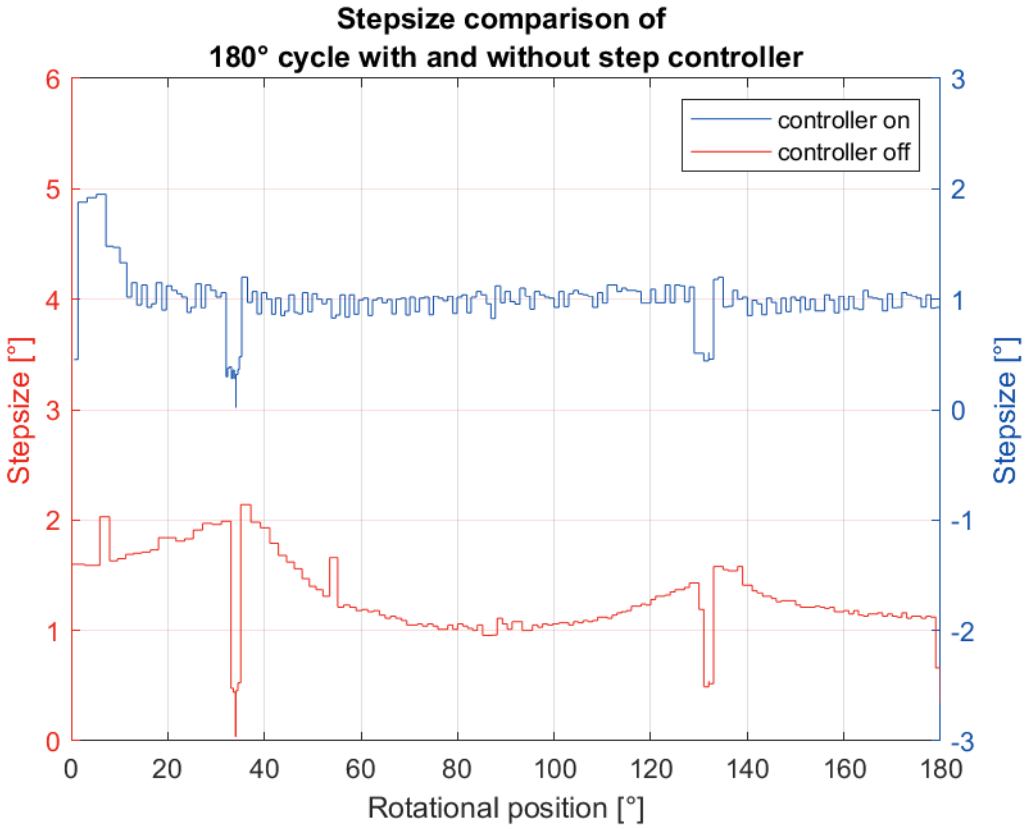

Figure 39 Cycle step sizes with and without step controller

Experiments for various step sizes, servo motor powers and runtimes show a linear correlation between the latter two (cf. Figure 40). The data depicted is taken from nine experiments at 0° rotational position. It is used to determine this correlation:

$$P_{servo} = \begin{cases} -0.0103\, t_{go} + 18.16, & \text{for } \Delta\varphi_{step,\,set} = 0.25° \\ -0.0140\, t_{go} + 24.13, & \text{for } \Delta\varphi_{step,\,set} = 0.50° \\ -0.0238\, t_{go} + 39.60, & \text{for } \Delta\varphi_{step,\,set} = 1.00° \end{cases} \tag{4.8}$$

A three-dimensional correlation incorporating the step sizes can be done in the future. It was not successful with the data set used for the equations above. The models deviation from the experimental data differed by more than 10%, most likely due to an insufficient number of data points. A three-dimensional model is not necessary since the step size is constant for a test program with several thousand test cycles. The smaller amount of data required for a two-dimensional, linear correlation is more easily obtained before a test program commences. Alternatively, the proportionality constant k in Equation 4.7 can be determined and the correlation can be implemented in the control algorithm to find suitable initialization values.

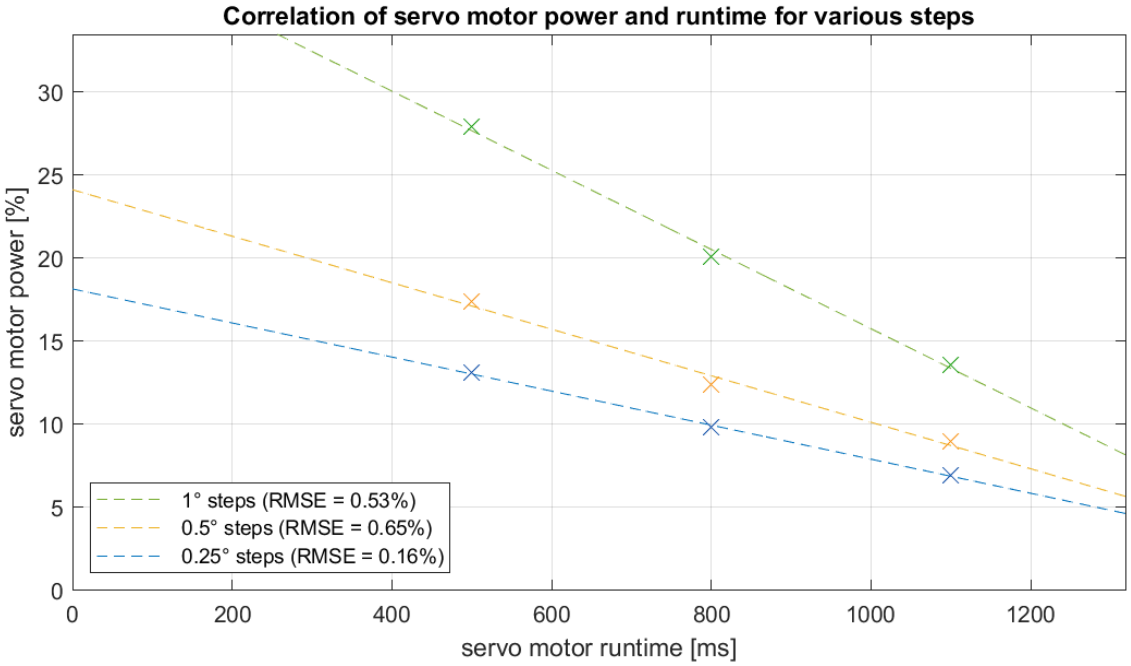

Figure 40 PID start value correlation at 0°

4.3.2 Optimization of servo stop time

It is crucial that the traverse stops in between steps in order to cause the switch between static and dynamic friction at the REPA swivel joint. The servo motor does not stop immediately once it receives the stop signal from the PLC. It slows down according to a set ramp (cf. Chpt. 3.1.2). This has to be considered when determining the actual time the traverse is at a standstill. The minimum servo stop time can then be calculated accordingly:

$$t_{stop} = \begin{cases} \frac{n_{servo}}{r_{dec}} + t_{standstill}, & \text{for } \frac{n_{servo}}{r_{dec}} + t_{standstill} > 500\ ms \\ 500\ ms, & \text{for } \frac{n_{servo}}{r_{dec}} + t_{standstill} \leq 500\ ms \end{cases} \quad (4.9)$$

The servo power is set by the step controller and the standstill time is a cycle parameter. The deceleration ramp can be maximized in order to minimize the stop time and thereby the overall test cycle time. The limits of the ramp are determined by the hardware and the operational safety of the test rig, i.e. by the effect on the oscillations. The ramp can be increased with a PID controller until the servo drive cannot accelerate as fast as specified (cf. Figure 41). It is important that the actual behavior of the motor matches the operation parameters set by the PLC to generate reproducible results. Same as the step controller, the ramp controller executes once

at the end of every step to maintain a trapezoidal motion profile. The input for the control loop is the maximum deviation of the actual motor speed from the ramp during the deceleration of the previous step. If that deviation is within acceptable limits, the ramp can be steadily increased. If the deviation exceeds that limit, the ramp is steadily decreased again until the servo motor deceleration can match the ramp again. Since this controller modifies the ramps which affects the servo speed profile, its output is an input disturbance for the step controller.

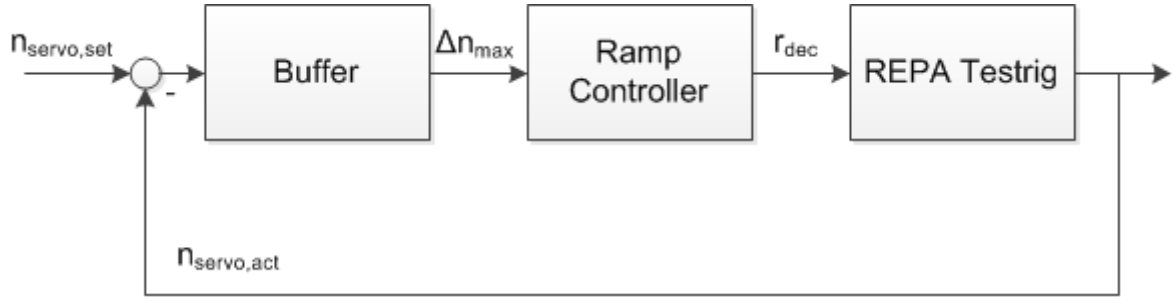

Figure 41 Ramp controller block diagram

This controller has not been implemented and tested because the servo controller is not able to exchange the required data with the PLC. A switch from analog to e.g. Profinet communication would be necessary. A similar controller can be also used for the acceleration ramp in the future to minimize the servo runtime. These ramps can then be maximized in real time up to a safety limit that needs to be determined. In general, an increased ramp can reduce the servo timing but can also be hazardous in regards to the test rig safety.

4.3.3 Velocity controller

At a constant servo motor power, the actual traverse velocity is angle dependent due to the angle dependency of the piston and gravitational moments at the cylinder/traverse interface (cf. Chpt. 4.1.2). Figure 42 show the block diagram of a PI controller which is used to maintain a constant rotation velocity. Empirical studies have shown a proportional gain of 0.12 and an integral action time of 30 ms are suitable for the test cycle.

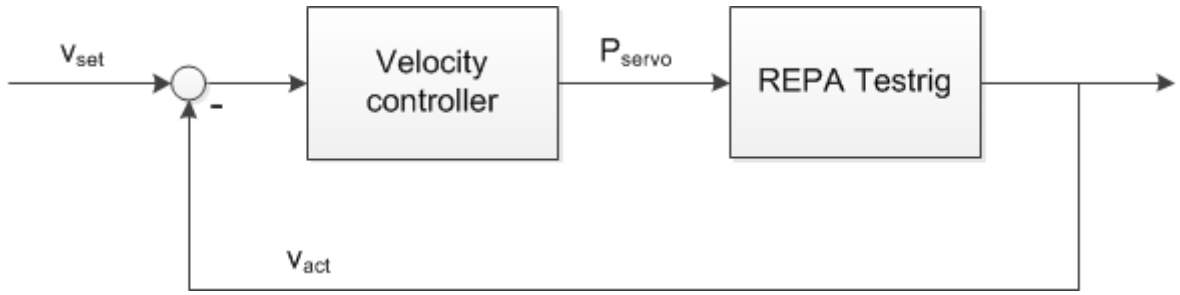

Figure 42 Velocity controller block diagram

A similar controller can be implemented for the translational speed. That is not required for the test cycle proposed in this thesis because the translation occurs during parts of the rotation. The continuous and step-by-step rotations are the determining factors for the overall test time.

5 Summary and Outlook

The life cycle test time is minimized within the mechanical limits of the test rig. One cycle using solely continuous rotation requires 140 seconds to complete. A more realistic daily cycle with a step size of 1°, a stow position of -20° and a tracking phase from 0° to 180° takes less than 9 minutes to complete. This results in an overall life cycle test time of approx. 17 days or 63 days, respectively. The simultaneous translation motions have no bearing on the overall test time.

Two PID controllers are utilized to control the rotational velocity during continuous motion and the step size during step-by-step motion, respectively. A split second timing is used for the servo motor powering the rotation to realize the step-by-step motion: For each step, the servo motor runs at a speed, which is output by the PID step controller, for 800 ms which proved itself to be the lower limit for a stable control. An algorithm uses the motor deceleration ramp to calculate the time between steps in order for the servo motor to completely stop and adds a safety margin. This ensures a standstill of the REPA before the next step begins. An upgrade of the PLC to servo controller communication to e.g. Profinet would enable a two-way communication. The split second timing can then be further optimized e.g. by replacing the stop time calculation with a simple servo controller feedback indicating whether the motor is stopped. After the upgrade, the proposed deceleration ramp controller which minimizes the servo motor stop time can be implemented and tested as well.

At the conclusion of this work the step-by-step motion is limited by mechanical faults which cause the test rig to critically oscillate if not slowed down gently before stopping. A counterweight, which balances out the excentrical masses of the KU, was designed and mounted to reduce the loads on the hydraulics system and the KU drive pylon. These oscillations are intensified by a more balanced KU, which is why the counterweight was only partially mounted. The partial counterweight reduced the load on the hydraulics system by 43% to below the rated load. The powertrain of the KU has been investigated in regards to possible weak points which contribute to these oscillations. The bearings of the hydraulic cylinders, one of those weak points, exhibit noticeable clearances and thus have been re-designed to reduce the play of the KU.

If the oscillations are reduced to an acceptable level, the counterweight can be mounted as-designed and the effect on the servo motor timings and ramps reexamined. But as long as the oscillations persist, a step-by-step motion is unfeasible. A slow, safe operation of the step-by-step motion for 10.000 cycles is possible but results in an impracticable overall test time. The test rig can safely subject the REPA to representative temperatures, pressures and mass flows, while rotating the traverse continuously back and forth over a range of 205° and using the translation to simulate the thermal expansion. Such a test is scheduled to begin in June 2019. In order to run a life cycle test including step-by-step motion in a reasonable time, further work needs to be done to reduce the oscillations to a safe level.

List of Figures

List of Tables

List of References

[1] "European Commission," [Online]. Available: https://ec.europa.eu/clima/policies/international/negotiations/paris_en. [Accessed 17 08 2018].

[2] C. Richter, D. Lincot und C. A. Gueymard, Solar Energy, Springer Science+Business Media New York, 2013.

[3] "Solar resource maps," Solargis, [Online]. Available: https://solargis.com/maps-and-gis-data/download/world/. [Accessed 21 08 2018].

[4] G. Knies, „Red Paper - An overview of the Desertec concept," Desertec Foundation.

[5] "PV Panels," Apricus, [Online]. Available: http://www.apricus.com/solar-pv-systems-pv-panels-19.html. [Accessed 21 08 2018].

[6] Fraunhofer Institute for Solar Energy Systems ISE, „New world record for solar cell efficiency at 46% – French-German cooperation confirms competitive advantage of European photovoltaic industry," *Press release,* 1 12 2014.

[7] D. Meneses-Rodriguez, P. P. Horley, J. Gonzalez-Hernandez, Y. V. Vorobiev und P. N. Gorley, „Photovoltaic solar cells performance at elevated temperatures," *Solar Energy,* Nr. 78, pp. 243-250, 2005.

[8] J. Pye, G. Hughes, E. Abbasi, C.-A. Asselineau, G. Burgess, J. Coventry, W. Logie, F. Venn und J. Zapata, „Development of a higher-efficiency tubular cavity receiver for direct steam generation," in *SolarPACES*, Cape Town, 2015.

[9] International Energy Agency, „Technology Roadmap - Solar Thermal Electricity (2014 edition)," Paris, 2014.

[10] R. Pitz-Paal, Lecture Notes: Solartechnik, Institute of Solar Research at RWTH Aachen University, 2018.

[11] E. Bellevrat and K. West, "Commentary: Clean and efficient heat for industry," International Energy Agency, 2018.

[12] A. Fernández-García, M. Cantos-Soto, M. Röger und C. Wieckert, „Durability of solar reflector materials for secondary concentrators used in CSP systems," *Solar Energy Materials and Solar Cells,* Nr. 130, pp. 51-63, 2014.

[13] D. Laing, "Dish-Stirling-Systeme - Eine Technologie tur dezentralen

Stromerzeugung," in *FVS Themen 2002*, 2002.

[14] T. Mancini and P. Heller, "Dish-Stirling Systems: An Overview of Development and Status," *Journal of Solar Energy Engineering,* vol. 125, pp. 135-151, 2003.

[15] A. Farr and R. Gee, "The SkyTrough™ Parabolic Trough Solar Collector," in *ASME 3rd International Conference of Energy Sustainability*, San Francisco, 2009.

[16] R. Buehler, S. Yang and J. C. Ordonez, "Heat Transfer Fluids for Parabolic Trough Solar Collectors – A Comparative Study," in *IEEE Conference on Technologies for Sustainability (SusTech)*, 2016.

[17] R. Pitz-Paal, „Parabolic Trough, Linear Fresnel, Power Tower - A Technology Comparison," in *Institute for Advanced Sustainability Studies e.V.*.

[18] H. Benoit, L. Spreafico, D. Gauthier and G. Flamant, "Review of heat transfer fluids in tube-receivers used in concentrating solar thermal systems: Properties and heat transfer coefficients," *Renewable and Sustainable Energy Reviews,* no. 55, pp. 298-315, 2016.

[19] A. Plumpe, "Design of a Test Rig and its Testing Methods for Rotation and Expansion Performing Assemblies in Parabolic Trough Collector Power Plants," *Master Thesis,* April 2016.

[20] T. Müller, "Commissioning and validation of the underlying model of a test rig analyzing rotation and expansion performing assemblies in parabolic trough collector power plants," *Master Thesis,* January 2017.

[21] P. Heller, The Performance of Concentrated Solar Power (CSP) Systems, Woodhead Publishing, 2017.

[22] B. Hoffschmidt, Lecture Notes: Solar Components, Institute of Solar Research at RWTH Aachen University, 2014.

[23] Senior Flexonics, "TUBOFLEX Datasheet," 2017.

[24] C. Richter und D. Martinez, „Plataforma Solar de Almeria - A German-Spanish cooperative venture," *DLR Nachrichten 109,* Januar 2005.

[25] T. Hilbel, "Design of the motion control for a test rig analyzing rotation and expansion performing assemblies in parabolic trough collector power plant applications," *Bachelor Thesis,* December 2016.

[26] L. Petrov, "Solar Tracking Strategies," *Bachelor Thesis,* January 2011.

[27] ME-Messsysteme, "Strain gauge basics," [Online]. Available: https://www.me-systeme.de/en/support/basics/strain-gauge-basics. [Accessed August 2018].

[28] C. Schütt, "Presentation, evaluation and validation of measurement results from operation tests of rotation and expansion performing assemblies during the commissioning of the REPA Test Rig," *Master Thesis,* April 2018.

[29] IDS Innomic GmbH, "User Guide Piezoelectric Accelerometers," 2008. [Online]. Available: https://www.innomic.com/en/service/training/training_materials/user_guide_piezoelectric_accelerometers.html. [Accessed August 2018].

[30] IDS Innomic GmbH, "KS943B.100 Datasheet," 2016.

[31] LTI Motion GmbH, "LSN-127 Datasheet," 2015.

[32] K. Vignarooban, X. Xu, A. Arvay, K. Hsu und A. Kannan, „Heat transfer fluids for concentrating solar power systems – A review," *Applied Energy,* Nr. 146, pp. 383-396, 2015.

[33] F. Ortiz Vives and M. Meyer-Grünefeld, "Flexible hose system - ROTATIONFLEX connection to HCE of parabolic collectors," in *SolarPACES*, Berlin, 2009.

Appendix A – Hydraulic Circuit Diagram

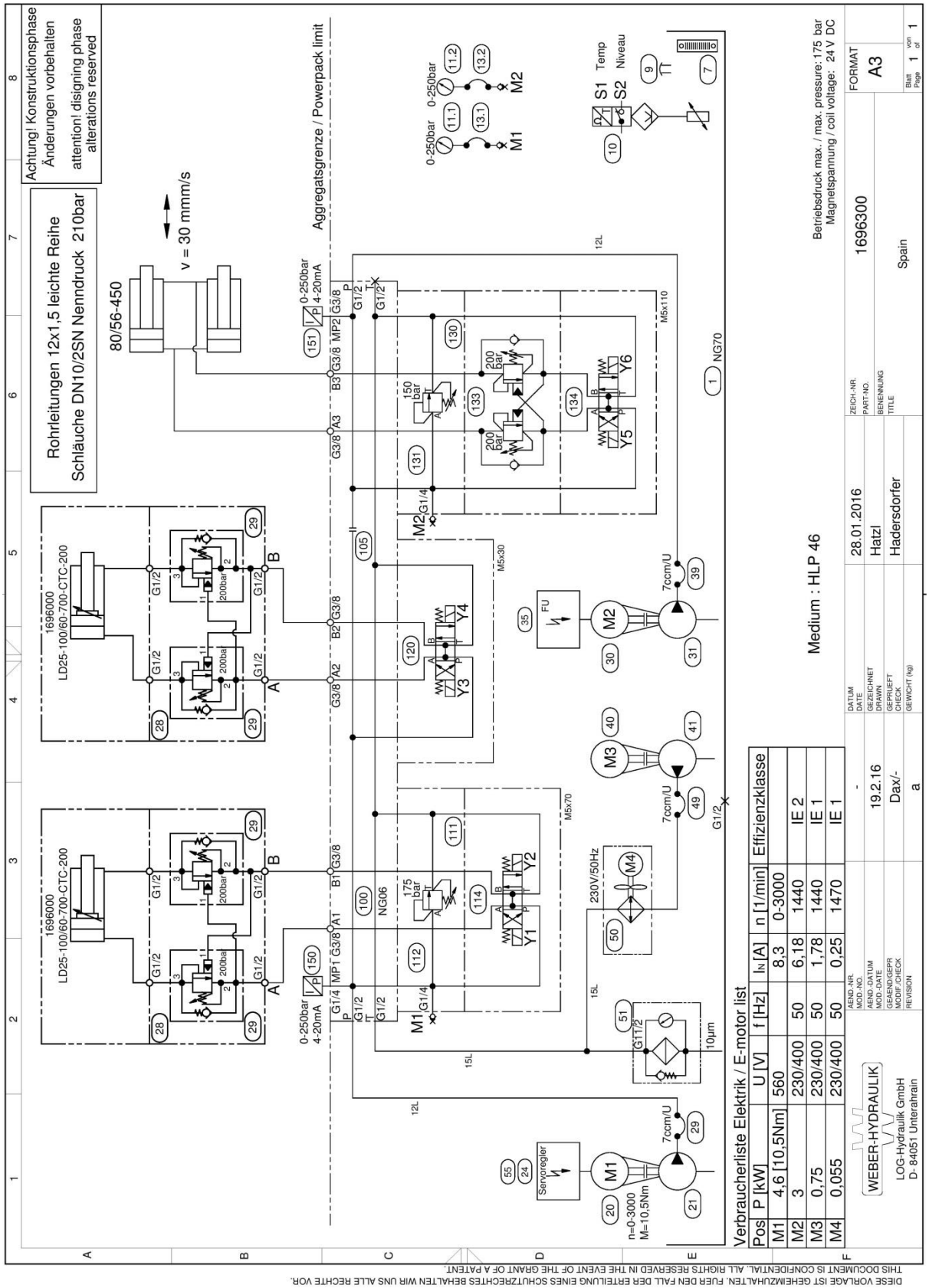

Appendix B.1 – Dynamometer Data Sheet

ME-Meßsysteme GmbH
Neuendorfstr. 18a
DE-16761 Hennigsdorf

Tel +49 (0)3302 8982 4 60
Fax +49 (0)3302 8982 4 69

Mail info@me-systeme.de
Web www.me-systeme.de

K6D175 10kN/1kNm, 20kN/2kNm, 50kN/5kNm

Description

The K6D175 multi-axis sensor is designed for measuring force and torque in three mutually perpendicular axes.
The measurement ranges for the forces and moments can be factory adapted in a wide range. The K6D175 was developed for the following applications:

- Robotics
- Measurements in automation technology.

The force and torque loadings are evaluated e.g. using GSV-8DS SubD44HD or GSV-8AS measurement amplifier. The 6 load values can be calculated using a Windows DLL or using LabVIEW with the aid of a digital calibration document provided.
The calibration document contains the individual calibration factors and error corrections for the sensor.

ME-Meßsysteme GmbH
Neuendorfstr. 18a
DE-16761 Hennigsdorf

Tel +49 (0)3302 8982 4 60
Fax +49 (0)3302 8982 4 69

Mail info@me-systeme.de
Web www.me-systeme.de

Dimensions

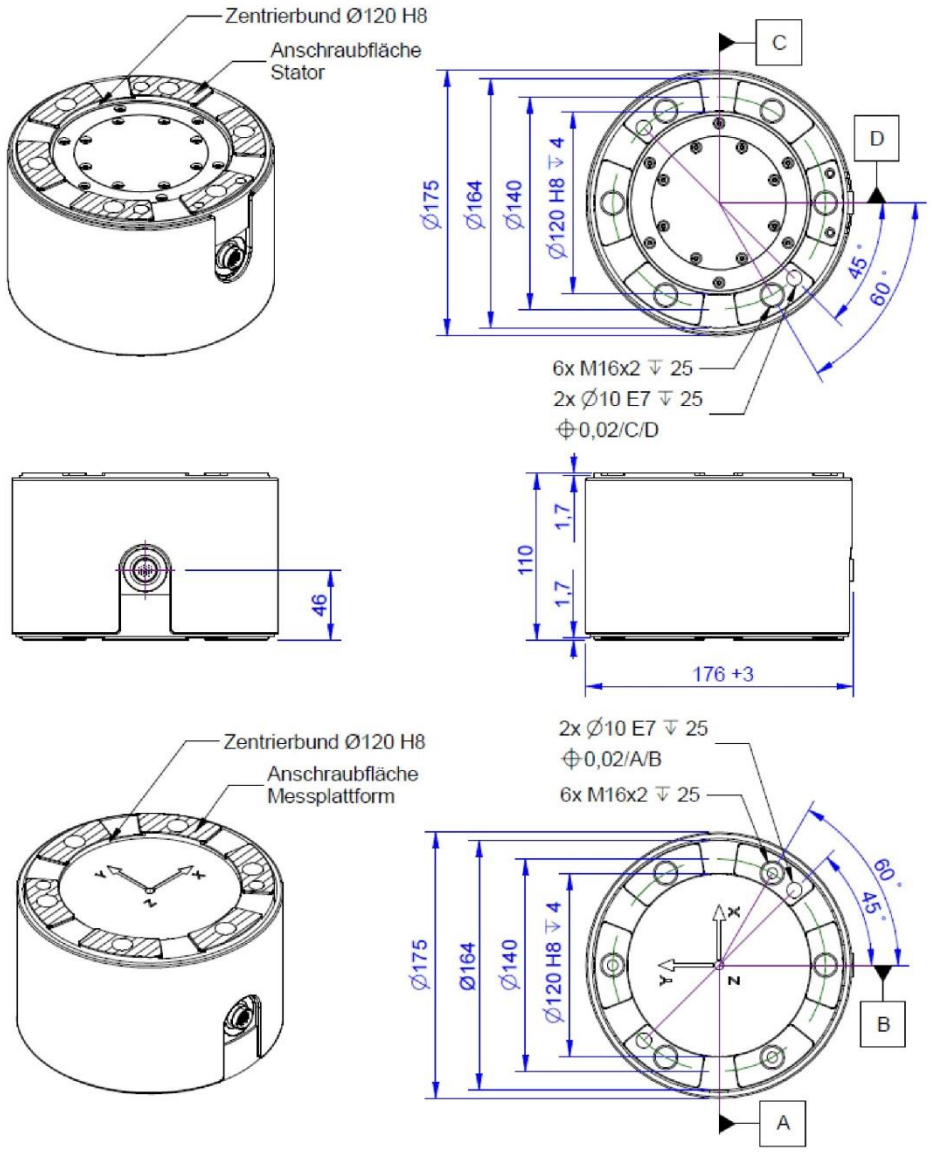

ME-Meßsysteme GmbH
Neuendorfstr. 18a
DE-16761 Hennigsdorf

Tel +49 (0)3302 8982 4 60
Fax +49 (0)3302 8982 4 69

Mail info@me-systeme.de
Web www.me-systeme.de

Technical Data

Force sensor		
Type	6-Axis force sensor	
Force direction	Tension / Compression	
Force introduction	Inner thread	
Dimension 1	6x M16x2	
Sensor Fastening	Inner thread	
Dimension 2	6x M16x2	
Operating force	200	%FS
Rated displacement	0.1	mm
Twist	0.01	rad
Material	Stainless steel	
Dimensions	Ø175 x 110	mm
Height	110	mm
Length or Diameter	175	mm
Torque limit	300	%FS
Bending moment limit	300	%FS

Electrical Data		
Input resistance	350	Ohm
Tolerance input resistance	10	Ohm
Output resistance	350	Ohm
Tolerance output resistance	10	Ohm
Insulation resistance	2	GOhm
Rated range of excitation voltage f	2.5 ... 5	V
Operating range of excitation voltage f	1 ... 10	V
Zero signal to	-0.05	mV/V
Zero signal from	0.05	mV/V

Precision		
Accuracy class	0,5%	
Relative linearity error	0.1	%FS
Relative zero signal hysteresis	0.1	%FS
Temperature effect on zero signal	0.1	%FS/K
Temperature effect on characteristic value	0.05	%RD/K
Relative creep	0.1	%FS
Relative repeatability error	0.5	%FS

Connection Data	
Connection type	Connector
Name of the connection	M16 Rundsteckverbinder oder 26-24 PUR / 24x0,16 mm²

Temperature		
Rated temperature range f	-10 ... 70	°C
Operating temperature range f	-10 ... 85	°C

ME-Meßsysteme GmbH
Neuendorfstr. 18a
DE-16761 Hennigsdorf

Tel +49 (0)3302 8982 4 60
Fax +49 (0)3302 8982 4 69

Mail info@me-systeme.de
Web www.me-systeme.de

Storage temperature range f	-10 ... 85	°C
Environmental protection	IP65	

Abbreviation : RD: „Reading"; FS: „Full Scale";

The application of a calibration matrix is required for the determination of the forces Fx, Fy, Fz and moments Mx, My, and Mz from the 6 measurement channels, and to compensate for the crosstalk.
The calibration data are individually determined and documented for the sensor.
The measurement error is expressed individually by the specification of the extended measurement uncertainty (k = 2) for the forces Fx, Fy, Fz, and moments Mx, My, Mz.

ME-Meßsysteme GmbH
Neuendorfstr. 18a
DE-16761 Hennigsdorf

Tel +49 (0)3302 8982 4 60
Fax +49 (0)3302 8982 4 69

Mail info@me-systeme.de
Web www.me-systeme.de

Pin Configuration

Channel	Symbol	Description	Wire colour	PIN
1	+Us	positive bridge supply	white	1
	-Us	negative bridge supply	brown	2
	+Ud	positive bridge output	green	3
	-Ud	negative bridge output	yellow	4
2	+Us	positive bridge supply	gray	5
	-Us	negative bridge supply	pink	6
	+Ud	positive bridge output	blue	7
	-Ud	negative bridge output	red	8
3	+Us	positive bridge supply	black	9
	-Us	negative bridge supply	purple	10
	+Ud	positive bridge output	gray-pink	11
	-Ud	negative bridge output	red-blue	12
4	+Us	positive bridge supply	white-green	13
	-Us	negative bridge supply	brown-green	14
	+Ud	positive bridge output	white-yellow	15
	-Ud	negative bridge output	yellow-brown	16
5	+Us	positive bridge supply	white-gray	17
	-Us	negative bridge supply	gray-brown	18
	+Ud	positive bridge output	white-pink	19
	-Ud	negative bridge output	pink-brown	20
6	+Us	positive bridge supply	white-blue	21
	-Us	negative bridge supply	brown-blue	22
	+Ud	positive bridge output	white-red	23
	-Ud	negative bridge output	brown-red	24

Shield: connected with sensor housing;

ME-Meßsysteme GmbH
Neuendorfstr. 18a
DE-16761 Hennigsdorf

Tel +49 (0)3302 8982 4 60
Fax +49 (0)3302 8982 4 69

Mail info@me-systeme.de
Web www.me-systeme.de

Manual

Stiffness Matrix K6D175 10kN/1kNm

178.1 kN/mm	0,0	0,0	0,0	10331 kN	0,0	u_x
0,0	178.1 kN/mm	0,0	-103314 kN	0,0	0,0	u_y
0,0	0,0	786.7 kN/mm	0,0	0,0	0,0	u_z
0,0	-10331 kN	0,0	2149.7 kNm	0,0	0,0	phi_x
10331 kN	0,0	0,0	0,0	2149.7 kNm	0,0	phi_y
0,0	0,0	0,0	0,0	0,0	1404.3 kNm	phi_z

Stiffness Matrix K6D175 20kN/2kNm

375.5 kN/mm	0,0	0,0	0,0	21800 kN	0,0	u_x
0,0	375.5 kN/mm	0,0	-21800 kN	0,0	0,0	u_y
0,0	0,0	1658.3 kN/mm	0,0	0,0	0,0	u_z
0,0	-21800 kN	0,0	4531.7 kNm	0,0	0,0	phi_x
21800 kN	0,0	0,0	0,0	4531.7 kNm	0,0	phi_y
0,0	0,0	0,0	0,0	0,0	4844.0 kNm	phi_z

Stiffness Matrix K6D175 50kN/5kNm

614.4 kN/mm	0,0	0,0	0,0	35600 kN	0,0	u_x
0,0	614.4 kN/mm	0,0	-35600 kN	0,0	0,0	u_y
0,0	0,0	2713.6 kN/mm	0,0	0,0	0,0	u_z
0,0	-35600 kN	0,0	7415.4 kNm	0,0	0,0	phi_x
35600 kN	0,0	0,0	0,0	7415.4 kNm	0,0	phi_y
0,0	0,0	0,0	0,0	0,0	4844.0 kNm	phi_z

Element	Description
[kN/mm]	force- displacement
[kNm]	torque- twist
[kN]	force- twist and torque- displacement

ME-Meßsysteme GmbH
Neuendorfstr. 18a
DE-16761 Hennigsdorf

Tel +49 (0)3302 8982 4 60
Fax +49 (0)3302 8982 4 69

Mail info@me-systeme.de
Web www.me-systeme.de

Mounting

The force is applied to an annulus/to 6 segments of a circle, 155 mm – 140 mm in diameter, on the end faces of the sensor. No force is applied to the area inside the 140 mm in diameter ring.

The areas outside the annuli can be used for centring purposes. A centring hole is provided to secure the angular position.

Appendix B.2 – Vibration Sensor Data Sheet

KS943B.100

Triaxiale Beschleunigungsaufnehmer IEPE
Triaxial Accelerometers IEPE

Überblick

- Zentral-Durchgangsbohrung zur einfachen Befestigung und Achsenjustierung
- Kleine Abmessungen
- Miniatur-M5-Steckverbindung
- IEPE-Ausgang: Geringe Störempfindlichkeit in rauer Umgebung; große Kabellängen möglich

Overview

- Central drilling for easy mounting and axis alignment
- Small dimensions
- Miniature M5 connector
- IEPE output guarantees low EMI under rough environmental conditions and allows long cables

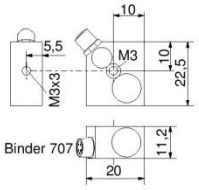

Modell • Model		KS943B.100
Piezoelement und integrierter Verstärker • Piezo element and integrated charge converter		
Spannungsausgang • Voltage output		IEPE (Integrated Electronics Piezo Electric)
Piezosystem • Piezo system		Scherprinzip • Shear design
Spannungsübertragungsfaktor • Voltage sensitivity	B_{ua}	100 mV/g ±5%
Messbereich • Range	a_+/a_-	±60 g
Bruchbeschleunigung • Destruction limit	a_{max}	8000 g
Eigenrauschen (Effektivwert) • Residual noise (RMS) Rauschdichten • Noise densities	$a_{n\ wide\ band}$ a_n	< 600 µg @ 0.5 .. 20000 Hz 50 µg/√Hz @ 0.1 Hz 30 µg/√Hz @ 1 Hz 10 µg/√Hz @ 10 Hz 1 µg/√Hz @ 100 Hz
Speisestrom • Supply current	I_{Const}	2 .. 20 mA
Arbeitspunktspannung • Output bias voltage	U_{Bias}	12 .. 14 V
Resonanzfrequenz Z-Achse • Resonant frequency z-axis	f_r	> 32 kHz (+25 dB)
Linearer Frequenzbereich • Linear frequency range	f_L	0.5 .. 22 000 Hz (±3 dB)
Querrichtungsfaktor • Transverse sensitivity	Γ_{90max}	< 5 %
Ausgangsimpedanz • Output impedance	r_{OUT}	< 150 Ω
Temperaturdaten • Temperature data		
Arbeitstemperatur • Operating temperature	T_{min}/T_{max}	-20 / 120 °C • -4 / 248 °F
Temperaturkoeffizient von B_{ua} • Temperature coefficient of B_{ua}	$TK(B_{ua})$	-0.08 %/K @ T < 80 °C -0.11 %/K @ T > 80 °C
Temp.sprungempfindlichkeit • Temp.transient sensitivity	B_{aT}	0.0015 g/K
Mechanische Daten • Mechanical data		
Masse ohne Kabel • Weight without cable	m	16 gr. • 0.6 oz
Gehäusematerial • Case material		Aluminium
Kabelanschluss • Cable connection		radial
Buchse • Connector		Binder 707
Befestigung • Mounting		M3 (Y), M3 (Z)

IDS Innomic Gesellschaft für Computer- und Messtechnik mbH

Typischer Frequenzgang • Typical Amplitude Response

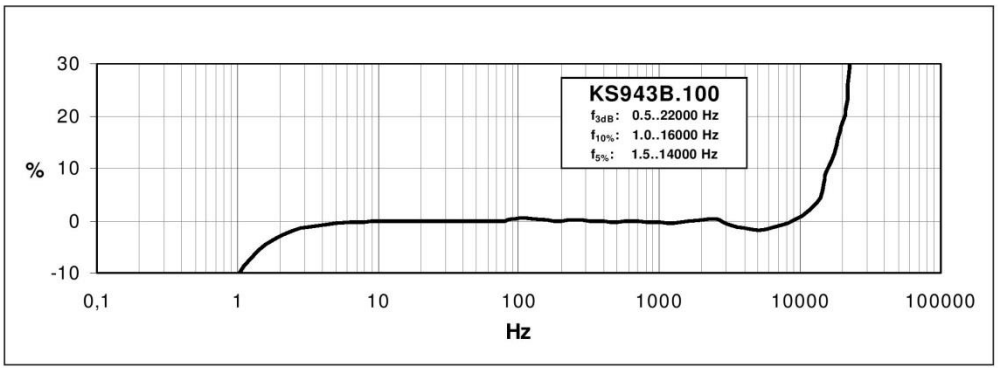

Temperaturverhalten • Temperature characteristics

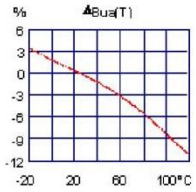

Rauschverhalten • Noise characteristics

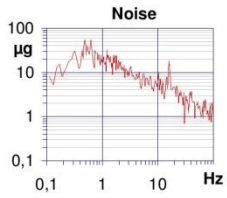

Blick auf Steckerstifte • View at pins

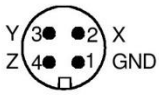

Bestellinformationen

KS943.100: Standard
- Sensor
- Dokumente: Kennblatt

Der KS943B.100 kann direkt an die PC-Messtechnik des *VibroMatrix®*-Systems angeschlossen werden.

Ordering information

KS943.100: Standard
- Sensor
- Documents: individual characteristics

The KS943B.100 can be directly connected to the measuring instrumentation of the PC-based *VibroMatrix®*-system.

Änderungen vorbehalten.
Specifications subject to change without prior notice.

Februar 2016 • February 2016

D e u t s c h l a n d

IDS Innomic
Gesellschaft für Computer- und Messtechnik mbH
Zum Buchhorst 35
29410 Salzwedel

(03901) 305 99 50
(03901) 305 99 51
info@innomic.de
www.innomic.de

I n t e r n a t i o n a l

IDS Innomic GmbH
Zum Buchhorst 35
D-29410 Salzwedel
Germany

+49 (3901) 305 99 50
+49 (3901) 305 99 51
info@innomic.de
www.innomic.com/en

Appendix C.1 – Counterweight Specifications

Lever Plate

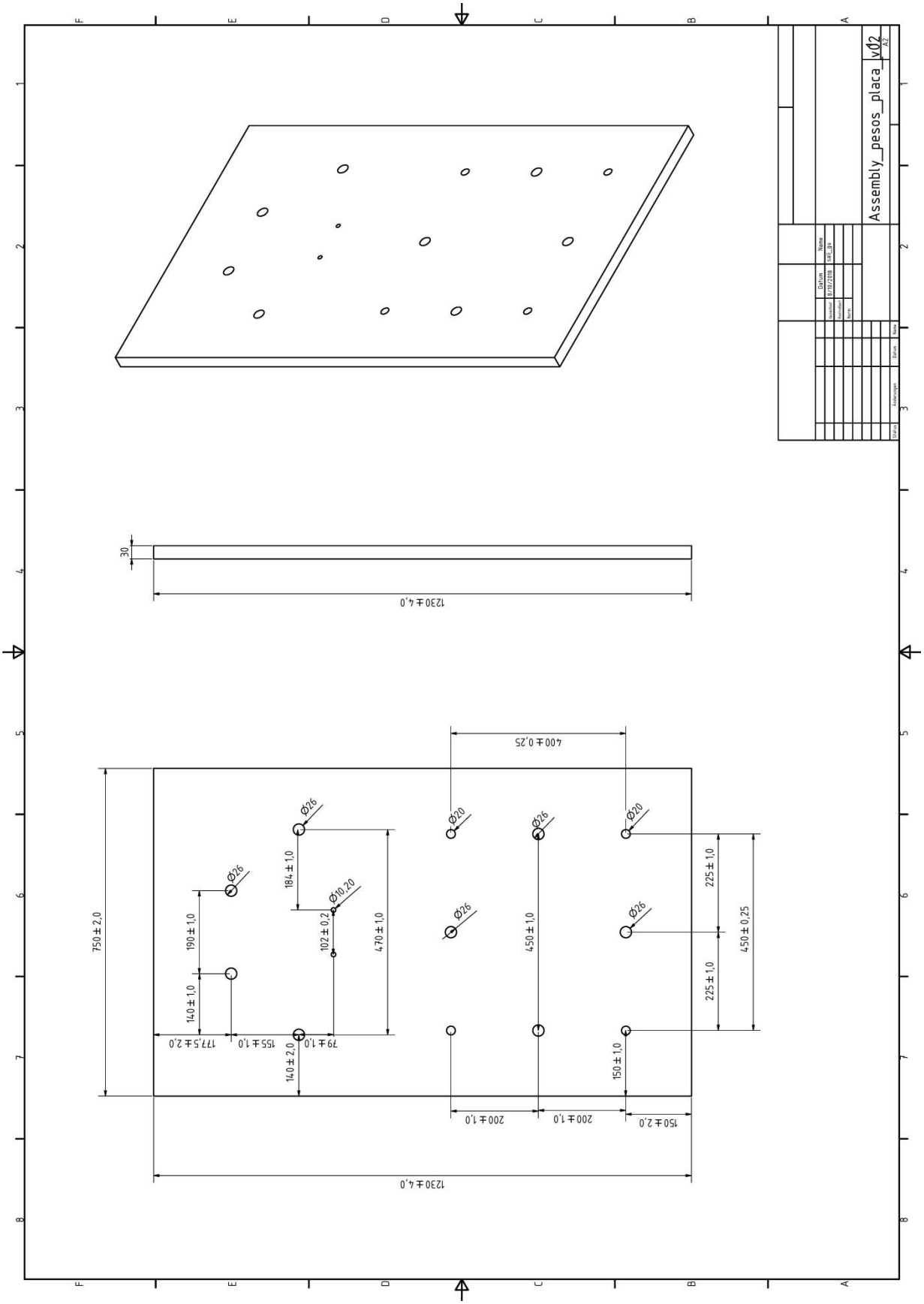

10 mm Weight Plate

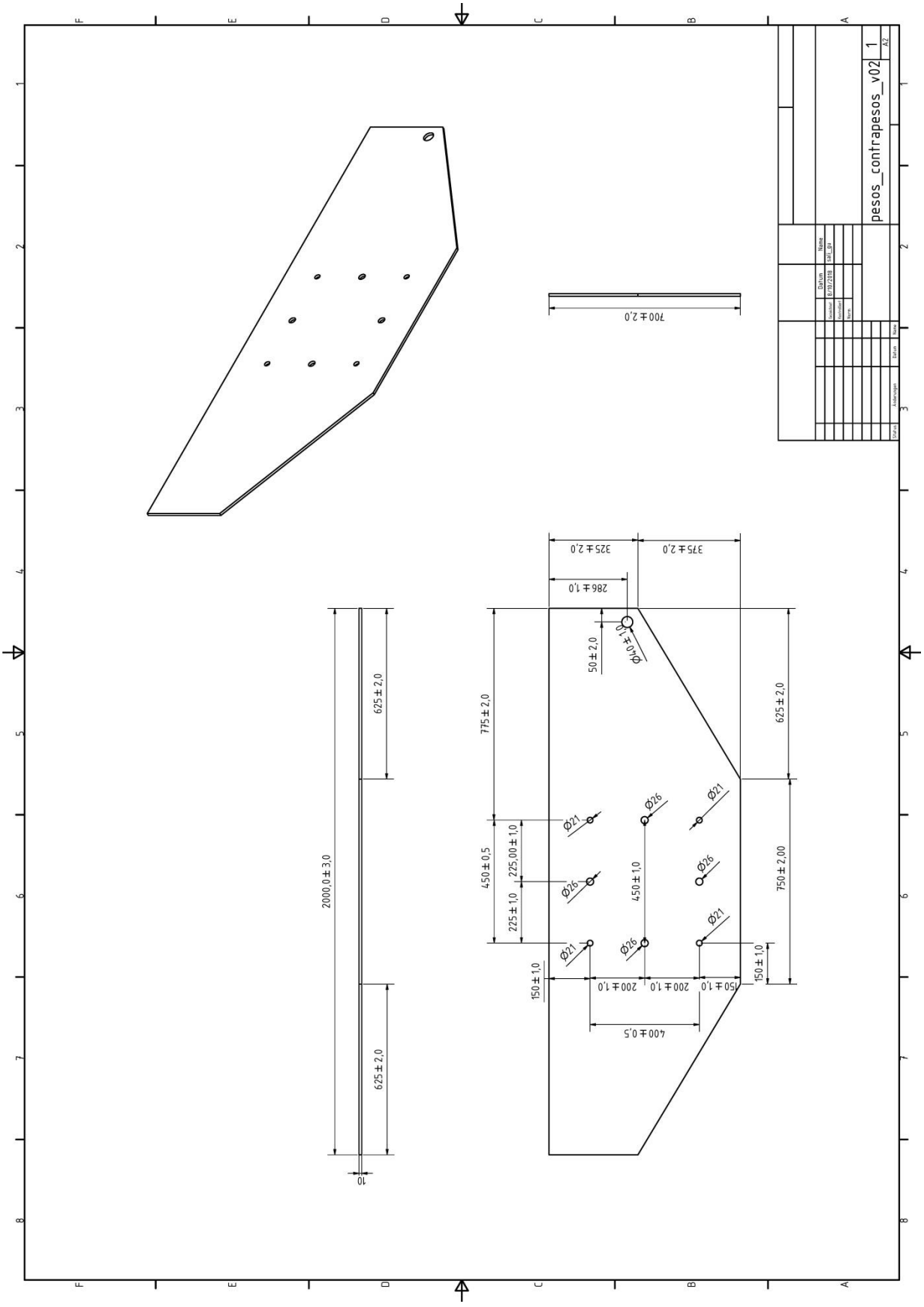

20 mm Weight Plate

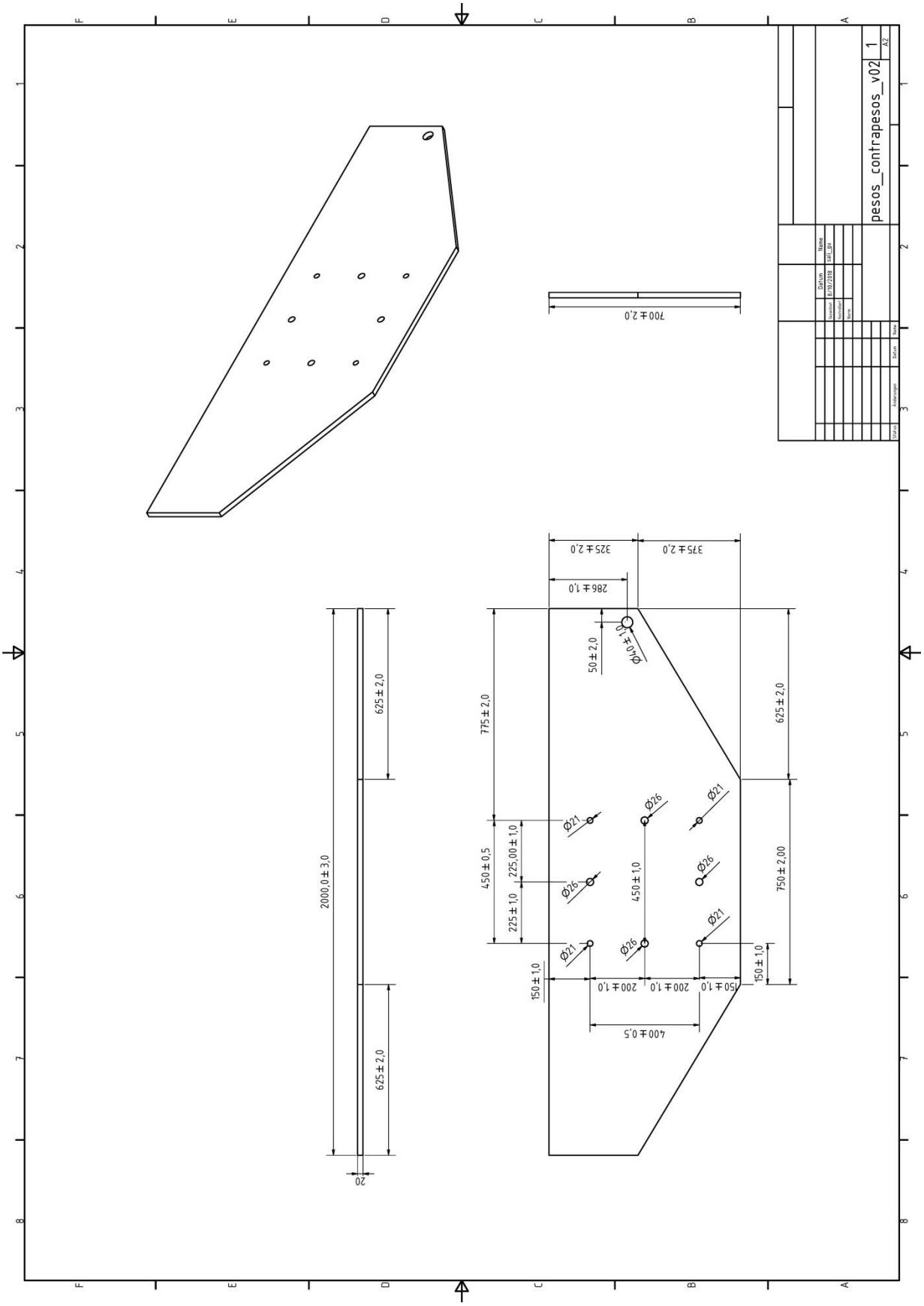

Appendix C.2 – New Cylinder Bearing Specifications

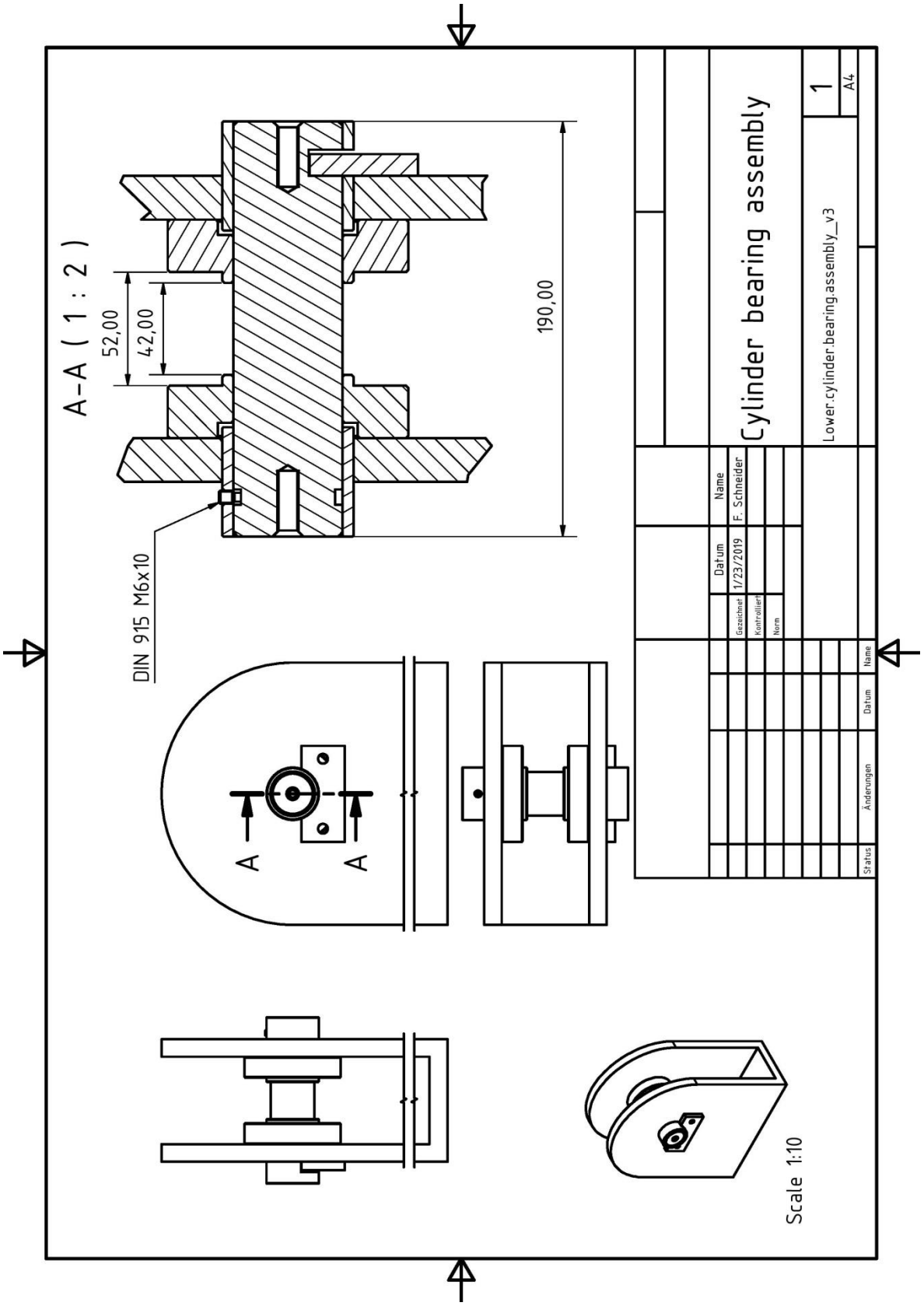

Technical specifications of a hydraulic cylinder powering the rotation

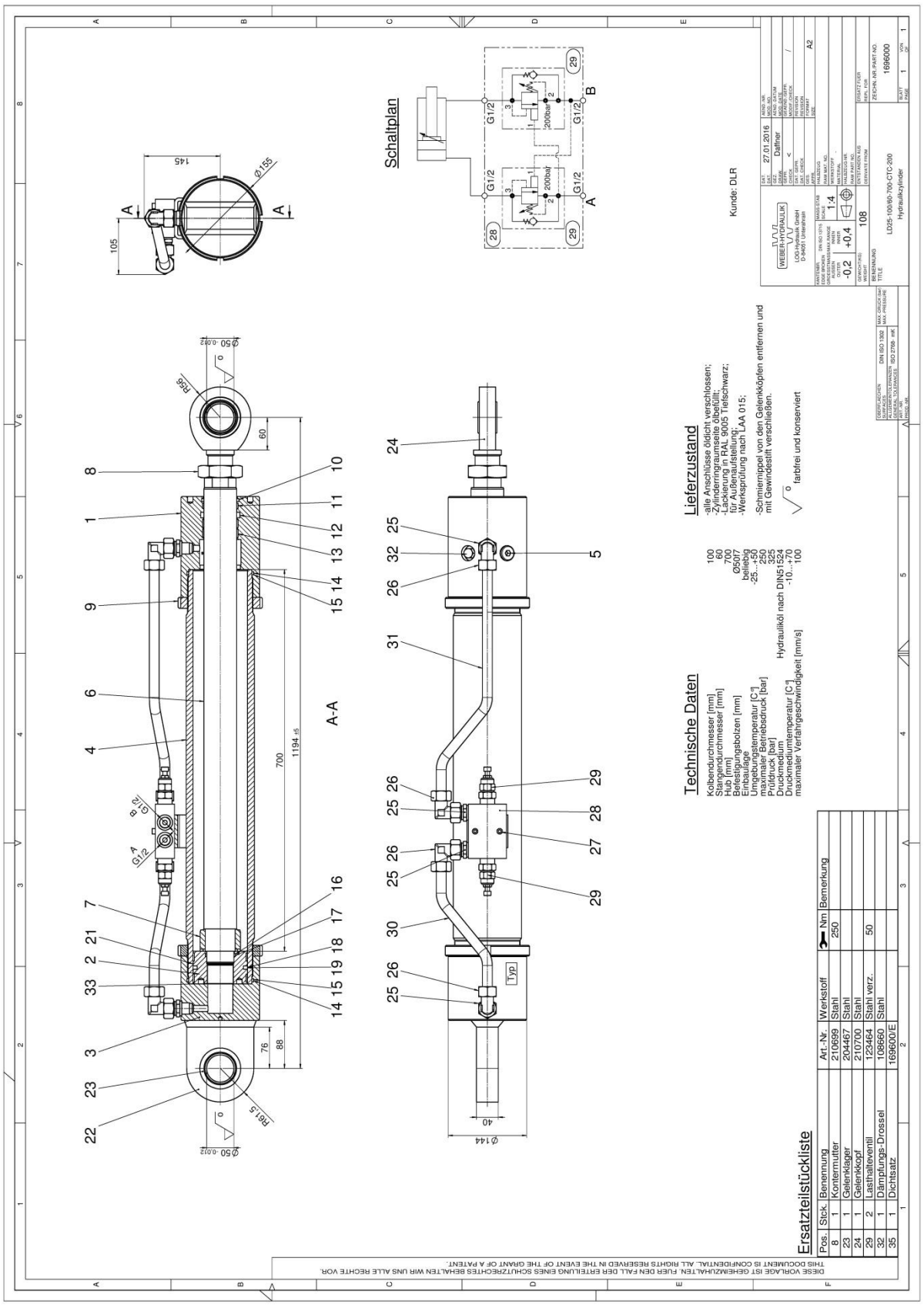

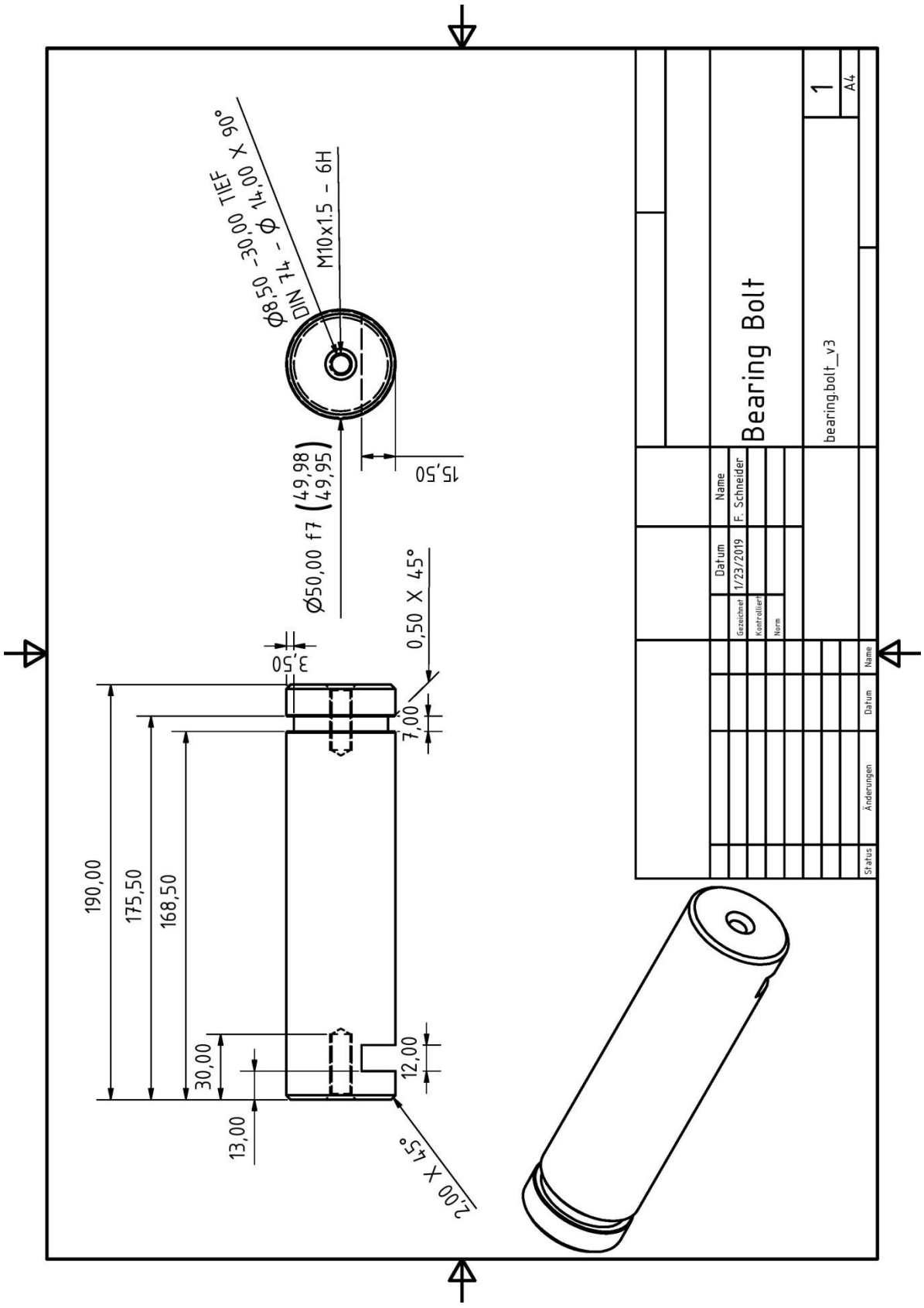
Bearing Bolt
bearing.bolt_v3
1
A4
Name
F. Schneider
Datum
1/23/2019
Gezeichnet
Kontrolliert
Norm
Status
Änderungen
Datum
Name
M10x1.5 - 6H
Ø8,50 -30,00 TIEF
DIN 74 - Ø 14,00 X 90°
Ø50,00 f7 (49,98 49,95)
15,50
0,50 X 45°
3,50
7,00
190,00
175,50
168,50
30,00
13,00
12,00
2,00 X 45°

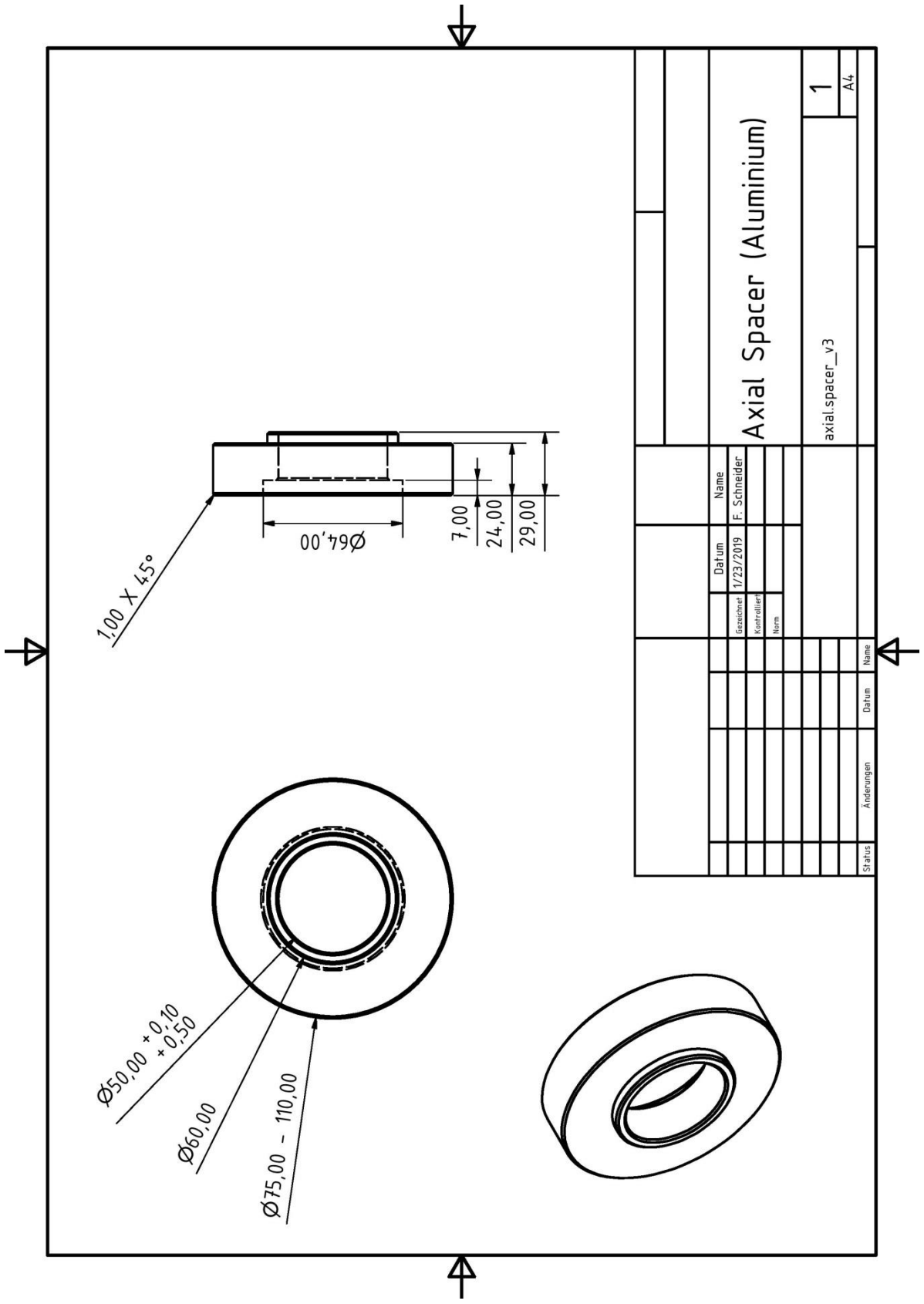
Axial Spacer (Aluminium)
axial.spacer_v3
1
A4
Name
F. Schneider
Datum
1/23/2019
Gezeichnet
Kontrolliert
Norm
Änderungen
Status
1,00 X 45°
Ø64,00
7,00
24,00
29,00
Ø50,00 +0,10 +0,50
Ø60,00
Ø75,00 - 110,00

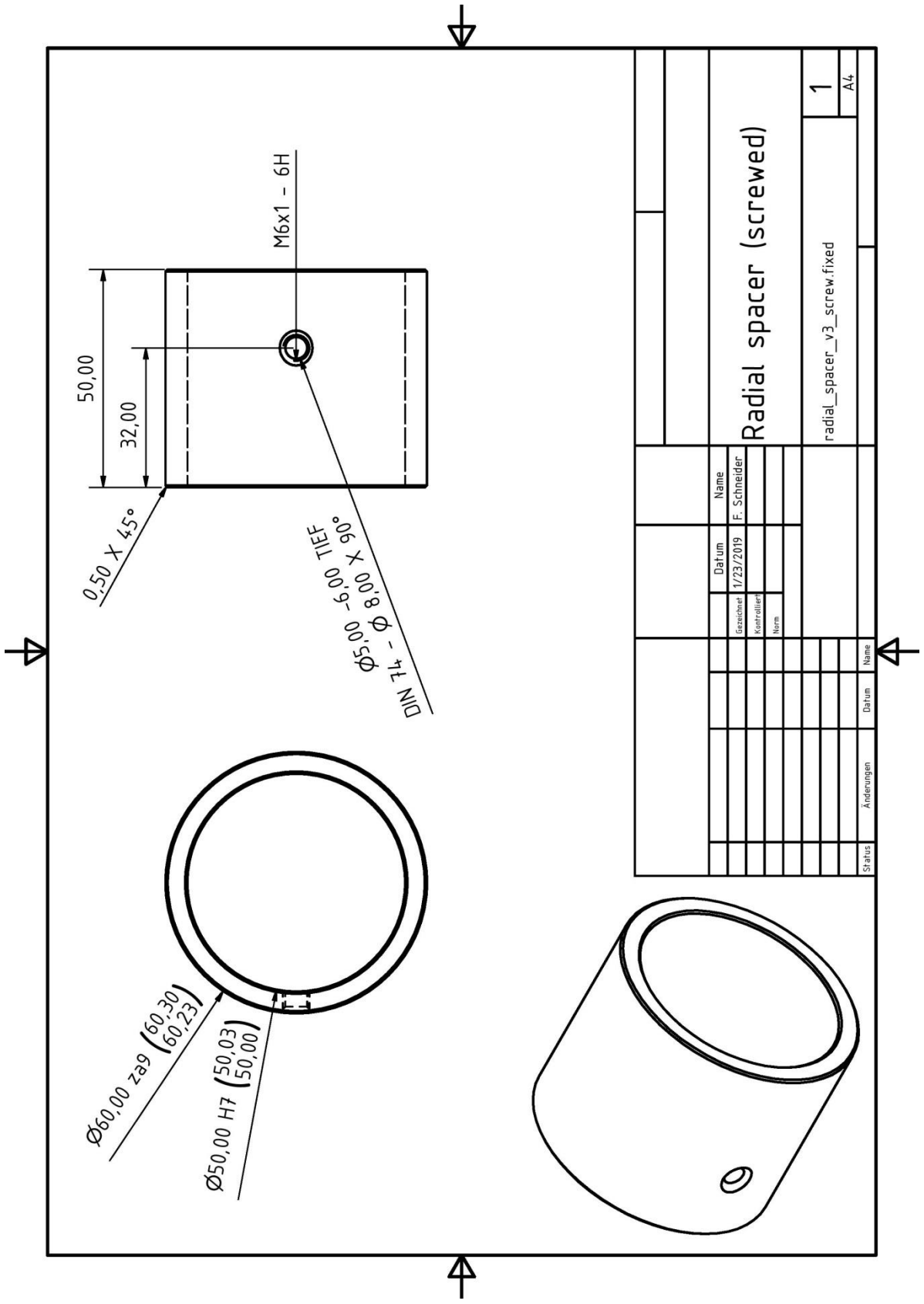
M6x1 - 6H
50,00
32,00
0,50 X 45°
DIN 74 Ø5,00 - 6,00 TIEF Ø8,00 X 90°
Ø60,00 6z9 (60,30 60,23)
Ø50,00 H7 (50,03 50,00)
Radial spacer (screwed)
radial_spacer_v3_screw.fixed
1
A4
Name
Datum
F. Schneider
1/23/2019
Gezeichnet
Kontrolliert
Norm
Status
Änderungen
Datum
Name

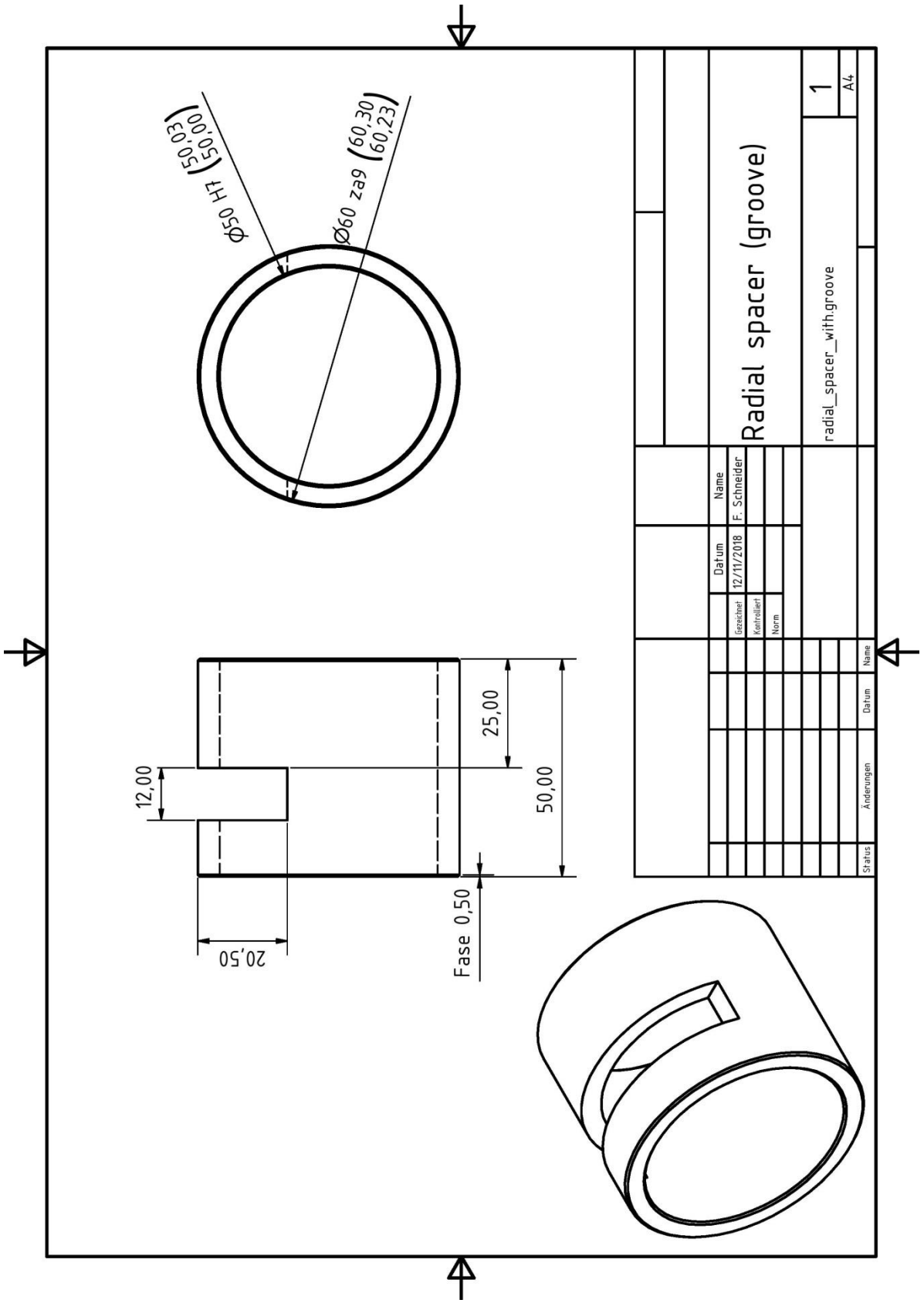
Ø50 H7 (50,03 50,00)
Ø60 za9 (60,30 60,23)
12,00
25,00
50,00
20,50
Fase 0,50
Radial spacer (groove)
radial_spacer_with.groove
1
A4
Name
F. Schneider
Datum
12/11/2018
Gezeichnet
Kontrolliert
Norm
Status
Änderungen
Datum
Name

Appendix E – Correlation between Step Size and Piston Lever

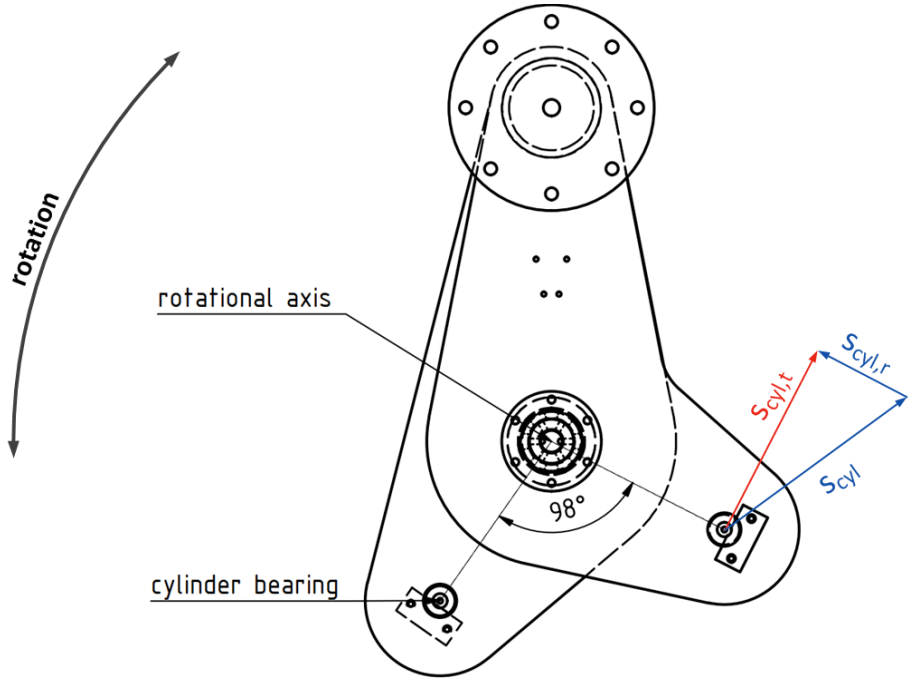

Cylinder motion at cylinder/traverse interface (vertical traverse position)

For small step sizes ≤1° the rotation can be approximated with a bearing to axis distance of 0.35m as follows:

$$\Delta\varphi_{step} = \frac{s_{cyl,t}}{0.35m} \tag{E.1}$$

The length of a piston extension is the sum of its radial and tangential components:

$$s_{cyl,t} = \sqrt{s_{cyl}^2 + s_{cyl,r}^2} \tag{E.2}$$

Because both bearings are connected to the same interface, the tangential components of the east and west cylinder piston motions are equal at all times:

$$|s_{cyl,t,east}| = |s_{cyl,t,west}| \tag{E.3}$$

The combined piston motions are proportional to the amount of oil pushed in the cylinder, which in turn is proportional to the servo speed and servo runtime which powers the gear pumps:

$$|s_{cyl,east}| + |s_{cyl,west}| = k * P_{servo} * t_{go} \quad \text{(E.4)}$$

The coefficient k of the servo power is unknown.

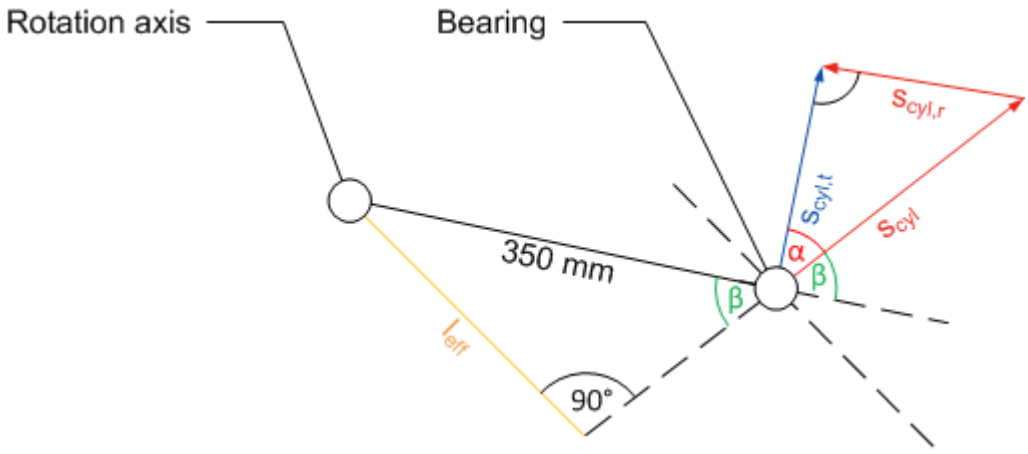

Geometric boundaries at interface

A correlation between the lever and radial component of the piston movement can be derived from the geometric boundaries at the interface:

$$s_{cyl,r} = \sin(\alpha) * s_{cyl} \quad \text{(E.5)}$$

By using

$$\alpha = 90 - \beta \quad \text{(E.6)}$$

and

$$\beta = \arcsin\left(\frac{l_{eff}}{0.35m}\right) \quad \text{(E.7)}$$

the equation for the radial component of the piston movement results to:

$$s_{cyl,r} = \cos\left(\arcsin\left(\frac{l_{eff}}{0.35m}\right)\right) * s_{cyl} \quad \text{(E.8)}$$

This equation can be inserted into Equation E.2:

$$s_{cyl,t} = s_{cyl} \sqrt{1 + \cos^2\left(\arcsin\left(\frac{l_{eff}}{0.35m}\right)\right)} \tag{E.9}$$

The equation can be further simplified with:

$$\cos(\arcsin(x))(= \sqrt{1 - x^2} \tag{E.10}$$

This results in:

$$s_{cyl,t} = s_{cyl} \sqrt{2 - \left(\frac{l_{eff}}{0.35m}\right)^2} \tag{E.11}$$

This can be correlated to the servo power with Equation E.4 and then simplified with Equation E.3:

$$k * P_{servo} * t_{go} = \frac{s_{cyl,t,east}}{\sqrt{2 - \left(\frac{l_{eff,east}}{0.35m}\right)^2} + \sqrt{2 - \left(\frac{l_{eff,west}}{0.35m}\right)^2}} \tag{E.12}$$

Substituting with Equation E.1 the correlation between step size and effective levers of the piston forces is established:

$$\Delta\varphi_{step} = \frac{k * P_{servo} * t_{go}}{0.35m} \left[\sqrt{2 - \left(\frac{l_{eff,east}}{0.35m}\right)^2} + \sqrt{2 - \left(\frac{l_{eff,west}}{0.35m}\right)^2}\right] \tag{E.13}$$